

SOLID MECHANICS EFFECTS IN CRYOPRESERVATION VIA VITRIFICATION

Submitted in partial fulfillment of the requirements for

the degree of

Doctor of Philosophy

in

Department of Mechanical Engineering

David Phillip Eisenberg

B.S., Mechanical Engineering, Carnegie Mellon University

M.S., Mechanical Engineering, Carnegie Mellon University

Carnegie Mellon University

Pittsburgh, PA

May 2015

ACKNOWLEDGEMENTS

First and foremost, I would like to thank my advisor, Professor Yoed Rabin. None of my work would have been possible without his help and support. Additionally, I would like to thank Dr. Michael Taylor, Professor Paul Steif, and Professor John Bischof for their insights into cryobiology, solid mechanics, and thermal medicine respectively, as well as the rest of the thesis committee for their help in shaping my research and their useful feedback. In addition, I would like to thank Jorge Jimenez-Rios for his help in rebuilding/calibrating the low temperature thermal expansion device. I would also like to thank my colleagues in the Biothermal Technology Laboratory, Anjali Sehrawat, Justin Feig, CJ Thaokar, Lily Ehrlich, and Rob Keelan as well as my friends and colleagues throughout Carnegie Mellon University. Finally, I would like to thank my family for always supporting me. My Work was supported by a National Science Foundation Graduate Research Fellowship under Grant No. DGE-1252522.

ABSTRACT

Cryopreservation via vitrification is the most promising means for long-term preservation of bulky tissues and organs. While the road to successful cryopreservation is paved with obstacles, of paramount importance is thermo-mechanical stress, which can lead to fracture. In order to model the mechanical stress within a vitrifying domain during cryopreservation, the relevant thermal and mechanical properties must be explored. Toward that end, mechanical properties, such as coefficient of thermal expansion and Young's modulus were measured in the cryogenic temperature range for a new class of cryoprotective cocktail involving DP6 (a less concentrated variant of VS55 without formamide) combined with synthetic ice modulators.

A synthesis of material models and properties, some measured in the current research work and others available from the literature, were incorporated into finite element models in order to model thermo-mechanical stress. An array of representative cases has been selected to investigate the effects of a spectrum of thermal histories on the resultant mechanical stress. In particular, a temperature hold near the glass transition temperature (i.e. annealing) has shown to significantly decrease the amount of mechanical stress. Other representative cases have been used to investigate the effects of volumetric warming on mechanical stress. It was shown that internal heating using a volumetric rewarming method reduces the stress to tolerable levels, even in cases involving high cooling and rewarming rates.

Additionally, photoelastic experiments were performed using an in-house proprietary device known as the cryomacroscopic. These photoelastic experiments allowed for the *in-situ* visualization of the stress field in real time. Photoelasticity experiments were used to validate a key finding from finite element analysis presented in this thesis. Finally, a new phenomenon associated with the stress history was discovered, where stresses are seen to increase during rewarming around the glass transition temperature and an explanation was proposed based on the Narayanaswamy model of glasses.

TABLE OF CONTENTS

1 Background	11
1.1 Vitrification	12
1.2 Solid Mechanics in Vitrification	13
1.3 Objectives and Specific Aims	14
2 Thermal Expansion Measurements in Higher Cryogenic Temperatures	15
2.1 Previous Studies	15
2.2 Synthetic Ice Modulators	16
2.3 Experimental Apparatus	17
2.4 Materials Tested	21
2.5 Results and Discussion	22
2.6 Summary and Conclusion	34
3 Thermal Expansion Measurements in Lower Cryogenic Temperatures	35
3.1 Experimental Setup	36
3.2 Artery Sample Preparation	39
3.3 Data Analysis	40
3.4 Results and Discussion	41
3.5 Unified Thermal Expansion Curves	46
3.6 Summary	50
4 Stress-Strain Measurements in Vitrified Arteries Permeated With Synthetic Ice Modulators	51
4.1 Experimental Apparatus	51
4.2 Materials	54
4.3 Methods	55
Specimen Setup	55
Experimental Protocol	55
Cross Section Measurements	57
4.4 Results and Discussion	58
4.5 Summary and Conclusions	64
5 Effects of Thermal History on Mechanical Stress in Cryopreservation via Vittrification	65
5.1 Background Information on Mechanical Stress In Cryopreservation Via Vittrification	65
5.2 Modeling	66
5.2.1 Material Model	67
5.2.2 Finite Element Solution	68
5.2.3 Material Properties	70
5.2.4 Thermal History at the Boundary	73
5.3 Results and Discussions	75
5.3.1 Thought Experiment	75
5.3.2 CPA Simulation—Case A	79

5.3.3 Simulations for CPA and container—Case B	84
5.4 Summary and Conclusion	87
5.5 Effect of Container on Annealing Time	88
6 Photoelastic Analysis	90
6.1 History of the Cryomicroscope	90
6.2 Introduction to Photoelasticity	92
6.3 Experimental Apparatus	93
6.3.1 Polarized-light Protocol	97
6.4 Analysis of previously unknown phenomenon	97
6.5 Experimental Investigation of Annealing	100
6.6 Summary of Photoelastic Experiments	105
7 Volumetric Rewarming in Cryopreservation.....	106
7.1 Background on volumetric warming techniques	106
7.2 Mathematical Model	108
7.3 Results and Discussion.....	110
7.4 Summary	112
8 Future Work.....	114
8.1 Summary of Research Projects	114
8.2 Additional Experimental Work	115
8.3 Additional Theoretical Work	116
References	117
Appendix: Material Property Summary	128

LIST OF FIGURES

Figure 2.1: Schematic illustration of the experimental apparatus [1] (with permission).....	19
Figure 2.2: Thermal history in a typical experiment, where T_{in} and T_{out} are the temperatures at center and the wall outer surface of the chamber, respectively [2].	23
Figure 2.3: Experimental results for pressure versus temperature for two typical cases: (i) DP6 without SIM, and (ii) DP6 + 12% PEG400 (the letters represent key points in the process, as described in the text) [2]	24
Figure 2.4: Cooling and rewarming rates for the two experiments shown in Fig. 2.3 [2].....	25
Figure 2.5: Polynomial approximation of the thermal strain for DP6 combined with various SIMs in the presence and absence of bovine muscle specimens [2].	27
Figure 2.6: Thermal strain data from all the individual experiments used for the polynomial approximations displayed in Fig. 5: (a) DP6+12% PEG400 (b) DP6+6% 1,3-CHD, and (c) DP6+6% 2,3 butanediol; j is the experiment number and solid lines represent the best-fit polynomial approximations [2].....	29
Figure 2.7: Polynomial approximation of the thermal strain for DP6 combined with various SIMs in the presence and absence of goat artery specimens [2].	30
Figure 2.8: Thermal strain data from all the individual experiments used for the polynomial approximations displayed in Fig. 7: (a) DP6+12% PEG400 (b) DP6+6% 1,3-CHD, and (c) DP6+6% 2,3 butanediol; j is the experiment number and solid lines represent the best-fit polynomial approximations [2].	32
Figure 2.9: Volume fraction of ice crystals in the case of partial vitrification displayed in Fig. 2.8(c): goat artery specimens permeated with DP6+6% 1,3-CHD [2]	33
Figure 3.1: Schematic illustration of the experimental setup to measure the thermal expansion in the current study [3] (with permission).....	36
Figure 3.2: Schematic illustration of the cooling chamber of the experimental setup displayed in Fig. 3.1 [3] (with permission).	36
Figure 3.3: Typical thermal history during experimentation, where T_{sample} is the blood vessel temperature at its mid-height, and T_{top} and T_{bottom} are the temperatures measured at the top and bottom of the cooling chamber [4].....	39
Figure 3.4: A typical strain-temperature curve obtained with the experimental system: (a) section B-C is the analyzed segment, where the material follows the expected thermal behavior of a vitrifying material, and (b) analyzed data from the same experiment using a 2 nd and 4 th order polynomial; error bars indicate $\pm 2\sigma$ [4].	43
Figure 3.5: Thermal strain of DP6 combined with (a) 12% PEG400, (b) 6% 1,3-CHD, and (c) 6% 2,3-BD. Symbols represent individual data points, solid lines represent polynomial approximation, and dashed lines represent an uncertainty range of $\pm 2\sigma$ [4].	45

Figure 3.6: Polynomial approximations of the three DP6 + SIM solutions. Since data compilation was performed for the rewarming stage, which started in the temperature range of -170°C to -160°C , a strain value of zero was selected at the reference temperature of -160°C . For clarity in presentation, representative error bars ($\pm 2\sigma$) are displayed for the DP6+12% PEG400 curve only [4].46

Figure 3.7: Unified thermal-expansion curves including data from the upper [2] and lower [current study] parts of the cryogenic temperature range, for DP6 combined with (a) 12% PEG400, (b) 6% 1,3-CHD, and (c) 6% 2,3-BD. Symbols represent data points calculated from the polynomial approximation for each subset (Table 3.1), solid lines represent polynomial approximations of the unified thermal strain, and dashed lines represents the $\pm 2\sigma$ range [4].49

Figure 4.1: Schematic illustration of the key elements of the cooling mechanism for mechanical testing. During experimentation, the artery is attached to the mechanical testing rods (see Fig.4.2), the cooling chamber is closed with a brass cover, and the system is covered with thermal insulation from all sides [5].51

Figure 4.2: Schematic illustration of the mechanical-rods thermal insulators, which were designed to accommodate smaller diameter arteriesv [5].52

Figure 4.3: An artery sample placed in the cooling chamber and ready for testing, where the cover of the cooling chamber has to be installed and insulated before experimentation. Also shown are thermocouples connected to both ends of the sample, where an additional thermocouple at the center of the sample is yet to be placed [5].53

Figure 4.4: A typical thermal history for tensile testing experimentations [5].56

Figure 4.5: Images used to calculate the cross sectional area of the artery specimens, including: (a) a stills image of four representative segments and a ruler, to determine area per pixel; (b) a black and white processed image; and (c) an isolated segment used for pixel counting [5].58

Figure 4.6: Three typical stress-strain curves obtained in the current study: (Case 1) representing the linear-elastic behavior found for specimens permeated with all solutions except for the cocktail DP6+PEG400; (Case 2) a possibly hardening specimen, permeated with DP6+PEG400; and (Case 3) a specimen permeated with DP6+PEG400, possibly exhibiting viscous flow or plastic deformations [5].59

Figure 4.7: Results of repeated loading-unloading cycles in of a blood vessel specimen permeated with DP6 + 12% PEG400: (a) the loading portions of the protocol, and (b) the unloading portions of the protocol; labels A, B, and C point to step-like changes of strain, possibly associated with the formation of microfractures [5].60

Figure 5.1: Schematic illustration of the axisymmetric model used for FEA in the current study for two key cases: (Case A) CPA in the absence of a container, where identical temperature boundary conditions are imposed on Ω_1 , Ω_2 , and Ω_3 ; and (Case B) CPA contained within a cylindrical vial, where identical temperature boundary conditions are imposed on Ω_4 and Ω_5 , while thermal insulation is assumed on Ω_3 , consistent with [6]. In both cases zero normal stress is assumed on the outer most surfaces. In Case B, continuity in temperature and displacement are

assumed on Ω_1 and Ω_2 . Also illustrated for the purpose of discussion the maximum principle-stress points, σ_A and σ_B , for Cases A and B, respectively [7].....69

Figure 5.2: The key thermal histories used in the current study and the corresponding principle stress for the case of uncontained CPA (Case A): (a) the thermal history imposed on the external boundary (Fig. 1), where the modified protocol includes an annealing stage; and (b) the corresponding principle stress at the center of the domain, subject to data shifted in time such that both data sets have a common onset of rewarming in stage R5—the stage in which maximum stress is found [7].....74

Figure 5.3: Qualitative results of a thought experiment subject to simplified boundary conditions in Case A: (a) the expected thermal history at the center of the domain subject to imposed temperature on the outer surface; and (b) the corresponding principle (also axial) stress at the center of the domain for both an elastic and viscoelastic material models [7].78

Figure 5.4: Maximum tensile stress for the in general Case A of the modified protocol (stress relaxation stage included) for variable boundary conditions. In each special case, only one parameter is varied at a time, while the maximum stress is always found in R5, qualitatively consistent with Fig. 5.2 [7].79

Figure 5.5: Stress history for variable annealing temperatures (stage R2) in Case A. Datasets have been shifted in time such that all have a common onset of rewarming in stage R5—the stage in which maximum stress is found [7].....81

Figure 5.6: stress history for CPA within a container with the three stress components clearly labeled. The stress history was chosen so as to make each component clearly visible. Also, note how the stress relaxation in R2 is slower when compared to the stress relaxation for a CPA without a container [7].84

Figure 5.7: (a) Stress history at the location offset from the center for the R4 variations, and (b) stress history at the bottom right corner for the R4 variations; see σ_B in Fig. 5.1 [7].86

Figure 5.8: Schematic illustration of sandwich seal composite.....88

Figure 5.9: Effect of container stiffness on stress relaxation time.....89

Figure 6.1: Schematic illustration of the Cryomicroscope IV assembly incorporating polarized-light illumination. A personal computer is used for hardware control, data acquisition, and post-processing [115].94

Figure 6.2: Schematic illustration of the Cryomicroscope IV stage incorporating components for polarized-light visualization: (a) isometric view including components used for non-polarized light, (b) side view showing polarized-light components only, where the red-dashed arrows mark the direction of polarized light propagation [115].96

Figure 6.3: Photoelastic effects during rewarming of vitrified material: (a) beginning of rewarming with relaxation at the wall (warmest point); (b) relaxation continues with stresses staying higher in the region trapped between the cavity and the wall; (c) the development of additional stresses at the walls as the CPA passes through glass transition; (d) the propagation of

these additional stresses during glass transition towards the CPA center; (e) complete relaxation; (f) thermal history of the free stream thermocouple; and (g) Illustration of fictive temperature: the fictive temperature is calculated by connecting a line beginning at the current value of a property, p , parallel to the glassy modulus, α_g , to a line collinear with the liquidy modulus, α_l . [116].99

Figure 6.4: Representative images showing the process of stress build-up and subsequent annealing in 7.05 M DMSO at 95 W, with an intermediate temperature-hold of -125°C , which is 5°C above the glass transition temperature [56]: (a) stress starts to build up at the beginning of the temperature-hold period, with the highest level appearing at the walls; (b) the stress level continues to increase with its maximum value propagating inwards towards the cavity; (c) the maximum stress was observed approximately 90 seconds after the beginning of the temperature-hold time; (d) significant decrease in stress at the end of the annealing process about 5 minutes after starting, displaying a brightness level comparable with the image presented in (a); and (e) thermal history of the free stream thermocouple [115].102

Figure 6.5: Scanning cryomicroscope images of photoelasticity effects in the study of annealing on 7.05M DMSO: (a) experiment #7 showing the beginning of annealing at -125°C with a polarized-light source power of 100 W; (b) stress-relaxed sample at the end of the temperature-hold stage in experiment #7; (c) the stress field in experiment #7 at 7°C below the glass transition temperature as measured by the free stream thermocouple, using a polarized-light source power of 45 W; (e) the stress field in experiment #8 at 7°C below the glass transition temperature as measured by the free stream thermocouple, using the same cooling protocol and illumination settings as in experiment #7 but in the absence of an annealing stage [116].103

Figure 6.6: Thermal history of the experiments displayed in Fig. 8: (a) free stream thermocouple data from experiment #7 (with annealing at -125°C); (b) free stream thermocouple data from experiment #8 (no annealing); (c) ANSYS simulation results showing the temperature field at the center of the CPA from experiment #7 when the outer surface of the specimen reaches a temperature of 7°C below the glass transition temperature at 1200 seconds (corresponding to Fig. 8(c)); (d) ANSYS simulation results showing the temperature field at the center of the CPA from experiment #8 when the outer surface of the specimen reaches a temperature of 7°C below the glass transition temperature at 577 seconds (corresponding to Fig. 8(d)) [116].104

Figure 7.1: Specific heat capacity (left) and specific absorption rate (right) of VS55 combined with 10 mg/ml of Fe_3O_4 Nanoparticles109

Figure 7.2: Ambient temperature history consists of one stage cooling ($-11.76^{\circ}\text{C}/\text{min}$), 500s hold at storage, one stage warming ($39.88^{\circ}\text{C}/\text{min}$), and 250 s hold at room temperature109

Figure 7.3: Axial stress at center of domain. Both protocols consist of identical cooling profiles and ambient rewarming temperatures. The volumetric rewarming case also includes uniform heat generation due to nano-particle RF warming.....110

Figure 7.4: Stress history due to ambient temperature history shown in Fig. 7.2.111

Figure 7.5: (left) stress history for four different cooling rates, (right) zoomed in maximum rewarming stress for those same cooling rates112

LIST OF TABLES

Table 2.1: Coefficients of best-fit polynomial approximation of thermal strain, $\varepsilon = a_2T^2 + a_1T + a_0$, and the thermal expansion, $\beta = 2a_2T + a_1$, where R^2 is the coefficient of determination.	26
Table 3.1: Coefficients of best-fit approximation of the thermal strain, $\varepsilon = a_1T^4 + a_2T^3 + a_3T^2 + a_4T + a_5$, for selected DP6-SIM mixtures, where the thermal expansion coefficient is given by $\beta = 4a_1T^3 + 3a_2T^2 + 2a_3T + a_4$, and where R^2 is the coefficient of determination.	47
Table 4.1: Summary of experimental data.....	63
Table 5.1: Physical properties used in this study.....	72
Table 5.2: Summary of thermal-history parameters and the resulting maximum stresses resulting maximum stresses for the cases compared in Fig. 4.	80

Chapter 1: Background

In the United States of America, twenty one people on average die each day while waiting for an organ transplant. Worse still, the gap between the number of people waiting for an organ and the number of available organs has continued to widen over the past two decades (based on data from the Organ Procurement and Transplantation Network, OPTN). There is currently a major effort to develop engineered tissues which will be able to fill in this gap [8–11]. Currently, the shelf life for most implantable tissues is in the range from a few hours to a few days. Even if engineered organs become available, this short shelf will cause a severe problem for supply chain management. Ideally, organs would have a long shelf life so that any surplus at one point in time could be banked for future use, thus smoothing out any supply-demand mismatches.

Contrary to common belief, freezing per se is not a viable means of preserving the tissue, as it has already been shown that ice crystallization is lethal in organs [99-101]. However, the shelf life of small specimens, such as cells in suspension, has been radically extended through the use of cryopreservation [12–16]. Classical cryopreservation, with low concentrations of cryoprotective agents (CPAs), works well for preserving individual cells or cell clusters. CPAs help to control ice formation in order to increase cell survival post thawing. As the solution cools, part of the domain freezes, which increases the CPA concentration in the rest of the domain. This process continues until the CPA concentration left over is so high that it can no longer crystallize and is left in an amorphous, arrested fluid state. For this technique, cell survival rates are highly dependent upon the cooling rate as described in Peter Mazur's famous two factor hypothesis of freezing injury [12], where the cells are likely to suffer from two distinct damaging mechanisms: (i) Supra-optimal cooling rates cause intracellular ice formation, where the precise cause of cell death is not fully understood, but it appears to be related to mechanical interaction of ice crystals with the cell membrane. (ii) Sub-optimal cooling rates, where pure water in the extra-cellular space freezes first, which increases the concentration of the remaining solution, resulting in cell death due to the relatively long exposure to elevated concentration, dehydration, and pH changes. This leaves the cells with an optimal cooling range where there is high cell survival post thawing.

Unfortunately, the cryopreservation protocols that have proven so effective for small scale samples such as cells in suspension, have proven to be mostly inadequate for large scale tissues and organs [17–19]. Classical cryopreservation allowed for extracellular crystallization, which is

mostly innocuous for cells in suspension. However, extracellular crystallization can damage the tissue structure in complex tissues and organs, rendering them non viable post thawing [17,20].

1.1 Vittrification

The alternative to classical cryopreservation is cryopreservation via vittrification (vitreous means glassy in Latin). Cryopreservation via vittrification employs high concentrations of CPAs and high cooling/warming rates in order to completely prevent crystallization and induce an amorphous, non-crystalline arrested liquid state due to a drastic increase in the material's viscosity. Thus, the problems with classical techniques listed above may be bypassed [20,21]. The idea of applying vittrification in order to preserve a biological system was first proposed by Basile J. Luyet in 1937 [22,23]. No appreciable degradation occurs over time in living matter trapped within a vitreous matrix, and vittrification is potentially applicable to all biological systems.

At relatively high temperatures, glass forming materials act as a viscous fluid, however, the viscosity increases with the decreasing temperature and the elastic effects take over when the material starts to behave as a solid. This temperature where the material transitions from fluid-like to solid-like is known as the glass transition temperature and is often defined as the temperature where the viscosity is equal to 10^{12} Pa-s (though other definitions based on changes in coefficient of thermal expansion or specific heat capacity exist as well).

As CPAs cool, their viscosity increases exponentially. If one cools down a CPA solution quickly enough, depending on the type and concentration of the CPA, then the rapid viscosity increase can prevent the water molecules from having the mobility needed to rearrange into the positions of the crystal lattice. This prevents the formation of ice crystals and promotes vittrification. The cooling rate threshold that must be exceeded in order to suppress crystallization and promote vittrification is known as the “critical cooling rate” and is dependent on the type and concentration of the CPA. Additionally, crystallization can also occur during rewarming. This is known as rewarming phase crystallization (RPC) and can take the form of either devitrification or recrystallization. Devitrification occurs when the viscosity of the domain decreases as the temperature increases, this increases the mobility of the molecules, allowing them to rearrange into the positions of the crystal lattice. Recrystallization also occurs as the temperature, and thus mobility increase, but instead of forming new ice crystals, recrystallization is when crystals that

were already formed during cooling now have a chance to grow into larger crystals. In order to prevent both types of RPC, a critical warming rate must be achieved. As a rule, the critical warming rate is generally higher than the critical cooling rate.

1.2 Solid Mechanics in Vitrification

In order to successfully vitrify a biological specimen, two things are required, high concentrations of CPAs and high cooling/warming rates. These two things work in concert, higher CPA concentration allows for lower cooling/warming rate and vice versa. Unfortunately, both of these factors can be deleterious to tissue viability post thawing. CPAs are generally toxic, and high concentrations can cause toxicity damage. The cooling/warming mechanism is generally applied to the surfaces of the material. Since the thermal conductivity of biomaterials is relatively low, there is a limit to cooling/warming rate achievable at the center of the specimen. In order to surpass the critical cooling/warming rate, very high rates need to be applied at the surface. These high rates coupled with low thermal conductivity induce thermal gradients. Since most materials (including biomaterials) tend to shrink when cooled, the thermal gradient induces a thermal strain gradient. Since adjacent layers of the material cannot overlap, thermal stress develops, making the resulting strain compatible. If this stress exceeds a critical threshold, permanent damage may occur rendering the sample non viable post thawing. A dramatic example of this permanent damage is fracture.

A successful cryopreservation protocol needs to strike a balance between minimizing CPA concentration to prevent toxicity and lowering the cooling/warming rates to minimize mechanical stress. There has been a large effort put into understanding and minimizing the effects of CPA toxicity. Many of these efforts have focused on characterizing CPA toxicity [24,25], developing CPA additives [20,26–28], or CPA “cocktails” which are combinations of multiple CPAs [29]. Unfortunately, there has been relatively little effort put into understanding or minimizing the effects of mechanical stress in cryopreservation.

Despite the scant attention paid to them, fractures have been observed in the context of cryopreservation numerous times in the literature [30–35] and mechanical stress has been suggested as a possible cause of failure for cryopreserved tissues [36]. The current approach to minimizing mechanical stress normally pursued is best described as “guess and check.” Cryopreservation protocols are proposed, tested, and then when they fail due to fractures, they

are revised in somewhat haphazard ways, in an attempt to alleviate mechanical stress. A more methodical, engineering type approach could save both time and money. The thermal and mechanical properties of tissues need to be measured, and then models can be built which simulate the cryopreservation process to determine its likelihood to cause fracture. Using the results from these simulations, improved cryopreservation protocols could then be designed. This would allow researchers to investigate a much wider array of potential cryopreservation protocols in less time and with less financial cost.

1.3 Objectives and Specific Aims

This thesis is part of an ongoing effort in the Biothermal Technology Laboratory (BTTL) at Carnegie Mellon University to measure the thermal and mechanical properties of vitrifying tissues and to model the mechanical response to cryopreservation protocols. Toward this end, five specific aims have been set:

1. To measure thermal expansion of low-viscosity CPA and tissue in higher cryogenic temperatures
2. To measure thermal expansion of vitrified tissue at lower cryogenic temperatures
3. To measure Young's modulus of vitrified blood vessels
4. To investigate the relationship between the thermal history and solid mechanics effects in common cryoprotocols
5. To investigate the benefits of volumetric warming by means of ferromagnetic nanoparticles in decreasing mechanical stress

Chapter 2: Thermal Expansion Measurements in Higher Cryogenic Temperatures

This chapter expands upon a recently published study in [2]. In that study, the thermal expansion of the CPA cocktail, DP6 combined with a class of compounds known as synthetic ice modulators (SIM) was measured. Since the vitrifying material changes behavior from fluid-like [1,37] to solid-like [38,39], two different experimental systems are required for mapping the effects of thermal expansion. This chapter is focused on the upper part of the cryogenic temperature range, where the CPA-SIM cocktail behaves as a fluid while the Chapter 3 is focused on the lower part, where it behaves as a solid. The synthetic ice modulators helped to suppress ice crystallization in DP6 and allowed for the experimental setup to measure thermal expansion down to much lower temperatures than was achieved in the past [2,37]. Then, with knowledge about the thermal expansion of DP6+SIM, the thermal expansion of tissues permeated with those solutions was then studied. This was the first study which investigated the mechanical properties of CPAs combined with synthetic ice modulators.

2.1 Previous studies measuring mechanical properties relevant to cryopreservation via vitrification

This chapter, along with the two subsequent ones will report on studies measuring the mechanical properties of CPAs and tissues permeated with CPAs. There have already been some studies measuring mechanical properties of materials relevant to cryopreservation via vitrification. For instance, a series of studies conducted by Bell and Rabin [40,41] and Plitz and Rabin [37] measured the thermal expansion of various CPAs and CPA cocktails within the upper part of the cryogenic temperature range, where the CPA still acts as a fluid [37,40,41]. Additional experiments then measured the thermal expansion of goat arteries and bovine muscles permeated with the 7.05M DMSO, VS55, and DP6, (the latter two are CPA cocktails whose constituents will be described in the section 2.3) within the same temperature range [1]. While no experiments to date have measured the thermal expansion of CPAs below the glass transition temperature, Jimenez and Rabin [3] designed a device which they then used to measure the thermal expansion of blood vessels permeated with 7.05M DMSO and VS55 at temperatures low enough that they reacted elastically [42]. Additionally, they modified the device and used it to measure the elastic modulus of the blood vessels permeated with the same CPAs below the glass transition temperature [38] and the viscoelastic response near glass transition [39]. The device

was modified further by Dan Noday and used to measure the viscosity of DMSO, VS55, and DP6 [43].

2.2 Synthetic Ice Modulators

Compounds that influence the formation and growth of ice nuclei and crystals by various purported mechanisms are grouped in the current study under the generic term Synthetic Ice Modulators (SIMs). This general classification embraces several categories of molecules that have been shown to modulate ice formation and growth. For example, molecules such as 1,3 cyclohexanediol (1,3 CHD) that specifically attenuates the growth of ice crystals by virtue of its chemical structure have been referred to as synthetic ice blockers (SIB) [20,44]. In contrast, compounds such as synthetic polyvinyl alcohol have been suggested to be ice modulators primarily by inhibiting heterogeneous nucleation [26]. Such compounds should be considered as “anti-nucleating agents” as opposed to “ice blockers”, but clearly fall within the general category of “ice modulators” since they are now reported to demonstrate other properties, including inhibition of ice recrystallization [28,45], thermal hysteresis and ice crystal shaping [46], indicating direct adsorption to ice. The present study includes three contrasting SIMs: 1,3CHD represents the best published example of an SIB [20,44], and 2,3 butanediol and polyethylene glycol (PEG-400), which are included as compounds known to facilitate the stability of the amorphous state by virtue of their interactions with water (reviewed in [20]). In general, ice modulators have a greater effect on influencing ice nucleation and growth and stabilizing the amorphous state than accounted for on a purely colligative basis [20].

As with any cryoprotectant, the practical utility of SIMs in cryobiology represents a balance between physical and chemical properties and their interactions with living cells. It is generally recognized that toxicity is dependent upon concentration, and often temperature, irrespective of intrinsic physical properties. This study is focused purely on an intrinsic physical property (thermal expansion) of CPA cocktails containing a variety of SIMs without specific regard for potential toxicity other than choosing compounds that have been demonstrated to have some utility in biological applications. Nevertheless, the rational approach of reducing the inherent chemical toxicity of the CPA cocktails by reducing the total concentration of solutes while retaining desirable physical attributes is an underlying value of incorporating SIMs [20,47].

The combination of ordinary CPA cocktails with SIMs is further expected to reduce the rapid cooling rate necessary for vitrification, which is critical to scale-up cryopreservation for two primary reasons: (i) regardless of the cooling mechanism at the outer surface, the achievable cooling rate at the center of a bulky specimen is always lower—limited by principles of heat conduction through the tissue, and (ii) lower cooling rates often mean lower thermo-mechanical stress and diminishing risk to structural damage.

While the concept of using a SIM as a controlling agent of crystal growth is not new, very limited corresponding information is available in the literature of cryobiology. Of particular relevancy to the current study is a recent report on the application of the CPA cocktail DP6 combined with 1,3 cyclohexanediol (1,3-CHD) as an experimental SIB and found that the addition of 1,3-CHD to DP6 significantly improved its tendency to vitrify in the preservation of pancreatic islets [47]. That study showed comparable islet viability for islets preserved in DP6+1,3-CHD and VS55, where the latter is a reference solution with a significantly higher concentration of permeating CPAs. More information on relevant SIMs is given in the Material and Methods below.

As a part of an ongoing effort to investigate thermo-mechanical effects in cryopreservation [1,3,35,37–39,42,48–52], the current study focuses on measuring key physical properties of the vitrifying specimen along the path of cryopreservation. In particular, thermal expansion is measured in the current study, which is the driving mechanism for thermo-mechanical stress. Since the vitrifying material changes behavior from fluid-like [1,37] to solid-like [38,39], two different experimental systems are required for mapping the effects of thermal expansion. The current study is focused on the upper part of the cryogenic temperature range, where the CPA-SIM cocktail behaves as a fluid. Beyond its key role in the formation of mechanical stress, thermal expansion can be used to study the extent of partial crystallization, when present.

2.3 Experimental Apparatus

A prototype of the apparatus for thermal expansion measurements used in the current study has been developed previously by Rabin, Plitz, and Bell [1,37,40] and is presented here in brief, for the completeness of presentation. With reference to Fig. 2.1, the experimental system consists of two main components: (i) a cooling chamber, which contains the specimen and is cooled to cryogenic temperatures, and (ii) a pressure tube, which includes a pressure transducer and

contains air at room temperature. The two components are connected by means of a flexible tube, which is filled with the same CPA solution under investigation, but has a negligible volume compared with the volume of the cooling chamber. This is a closed system, where expansion of the specimen due to temperature changes causes pressure changes in the system. It follows that the measured quantity is the pressure, whereas the modeled parameter is the thermal expansion. In order to passively control the cooling rate, the cooling chamber is placed in a cylindrical insulation shell, which is immersed in liquid nitrogen. The shell thickness is designed to achieve the desired conditions for vitrification. T-type thermocouples are placed on the outside of the cooling chamber and at its center, in order to monitor the temperature and verify that it is close to uniform across the chamber. For the purpose of the current study, the cooling chamber has been modified from 11.1 ml [1] to 3.0 ml, in order to increase the cooling rate. The thermal insulation shell was further modified accordingly to achieve pre-specified cooling rates, as demonstrated in the Results and Discussion section.

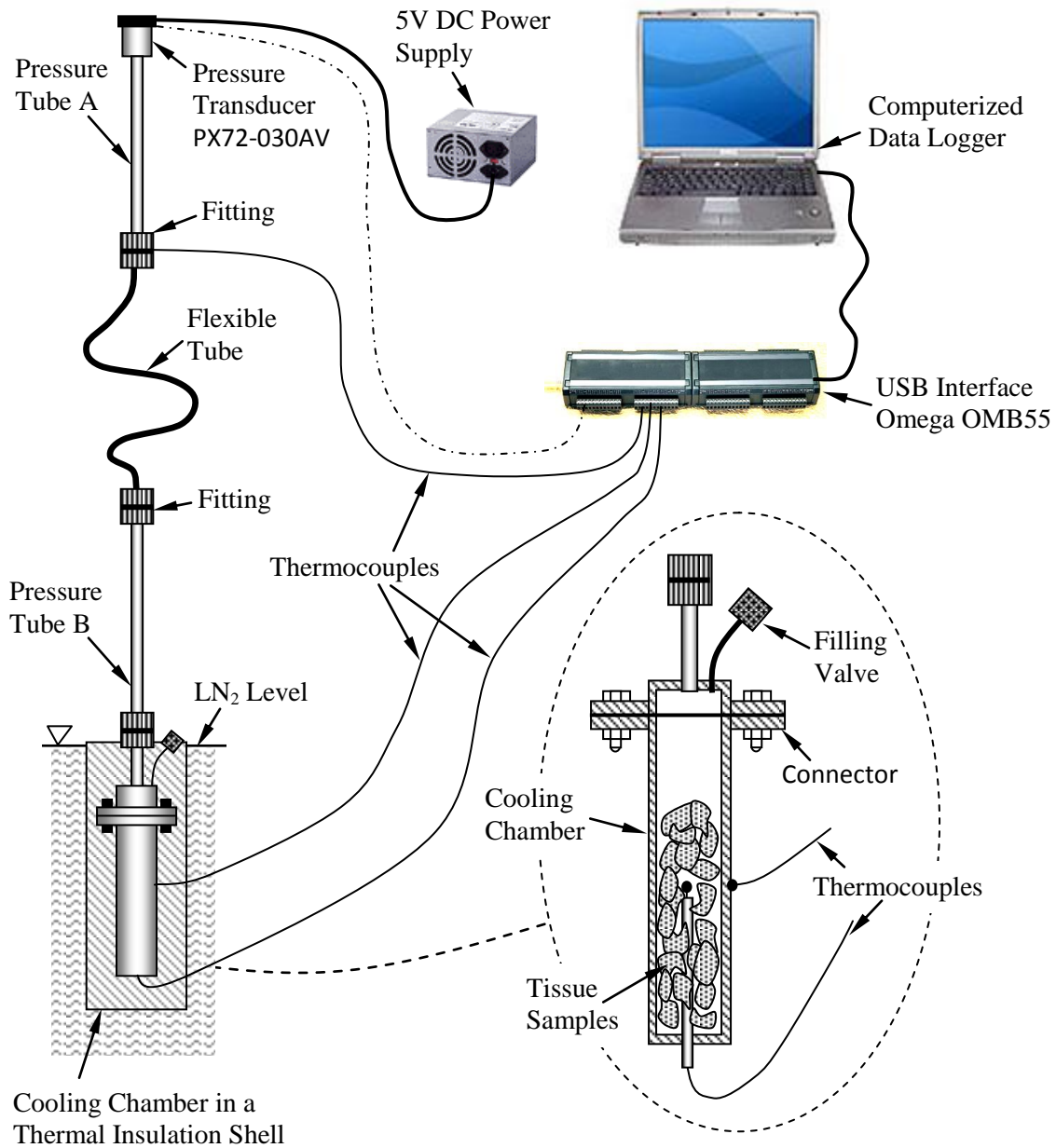


Figure 2.1: Schematic illustration of the experimental apparatus [1] (with permission).

While the experimental protocol, a detailed mathematical analysis of the system, and uncertainty analysis have been previously presented [40], the key equations are represented here in brief, as they are important for interpretation of results. The analysis requires a pressure-volume calibration curve for the specific pressure tube, which was generated by substituting the cooling chamber with micro-syringe and recording pressure versus displacement data.

Since the cooling chamber is made of brass, which is a well-characterized material, the linear strain in the sample can be extracted as:

$$\varepsilon_i = \frac{1}{3} \frac{\Delta V_i + \Delta V_{brass,i}}{V_o} \quad (2.1)$$

where V_o is the initial volume of the cooling chamber containing the specimen, ΔV_i is the volume change of the specimen, and $\Delta V_{brass,i}$ is the volume change of the brass chamber between its initial temperature, T_o , and a specific given temperature, T_i . The change in brass volume $\Delta V_{brass,i}$ is calculated by:

$$\Delta V_{brass,i} = 3V_o \int_{T_o}^{T_i} \beta_{brass} dT \quad (2.2)$$

where β_{brass} is the thermal expansion property of brass.

The rate of change of the thermal strain with respect to temperature is defined as the thermophysical property of thermal expansion, β , which can be derived from:

$$\beta = \frac{d\hat{\varepsilon}}{dT} \quad (2.3)$$

where $\hat{\varepsilon}$ is a polynomial approximation of the thermal strain ε_i , at all measurement points. While the property of thermal expansion is intrinsic, the thermal strain is a relative measure specific to a particular process (i.e., the integral of thermal expansion between two relevant temperatures). Hence, the polynomial approximation $\hat{\varepsilon}$ can be conveniently shifted for the purpose of analysis and/or presentation.

Equations (2.1)-(2.3) conveniently describe the analysis of thermal expansion for a chamber filled with a fluid (CPA-SIB cocktail in the current study). In order to analyze the thermal expansion of a CPA-permeated specimen, the experimental analysis must be performed in two consecutive steps: (i) measuring thermal expansion of the pure cocktail as described above, and (ii) measuring the thermal expansion of a chamber containing CPA-permeated tissue specimens, where the remainder of the chamber is filled with the same CPA under investigation. Once the ratio of specimen volume to chamber volume, x , is established, the thermal strain in the second step of experimentation is calculated by:

$$\varepsilon_i = \frac{1}{3} \frac{\Delta V_i + \Delta V_{brass,i}}{V_o} = (1 - x)\varepsilon_{CPA} + x\varepsilon_{tissue} \quad (2.4)$$

where ε_{CPA} is the thermal strain of the CPA solution as measured in the first step of experimentation. It follows that:

$$\varepsilon_{tissue} = \frac{\varepsilon_i - (1 - x)\varepsilon_{CPA}}{x} \quad (2.5)$$

2.4 Materials Tested

In previous studies along the current line of research, the following CPA cocktails have been tested: VS55, DP6, and DMSO in various applicable concentrations [1,37,49]. DP6 is a cocktail of 234.4 g/L DMSO (3M), 228.3 g/L propylene glycol (3M), and 2.4 g/L HEPES in EuroCollins solution. VS55 is a cocktail of 242.14 g/L DMSO (3.1M), 168.38 g/L propylene glycol (2.2M), 139.56 g/L formamide (3.1M), and 2.4 g/L HEPES in EuroCollins solution. The two cocktails are similar, excepting the exclusion of formamide from DP6 to reduce its toxicity. In return, DP6 contains a higher concentration of propylene glycol. While VS55 has been found to be a much better glass promoting cocktail [1,49], DP6 appears to be more promising due to its reduced overall CPA concentration, and therefore its toxicity.

DP6 with, or without additional ice modulators, has not yet been used extensively in biological cryopreservation principally because the focus to this point has been to characterize the physical properties and attributes of the formulation, which by design has a significantly lower total solute concentration than the baseline reference VS55 solution. It was also formulated to omit the formamide component of VS55, which has been proposed as an unnecessary and potentially toxic element of VS55 that does little to promote the vitreous state. Some pilot studies comparing DP6 with VS55 for cryopreservation of pancreatic islets provide initial support for the hypothesis that DP6 will be less toxic by virtue of the lower total CPA concentration [53]. The downside in the application of DP6 is the high cooling rate typically required for vitrification. Hence, the current pilot study focuses on DP6 combined with SIMs, in an effort to improve its performance.

While many SIMs could be selected for the current pilot study, the choice of practice is based on recent experience developed by the current research team [20]. The following compounds were thus selected as representing the broad classification of ice-control molecules: 6% 1,3-cyclohexanediol (1,3-CHD), 6% 2,3 butanediol, and 12% polyethylene glycol 400 (PEG400), which is a low molecular weight grade of polyethylene glycol.

Attempts to understand the requirements of vitrification solutions at the molecular level have led to identification of new solutes with physical properties that would promote the vitreous

state during cooling. A promising class of compounds is the polyalcohols such as 1,2-propanediol (1,2PD), which is a component of DP6, and butane-2,3-diol (2,3BD), the optical isomers of which have been shown to vitrify at significantly lower concentrations than any other known CPA [54,55]. This is important to minimize the toxic effects of using high concentrations of CPAs. The use of 2,3 BD (6% = 0.7M) as a supplemental SIM in this study is well within the toxic limits since we have previously published data showing tolerance of pancreatic islets exposed to up to 3M 2,3 BD [47,56]. Moreover, it is now established that both the concentration needed to vitrify and the toxicity can be reduced by incorporating a wide variety of non-permeating disaccharides or polymeric compounds [54,57]; hence the selection of PEG400, which we have previously reported to elevate the glass transition temperature, reduce the energy associated with the transition, and reduce the risk of devitrification in a concentration dependent manner [102]. 1,3-CHD falls within the sub-classification of SIBs that are specifically designed to lattice-match with the basal plane of an ice crystal by hydrogen bonding and thereby inhibit ice crystal growth [20,44].

The tissues models used in the current study are bovine muscles and goat carotid arteries. All tissue samples were donated by local slaughterhouses and no animals were sacrificed for the purpose of this study.

2.5 Results and Discussion

Figure 2.2 displays a typical thermal history during experimentation, with a temperature difference of less than 3°C across the specimen. The small temperature difference and the exponential decay in chamber temperature indicate that the chamber can be treated as a lumped-capacity system, which is consistent with the mathematical formulation presented above. Hence, results in Fig. 2.2 indicate that modifying the cooling chamber to have a smaller volume and faster cooling rate did not affect system performance.

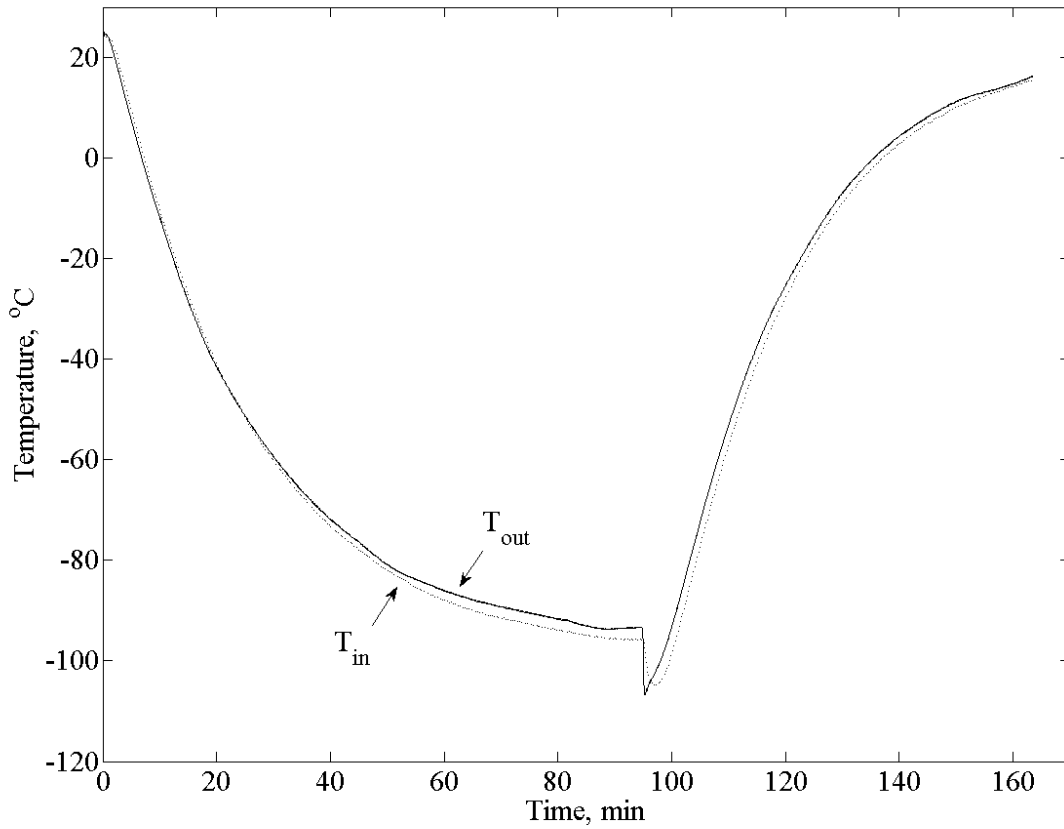


Figure 2.2: Thermal history in a typical experiment, where T_{in} and T_{out} are the temperatures at center and the wall outer surface of the chamber, respectively [2].

Figure 2.3 displays typical results for the pressure versus temperature curve, obtained in DP6 and DP6+12% PEG400 experiments. Note that the pressure in the system is proportional to the overall volumetric contraction and therefore to the strain. With respect to the DP6 curve (upper curve), the material contracts nearly linearly with temperature in section A-B, exhibiting a simple fluid behavior during cooling. Volume expansion is evident in section B-C, indicating crystallization in the specimen. Due to the extent of crystallization, the system stopped functioning in sections C-D and D-E, and the related output is meaningless. The material regains flow capability at point E during rewarming, where additional crystallization during rewarming is evident in section E-F; that is rewarming phase crystallization (RPC) in a partially vitrified material. The crystals start to melt at point F, a process which is completed by point G. The material regains its simple fluid behavior in section G-H. The range between point G and point B is the range of super cooling. In sharp contrast, no crystallization or RPC are demonstrated for

DP6+12% PEG400 following the same thermal history. Here, the exceptional system response between point B and G is associated with the high level of viscosity and departing from a simple fluid-like behavior. Thermal expansion analysis in the current study is performed on section A-B of each curve.

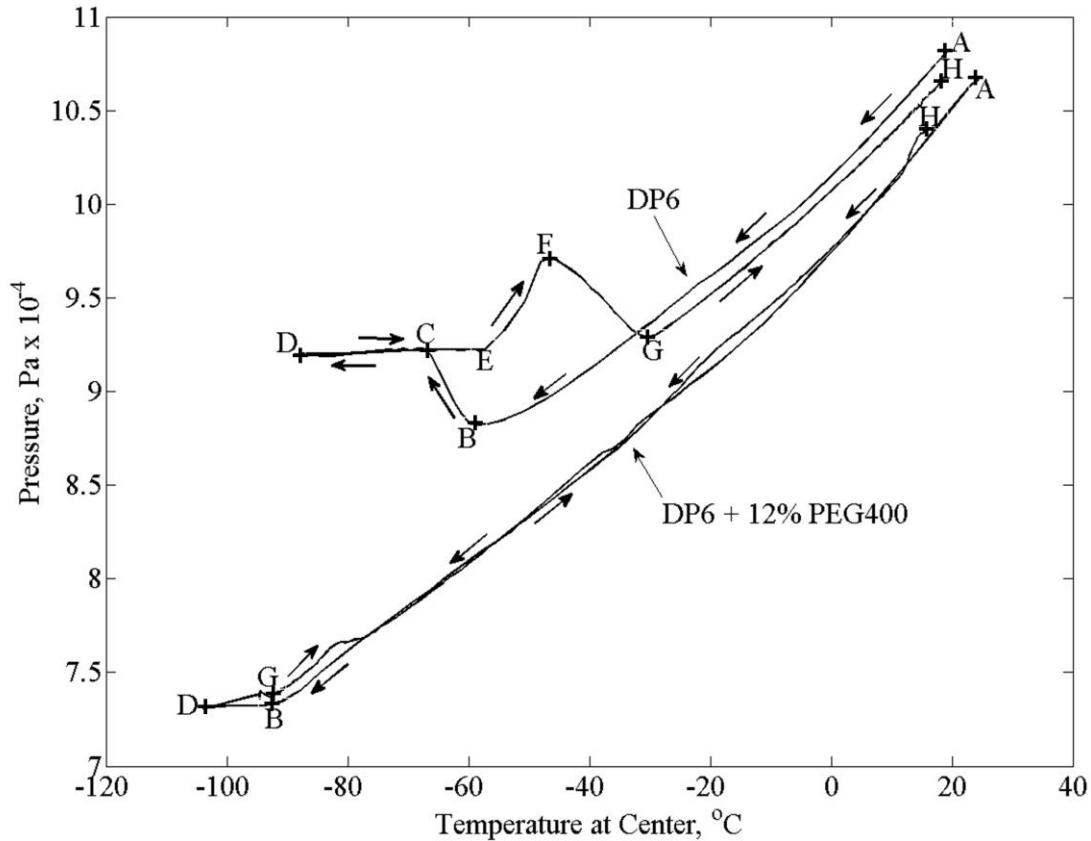


Figure 2.3: Experimental results for pressure versus temperature for two typical cases: (i) DP6 without SIM, and (ii) DP6 + 12% PEG400 (the letters represent key points in the process, as described in the text) [2]

Figure 2.4 presents the measured cooling rates from the experiments displayed in Fig. 2.3. It can be seen from Fig. 2.4 that the cooling rate in the temperature range of interest is close to linearly dependent upon temperature, which means that the thermal history can be approximated as a second order in time in the range of interest. The CPA cocktails were cooled at similar rates, ranging from $-4.5^{\circ}\text{C}/\text{min}$ at the beginning of cooling down to below $-1^{\circ}\text{C}/\text{min}$ as the CPA cocktail approached -100°C . The rewarming phase followed a somewhat similar pattern. Interestingly, the effects of RPC are evident from the pure DP6 results, which support the observations of RPC followed by melting in the rewarming phase. It is noted that those rates of

cooling and rewarming are considered very slow in the context of vitrification, which supports the effort to achieve large-scale vitrification in due course.

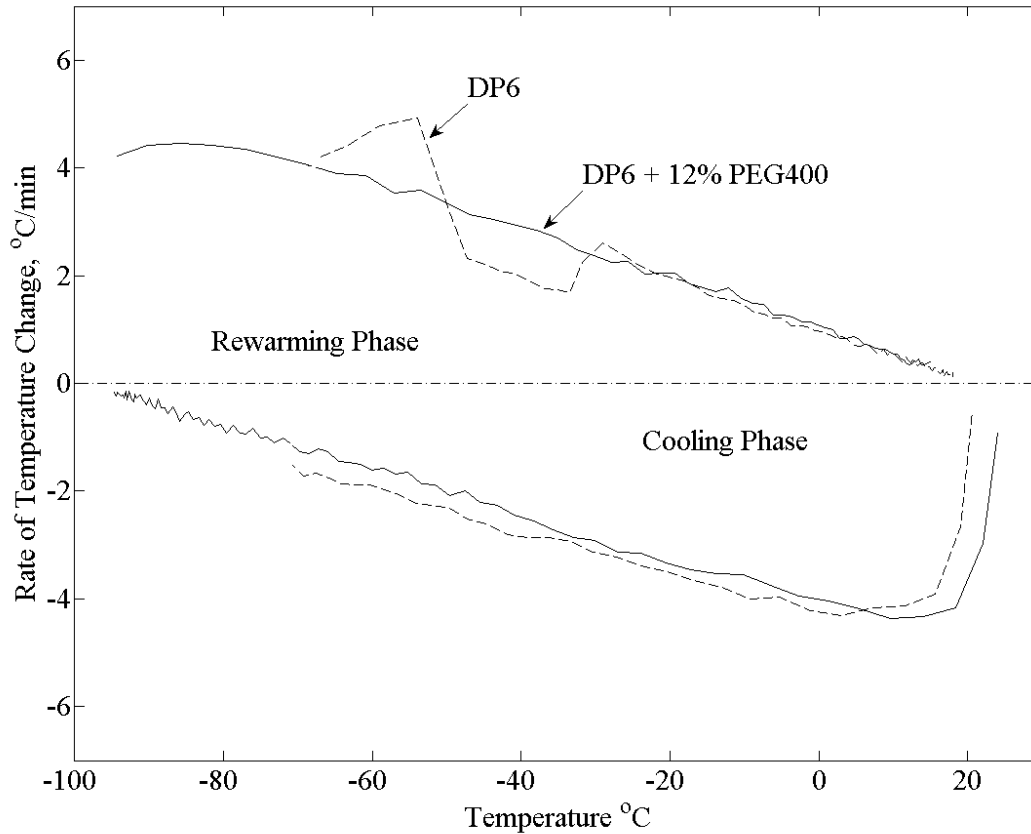


Figure 2.4: Cooling and rewarming rates for the two experiments shown in Fig. 2.3 [2]

Figures 2.5-2.8 display experimental results, whereas Table 2.1 lists parametric estimation results for the corresponding thermal expansion coefficient. Figure 2.5 displays the effect of SIMs on thermal expansion of DP6 in the presence and absence of bovine muscle specimens. In the absence of tissue specimens at -55°C for example (which is the onset of crystallization for pure DP6 at the corresponding thermal history, Fig. 2.4), the thermal strain increases by 8% to 11% when the different SIMs are added, with 12% PEG400 displaying the most significant effect. Suppression of crystallization is evident when SIBs are combined, as the minimum temperature achieved (point B on Fig. 2.3) has been significantly lowered.

Table 2.1: Coefficients of best-fit polynomial approximation of thermal strain, $\varepsilon = a_2 T^2 + a_1 T + a_0$, and the thermal expansion, $\beta = 2a_2 T + a_1$, where R^2 is the coefficient of determination.

Solution	Material	Temperature Range, °C	$a_0 \times 10^4$	$a_1 \times 10^4$	$a_2 \times 10^7$	R^2	n	Source
DP6	Pure solution	0...-55	2.472	1.992	2.705	0.9967	6	Current
	Bovine muscles	0...-45	-4.276	1.957	11.50	0.9915	7	Current
	Goat Artery	20...-40.5	-44.47	1.653	10.41	0.9984	6	[37]
DP6 + 12% PEG400	Pure Solution	0...-95	-4.959	2.313	-0.2188	0.9991	6	Current
	Bovine Muscle	0...-85	9.822	2.118	1.697	0.9845	6	Current
	Goat Artery	0...-80	-4.866	2.392	1.777	0.9896	6	Current
DP6 + 6% 1,3-CHD	Pure Solution	0...-80	0.2699	1.957	-0.6272	0.9963	7	Current
	Bovine Muscle	0...-80	-13.66	2.175	4.411	0.9823	7	Current
	Goat Artery	0...-80	-5.477	2.232	1.054	0.9974	5	Current
DP6 + 6% 2,3 Butanediol	Pure Solution	0...-90	4.518	2.080	0.6309	0.9932	6	Current
	Bovine Muscle	0...-85	-11.17	2.094	1.431	0.9895	6	Current
	Goat Artery	0...-90	-11.04	1.912	0.7383	0.9937	5	Current

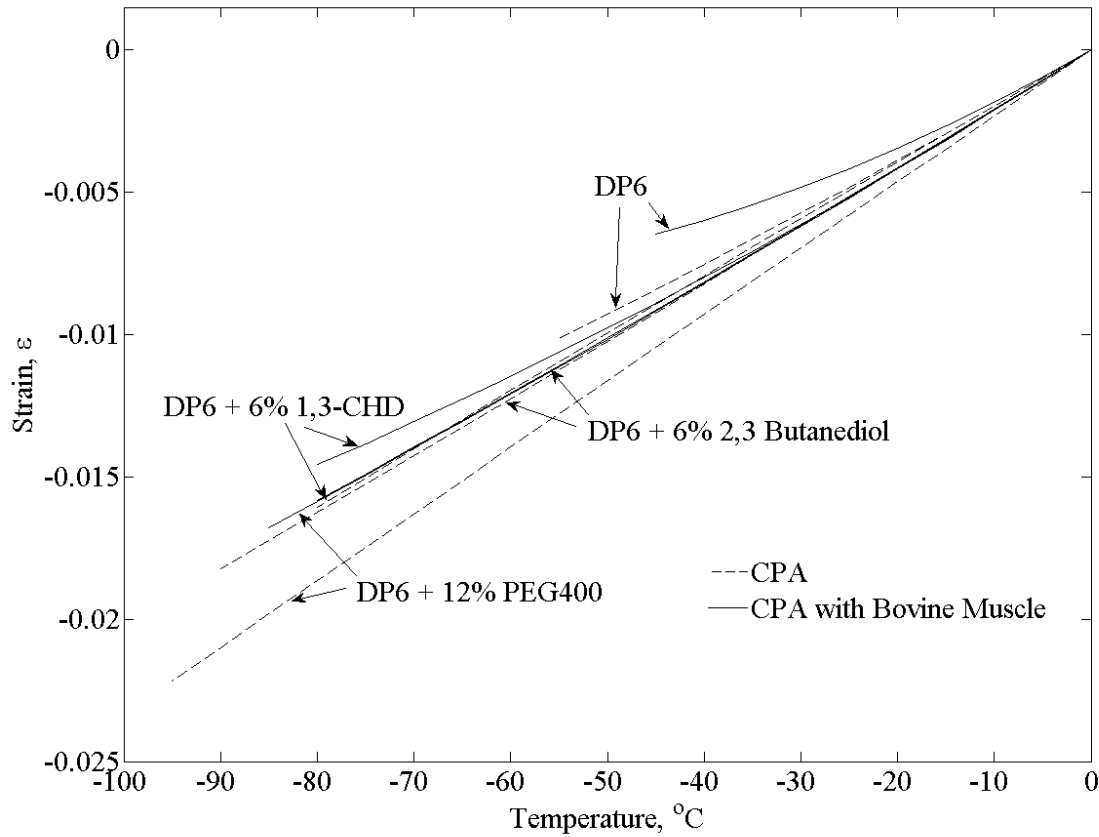


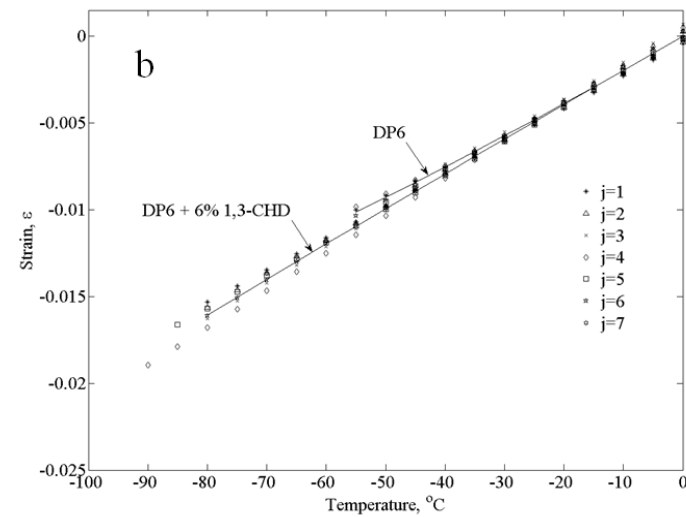
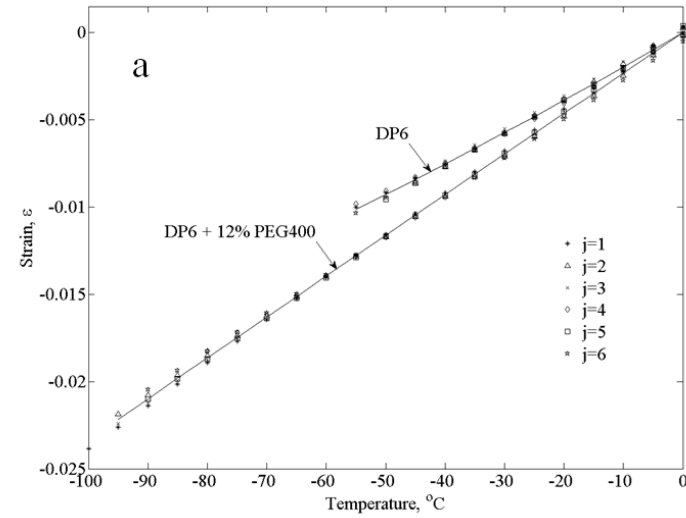
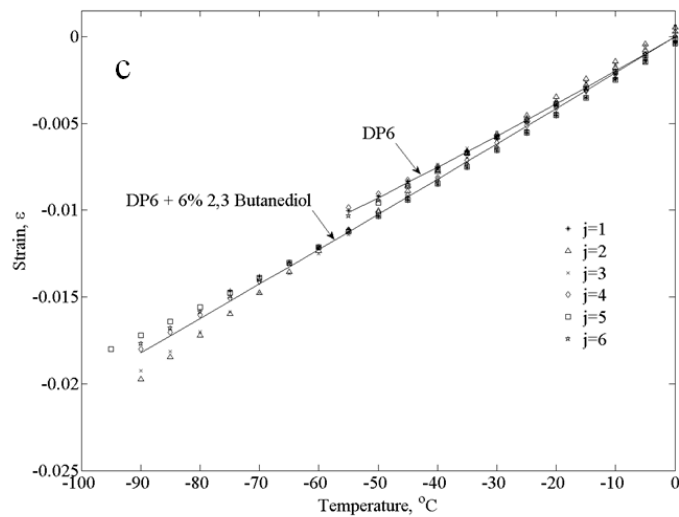
Figure 2.5: Polynomial approximation of the thermal strain for DP6 combined with various SIMs in the presence and absence of bovine muscle specimens [2].

In order to demonstrate repeatability and consistency, Fig. 2.6 presents all experimental data used to approximate the polynomials displayed in Fig. 2.5, for experiments in the absence of tissue specimens. In general, data scattering for DP6+12%PEG400 is at a narrower range than that found for DP6 combined with the other two SIMs. In fact, it simply appears as one would expect from a cocktail with a higher concentration than DP6. The effects of 6% 1,3-CHD and 6% 2,3 butanediol are expressed in increased data scattering, which is likely to be associated with the stochastic nature of ice nucleation and the SIM interference with crystal growth. Nevertheless, the absolute volume fraction that this strain scattering represents is less than 0.25% (i.e., $\epsilon=0.0025$). While such a small volume represents insignificant portion of crystals, if indeed the scattering is directly related to crystallization, such a variation in strain may be quite significant in solid mechanics analysis. In general, while a ductile material, such as the tissue above freezing temperatures, may sustain strains of the order of 1%, strains of a smaller order may lead to

fracture formation in a brittle material such as glass. One example of generating such strains would be when cooling of an organ, where its outer portion vitrifies first due to a radial process of heat transfer, which results in applied forces on the inner-warmer region. In such a case, the outer surface would experience tensile circumferential stresses, which can potentially lead to fracture propagation from the surface inwards.

With regard to the bovine muscle experiments displayed in Fig. 2.5, CPA-SIM cocktail permeation was achieved by immersion of approximately 1.5 ml of tissue into 3 ml of full concentration solution in three steps. These steps are not optimized for tissue functionality nor viability, as the experimental protocol is aimed at physical testing only. In order to test the assumption that the solution fully equilibrates, bovine muscles permeated with DP6 + 12% PEG400 were immersed for varying time periods of 2, 4, 8, 12, 24, and 48 hours, with each step taking up to a third of the complete immersion time. Based on those tests and for data analysis based on the cooling portion of the curve (Section A-B in Fig. 2.3), there appears to be no correlation between the immersion time and the measured thermal expansion. While not relevant to thermal expansion measurements in the current study, RPC was evident for shorter immersion times for bovine muscles permeated with both DP6 + 12% PEG400 and DP6 + 6% 1,3-CHD. Regardless of permeation time, RPC was always evident in experiments performed on bovine muscles permeated with DP6 + 6% 2,3 butanediol. In general, the critical rewarming rate to prevent crystallization is higher in magnitude than the critical cooling rate to prevent crystallization in the process of vitrification. However, the specific cooling rates and the kinetics of SIB permeation are yet to be explored by means of DSC and spectroscopy, respectively. Interesting to note that in the pure DP6 experiments in the current study, Unisol was replaced with EuroCollins as a buffer solution, which had no effect on thermal expansion results, as compared with a prior study [37].

Figure 2.2: Thermal strain data from all the individual experiments used for the polynomial approximations displayed in Fig. 5: (a) DP6+12% PEG400 (b) DP6+6% 1,3-CHD, and (c) DP6+6% 2,3 butanediol; j is the experiment number and solid lines represent the best-fit polynomial approximations [2].



It can be seen from Fig. 2.5 that permeated tissue specimens contract less than the pure cocktails, which is consistent with previous studies in the absence of SIMs [37]. However, lower minimum temperatures were achieved in the current study, due to the particular combinations of CPA and SIMs. Such a differential expansion between the tissue and the surrounding CPA has implications on the design of packaging for vitrified materials, in an effort to reduce resulting fractures. It has been shown previously that such a difference may result in fracture initiation in the surrounding solution [52]. Once fractures are triggered, their propagation requires smaller driving forces, and it is difficult to predict where or by what fractures may be arrested. In general, a thermal expansion difference of up to 15.1% is observed between tissue permeated with a CPA-SIM cocktail and the thermal expansion of the pure cocktail.

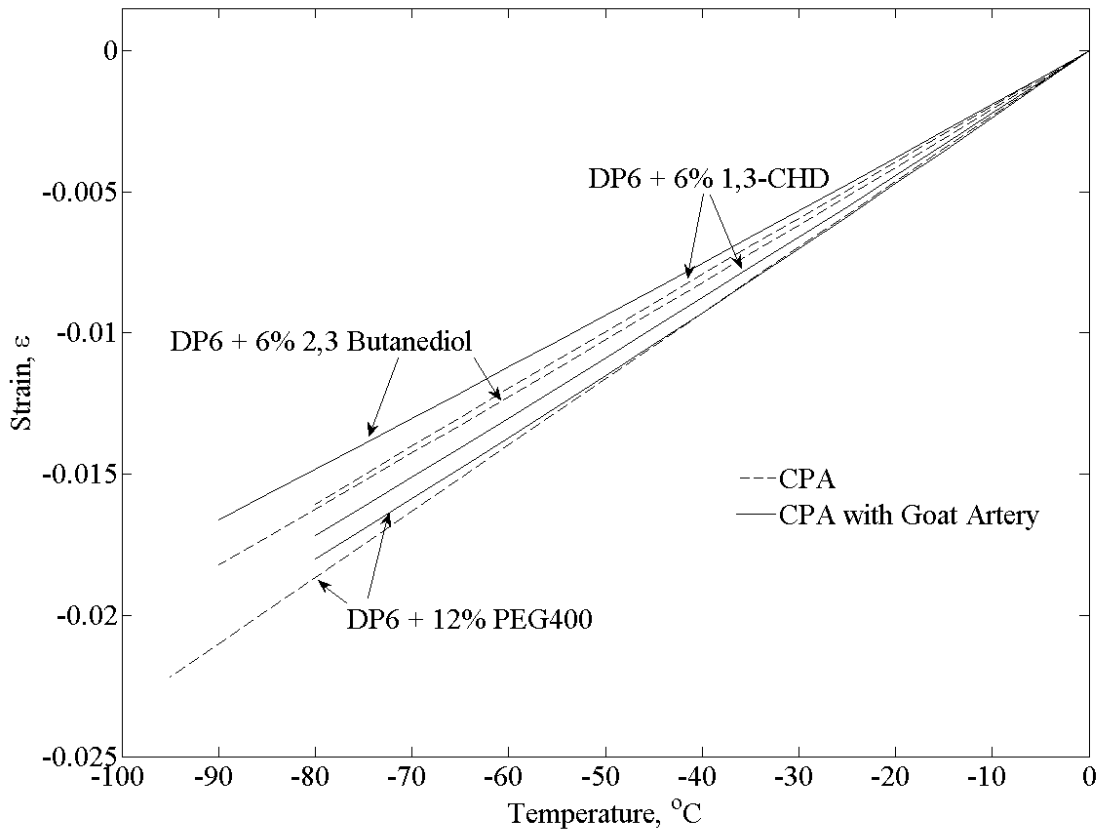


Figure 2.7: Polynomial approximation of the thermal strain for DP6 combined with various SIMs in the presence and absence of goat artery specimens [2].

Figure 2.7 displays results for goat artery samples, following a similar procedure to the one described above for bovine muscle samples. The thermal strain of DP6 + 12% PEG400 in the

absence of tissue samples is in a much closer range with permeated arteries (up to 3.5% for a temperature range of 80°C) than with permeated muscle specimens (up to 15.1% for a temperature range of 80°C). Interestingly, the thermal strain of goat arteries permeated with 6% 1,3-CHD is actually greater than that of the solution itself from an unknown reason at this stage (up to 6.5% for a temperature range of 80°C) and is quite similar to that of goat arteries permeated with DP6 + 12% PEG400. Finally, the thermal strain for goat arteries permeated with 6% 2,3 butanediol showed less thermal strain than that of bovine muscles permeated with that solution (up to 8.7% for a temperature range of 80°C). Overall, thermal strain in permeated goat arteries tended to be closer to that of the pure solution than to that of permeated bovine muscles. As indicated above, these differences may be associated with techniques and effects of permeation, with an optimal procedure remaining to be explored in future studies for tissue viability and functionality. Following a similar procedure to the one presented in [40], analysis of the current system indicates absolute uncertainty range of 8% for a single independent measurement with the experimental system, including systematic errors originated from calibration, geometrical dimensions, and the characteristics of the pressure transducer (gain, bias, repeatability, etc.). Taking into account that the above observations rely on differences between polynomial approximations based on datasets and not on single independent measurements, and taking into account that all datasets were obtained with the system after calibration, the above observations are deemed significant.

The current experiments are conducted at very low cooling rates and, therefore, are deemed relevant to scale-up efforts of cryopreservation by vitrification. In particular, the typical cooling rates displayed in Fig. 2.4 were found to be at the threshold for vitrification of goat artery specimens permeated with DP6 + 6% 1,3-CHD. Here, Fig. 2.8(c) displays results from ten experimental runs under identical conditions, where the results could be grouped into two groups of five: (i) crystallization is not evident—the strain curve is close to linear and scattering of results is in a very narrow range (results included in Table 2.1), and (ii) crystallization is evident—the strain curve is quadratic in nature and scattering of results is significant (results omitted from Table 2.1). The reason for smaller strains during crystallization is that cooling with no phase change is associated with contraction, while ice crystallization is associated with volume expansion of the pure water. These are competing effects, causing the overall strain to decrease. Since water crystallization is a dramatic effect of about 9% volume increase, the

relatively small changes in the strain rate in Fig. 2.8(c) suggest partial vitrification only (more significant crystallization is shown in Section B-C of Fig. 2.3).

Figure 2.8: Thermal strain data from all the individual experiments used for the polynomial approximations displayed in Fig. 7: (a) DP6+12% PEG400 (b) DP6+6% 1,3-CHD, and (c) DP6+6% 2,3 butanediol; j is the experiment number and solid lines represent the best-fit polynomial approximations [2].

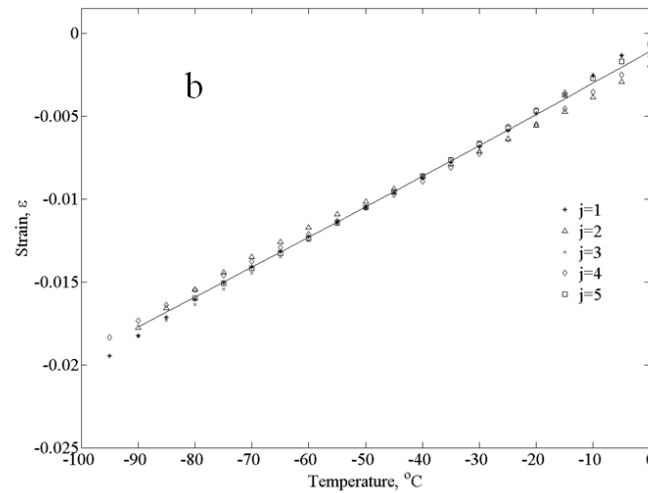
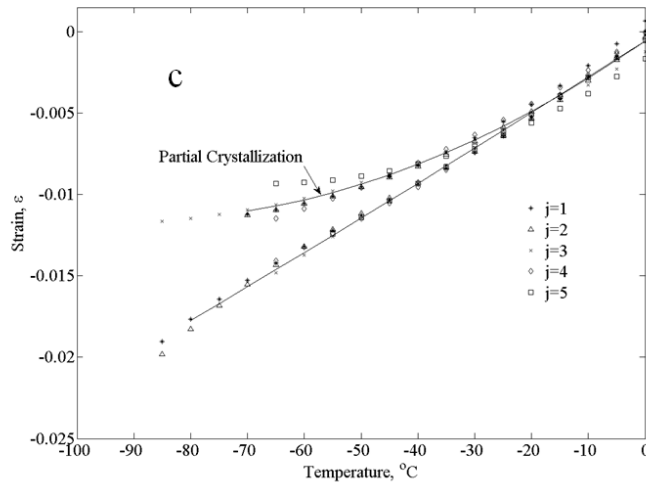
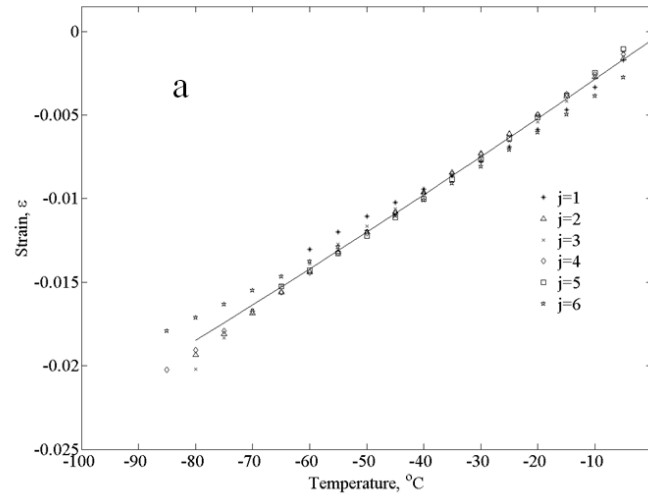


Figure 2.9 displays estimation for the extent of partial crystallization in Fig. 2.8(c). This estimation is based on the difference between the two best-fit curves for goat arteries permeated with DP6 + 6% 1,3-CHD (for small strains, the volumetric strain is triple the linear strain displayed in Figs. 2.5-2.8). Note that uncertainty in strain measurements is estimated as 8%, which is the strain difference between the different curves at -30°C , a point at which the extent of partial crystallization is estimated as 1.8% (Fig. 2.9). Since the maximum value of partial crystallization presented in Fig. 2.9 is 15.5%, partial crystallization is found to be a significant effect in this experimental set. Nevertheless, the shape and distribution of crystals in the system remains unknown at this stage. It is reemphasized that the SIMs selected for this study are considered not to prevent ice nucleation but to prevent the growth of crystals. The presence of nuclei or small portion of ice crystals is not necessary detrimental to the success of cryopreservation via vitrification, as has been demonstrated recently on blood vessels at marginal cooling rates [58].

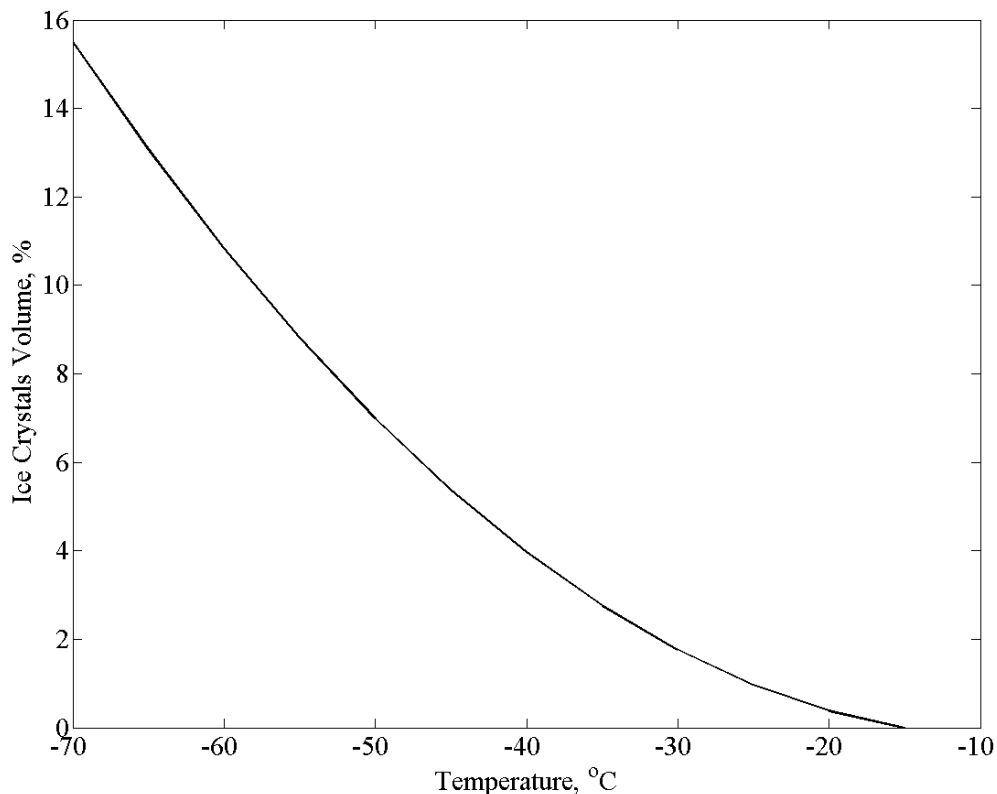


Figure 2.9: Volume fraction of ice crystals in the case of partial vitrification displayed in Fig. 2.8(c): goat artery specimens permeated with DP6+6% 1,3-CHD [2]

2.6 Summary and Conclusions

Investigation of solid mechanics effects in cryopreservation represents a largely uncharted area of research. To the best of our knowledge, this study represents the first published example of an investigation into the thermo-mechanical effects associated with the application of SIMs to vitrification. This study is focused on measuring the driving mechanism to thermo-mechanical stress—the physical property of thermal expansion. This study focuses on the upper part of the cryogenic temperature range, where the CPA behaves as a fluid for all practical applications. Concurrent efforts were devoted to measure thermal expansion at lower cryogenic temperatures, where the vitrified material behaves like a solid.

Results of this study demonstrate that the SIMs under investigation facilitate DP6 vitrification at low cooling rates in the range of 1 to 4 °C/min, which relaxes the constraints on large-scale cryopreservation. In fact, cooling pure DP6 alone always resulted in crystallization at some point in the process subject to the same thermal protocol. SIMs were found effective not only in suppressing crystallization but also in preventing RPC. It appears that the addition of SIM can potentially lead to two competing effects: (i) increased thermal expansion of the CPA-SIM cocktail, which may lead to higher thermo-mechanical stresses for a particular cooling rate, and (ii) decreased cooling/rewarming rates necessary to achieve a high degree of vitrification. Nevertheless, the magnitude of each effect will be dependent upon the specific setup and geometry of the problem and, thus, it is impossible to generate general rules on which effect will be more significant.

The promising results of this study suggest the additional resources should be devoted to study the application of SIM to vitrification, including, tissue viability and functionally, kinetics of CPA-SIM permeation, and other thermo-physical properties of the CPA-SIM-tissue system.

Chapter 3: Thermal Expansion Measurements in Lower Cryogenic Temperatures

This chapter expands upon a recently published study in [4]. In this study, the thermal expansion of tissues permeated with DP6+SIM was measured in the lower part of the cryogenic temperature range, where the material acts as an elastic solid. The results of this study, were combined with the results from a previous study [2] to construct a combined thermal strain curve that goes from room temperature down to approximately -160°C . The degree to which the coefficient of thermal expansion matches at the overlap of these two datasets (each collected using a different experimental setup) provides experimental verification for the measured data and techniques.

3.1 Experimental Setup

The device used to measure thermal expansion in the lower part of the cryogenic temperature range was previously developed and validated by Rabin and Jimez. [3], and is presented here in brief for the completeness of presentation. With reference to Fig. 3.1, the experimental system consists of six units: (1) a cooling chamber; (2) a low pressure cooling unit for slow cooling; (3) a high pressure cooling unit for rapid cooling; (4) a closed-loop electrical heating unit for thermal control of the cooling chamber; (5) a computerized sensory unit to record specimen elongation and thermal history; and (6) a specimen gripping unit and telescopic glass tubing for displacement measurements, where the displacement sensor operates at room temperature. The experimental system was designed and constructed at the Biothermal Technology Laboratory at Carnegie Mellon University.

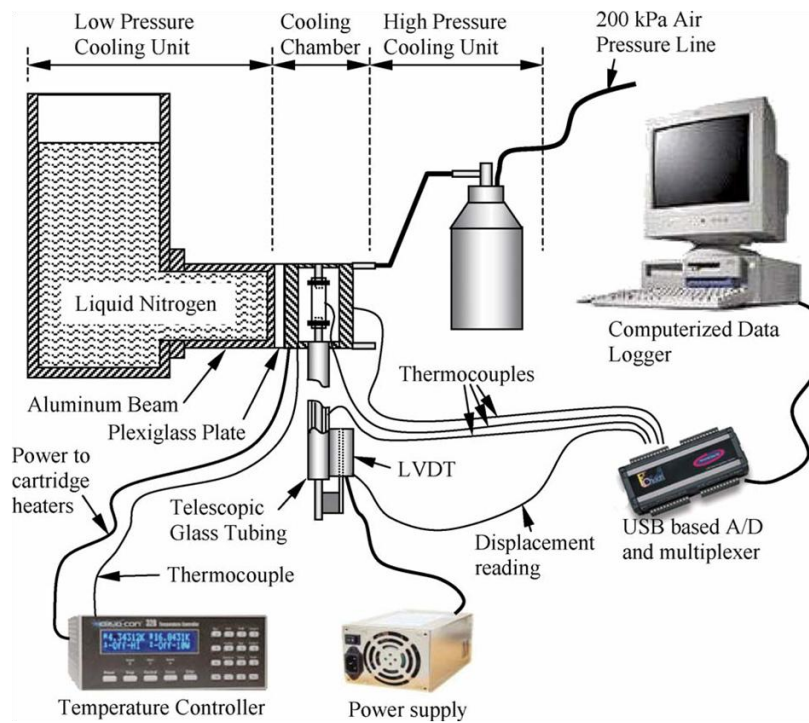


Figure 3.1: Schematic illustration of the experimental setup to measure the thermal expansion in the current study [3] (with permission).

Figure 3.2 displays a schematic illustration of the cooling chamber assembly. The cooling chamber is constructed of a yellow brass block. Due to the high thermal conductivity of brass, ($k = 83 \text{ W/m-K}$) the cooling chamber behaves as a lumped system in the thermal sense. A groove is machined along one side of the block in order to accommodate the blood vessel specimen and is covered with a brass plate. The cooling chamber is attached to an aluminum beam which extends from the low pressure cooling unit, which operates at atmospheric temperature. Between the cooling chamber

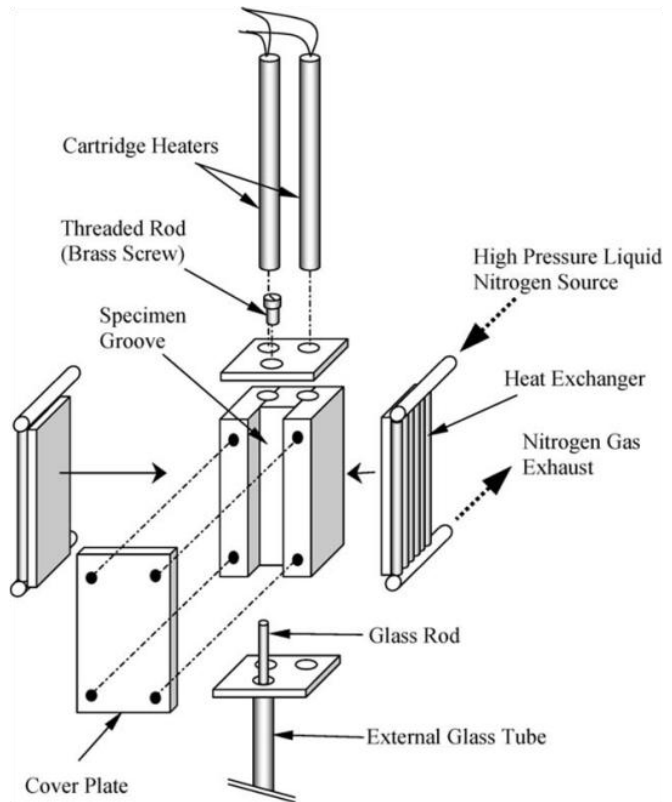


Figure 3.2: Schematic illustration of the cooling chamber of the experimental setup displayed in Fig. 3.1 [3] (with permission).

and the aluminum beam is a thin Plexiglass plate which acts as a thermal barrier (as shown in Fig. 3.1). This slows down the heat transfer and conserves liquid nitrogen stored in the low pressure cooling unit. The contact face of the chamber with the Plexiglass plate is on the face opposite of the cooling chamber groove. The high pressure cooling unit consists of two heat exchangers, one on each side of the cooling chamber, liquid nitrogen container, and a portable air pressure container. The heat exchangers are connected in parallel to the high pressure liquid nitrogen container. The high pressure cooling unit is manually operated while the low pressure cooling unit is active throughout the experiment.

Two cylindrical holes are drilled along the cooling chamber, to accommodate a pair of cartridge-electrical heaters, which are connected in parallel to the temperature controller and power supply. A copper-constantan thermocouple (type T) is connected to the cooling chamber in a drilled hole between the electrical heaters and the groove of the chamber, which closes the feedback loop of the control system.

The computerized sensory unit comprises a regular desktop computer, an analog to digital converter and multiplexer in one unit (OMEGA, OMB-DAQ 55) an array of T-type thermocouples, a linear variable differential transformer (LVDT) sensor and a power supply to excite the LVDT. In order to thermally isolate the LVDT from the rest of the experiment, a system of telescopic glass tubing was used—a tube and a rod. The glass tube is vertically connected to the cooling chamber at one end, and to the LVDT coil at the other end. The glass rod is connected to the specimen at one end, and to the LVDT core at the other end. With reference to Fig. 3.2, the blood vessel specimen is connected onto a threaded screw, which extends from the plate covering the top side of the cooling chamber groove.

To operate the system, first the liquid nitrogen reservoir of the low pressure cooling system is filled—in order to pre-cool the system, while the cartridge heaters are turned on—in order to hold the cooling chamber at a steady initial temperature of 0°C. After the system has reached steady state, the heater is turned off and the high-pressure cooling system is activated. The high pressure cooling unit, working simultaneously with the low pressure cooling unit, allows the cooling rate to be high enough ($\sim -40^{\circ}\text{C}/\text{min}$) to prevent crystallization while the system is cooled down to the minimum temperature (typically between -160°C and -170°C). Next, the high pressure system is turned off and the heater is turned back on until the system reaches room temperature. The average rewarming rate is $8.25^{\circ}\text{C}/\text{min}$, starting at $11^{\circ}\text{C}/\text{min}$ upon activation

and reaching $5.5^{\circ}\text{C}/\text{min}$ at -80°C , which is the upper temperature range for data collection in this study (see [3] for further details on system operation).

The contraction of the cooling chamber, the telescopic tubing, and the blood vessel differ, which causes an axial movement of the glass rod inside the glass tube. This moves the core of the LVDT relative to its coil. The LVDT core movement is recorded through the USB-A/D converter and multiplexer, concurrently with the thermal history of the specimen and cooling chamber. With both the axial displacement and the temperature history, the thermal strain of the blood vessel specimen and its thermal expansion coefficient can be calculated as described below.

Each experiment produces a continuously varying thermal strain response as temperature rises and is sampled at a rate of 1 Hz. The multiplexer was set to measure data from seven different inputs with a measurement duration of 110ms. This led to a maximum time delay of 0.77s between the first and last measurements. The maximum rewarming rate for analyzed data (Fig. 3.3) is about $9.5^{\circ}\text{C}/\text{min}$. It follows that the maximum temperature increment between consecutive measurements is 0.16°C . Due to uncertainty relating to the actual time of measurement within each sampling cycle (7 inputs at 110 ms each, results in a sampling cycle of 0.77s), the uncertainty in sampled temperature may reach up to 0.12°C . This uncertainty is significantly smaller than the inherent uncertainty for the T-type thermocouple (0.5°C) used in the current system. Nonetheless, the linear thermal expansion coefficient—the inferred property in the current experimental investigation—is a monotonic and very slow changing property. The effect of 0.16°C temperature increment on the correlation between the thermal expansion coefficient and temperature is deemed negligible (see [3] for more detailed uncertainty analysis).

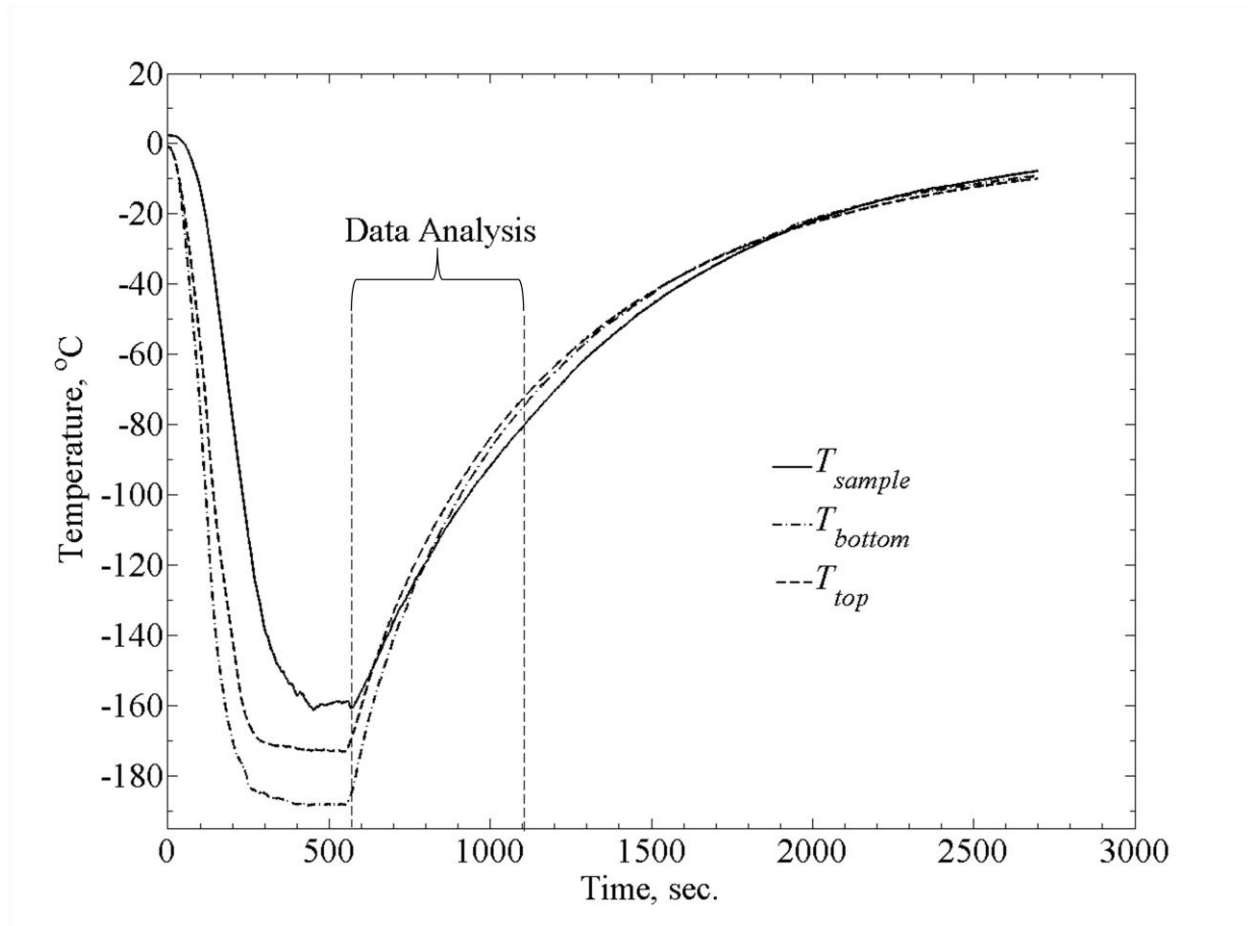


Figure 3.3: Typical thermal history during experimentation, where T_{sample} is the blood vessel temperature at its mid-height, and T_{top} and T_{bottom} are the temperatures measured at the top and bottom of the cooling chamber [4].

With reference to [3], two modifications are integrated into the experimental setup: (i) the glass rod and threaded screw diameter used in this study were changed from 3mm to 1.5mm, to be compatible with smaller size blood vessel specimens, and (ii) a higher precision power supply was used in the current study—Hewlett, Packard 6228B, instead of a Bested, Model BPS-2004-4U. These modification necessitated recalibration of the experimental system, following the process outlined in [3].

3.2 Artery Sample Preparation

All tissues used in this experiment were donated by a local slaughterhouse. No animals were sacrificed specifically for the purpose of the current study. The main carotid artery was harvested from goats (which were sacrificed for other purposes). Tested samples had a diameter

in the range of 3 to 5 mm, length in the range from 40 to 52 mm, and a wall thickness of about 1 mm (diameter and wall thickness have no effect on the thermal expansion measurements). Samples were immersed in SPS-1 organ preservation solution (Organ Recovery Systems, Inc. Itasca, IL) immediately after harvesting and stored at 4°C for a period between one and five days. This time period was selected due to availability of specimens and appeared to have no effect on experimental results. While storing the specimens in such conditions is likely to affect viability and functionality of the blood vessel, it has no effect on its thermo-physical properties, as has been demonstrated previously [2,42]. Following the procedure outlined in [2], each specimen was immersed in the DP6 + SIM solution for 2 h before testing.

The formulations for DP6 and VS55 were presented previously in section 2.3 of this thesis. While many SIMs could be selected, the choice of practice is based on recent experience developed by the current research team [2,20], the following cocktails have been tested: DP6 + 12% PEG400 (n = 5), DP6 + 6% 1,3-CHD (n = 5), and DP6 + 6% 2,3-BD (n = 4), where n is the number of specimens and each specimen was tested twice (a total of 2n experiments). Two experiments were performed on each specimen to investigate the effect of repeated cooling-thawing cycles. Experiments were repeated on multiple arteries in order to investigate variance among tissue samples as well as to eliminate any systemic and preparation errors. All SIMs, PEG400, 1,3-cyclohexanediol (98% mixture of cis and trans isomers), and 2,3-butanediol (2R,3R isomer), were obtained from Sigma-Aldrich (St. Louis, MO) and DP6 was obtained from Cell and Tissue Systems, inc. (Charleston, SC).

3.3 Data Analysis

The experimental protocol, a detailed mathematical analysis of the system, and uncertainty analysis have all been presented previously [3,42]. Key equations and a brief description of the data analysis process are presented here for the completeness of presentation. Due to the two modifications described above, the system had to be recalibrated. First, a voltage-displacement curve was obtained, by driving the glass rod with a depth micrometer and recording the LVDT voltage output.

The LVDT displacement reading is the sum of:

$$\Delta L_v(t) = \Delta L_s(t) + \Delta L_g(t) - \Delta L_c(t) \quad (3.1)$$

where ΔL_s is the tissue sample elongation, ΔL_g is the elongation of the portion of the glass rod that extends into the cooling chamber, and ΔL_c is the elongation of the cooling chamber. In order to obtain ΔL_s , the unknown quantity ($\Delta L_g - \Delta L_c$) has to be measured experimentally, following the procedure described in [3]—this quantity is unique to the specific experimental setup.

Finally, the thermal strain (the relative contraction) of the blood vessel is calculated by:

$$\varepsilon = \frac{\Delta L_s}{L_s} \quad (3.2)$$

where L_s is the initial length of the specimen. The linear thermal expansion coefficient is the rate of change of thermal strain with respect to temperature:

$$\beta = \frac{d\hat{\varepsilon}}{dT} \quad (3.3)$$

where $\hat{\varepsilon}$ is a polynomial approximation of the temperature dependence of the strain, ε . While the property of thermal expansion is intrinsic, the thermal strain is a relative measure specific to a particular process (i.e. the integral of thermal expansion over temperature along the process).

3.4 Results and Discussion

Figure 3.3 displays a typical thermal history in a thermal strain experiment. Due to the large temperature distribution in the cooling chamber during the cooling phase of the experiment, data analysis in the current study is focused on the rewarming phase, when the temperature distribution is moderate (less than $\pm 7^\circ\text{C}$ from the average in the experiment displayed in Fig. 3.3). Data collection starts at the lowest temperature achieved and continues until the specimen reaches a certain temperature, T_B , (Fig. 3.4a) where the material can no longer be approximated as solid. While the precise location of T_B may vary between experiments, based on the data collected in the current study and the conclusions drawn in [42], -80°C appears to be below that temperature threshold for all experiments. Hence, data analysis in the current study is focused on the temperature range of -80°C (point B) to the lowest temperature obtainable for a given experiment (point C)—typically in the range of -170°C to -160°C . A second order polynomial has been used in a previous study to approximate the thermal strain at low temperatures [42], attempting a 2nd order fit, resulted in a coefficient of determination (R^2) value of 0.9914. Results of this study suggest a better fit with a 4th order polynomial, resulting in an R^2 value of 0.9995

(Fig. 3.4(b)). Data obtained in this study on the thermal expansion of DP6 matched reasonably well previously obtained data [42]. However, due to the slow rewarming rate (between 5.5 and 9.5°C/min), which is below the critical rate of 185°C/min, we are unable to exclude rewarming phase crystallization effects, and that data was not included in the current report.

While the property of thermal expansion is intrinsic, the thermal strain is an integral property (the integral of the thermal expansion coefficient with respect to temperature), which is dependent upon an initial condition. In these experiments, the initial condition is the initial temperature, which varies between experiments. Since each experiment starts at a slightly different temperature, the approximation of $\hat{\epsilon}_j$ from a specific experiment, j ($j = 1, \dots, 2n$), needs to be shifted in the ϵ direction (vertical direction) within the ϵ -T plane so that the data sets overlap. Once one experiment is arbitrary selected as a reference, $\hat{\epsilon}_k$ ($k = j$, $j = 1, \dots, 2n$), experimental results from all other experiments are shifted by a constant value $\Delta\hat{\epsilon}_j$, so that the parameter F_j is minimized (a different value for each experiment):

$$F_j = \sum_{i=1}^m [\hat{\epsilon}_{k,i} - (\hat{\epsilon}_{j,i} - \Delta\hat{\epsilon}_j)]^2 \quad (3.4)$$

where i represents all the overlapping points from the polynomial approximations $\hat{\epsilon}_k$ and $\hat{\epsilon}_j$. Due to the exponentially decaying rewarming rate, Eq. (3.4) is used on polynomial approximations of the original experimental datasets, rather than on raw data; otherwise it would have over-weighted the differences at higher temperatures. In practice, the temperature range of interest was discretized in 5°C increments, with m value typically equal to 16. Decreasing that temperature increment to 0.16°C, which is the maximum temperature increment at 1Hz (as discussed above), had insignificant effect on $\Delta\hat{\epsilon}_j$ of less than 1.52% of full scale.

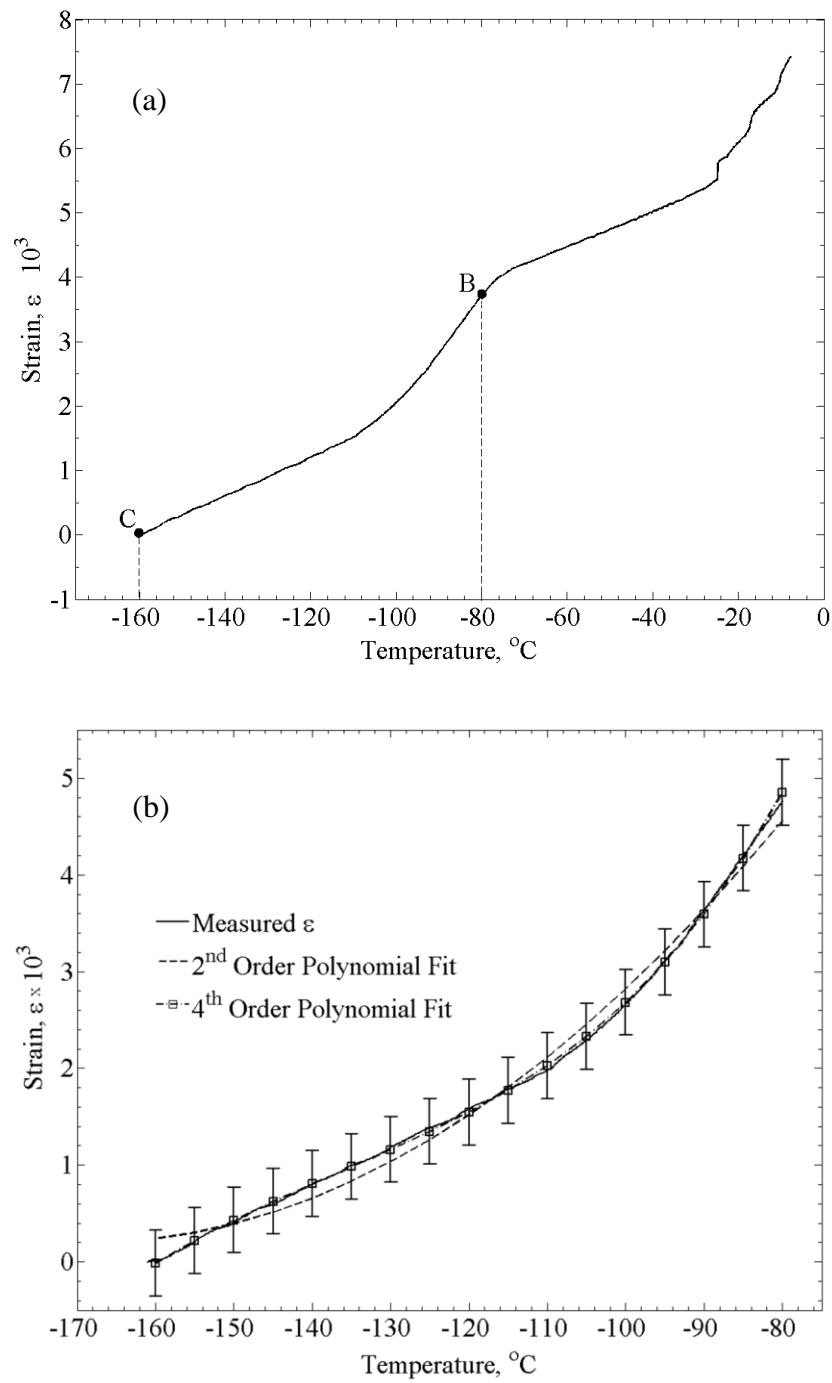


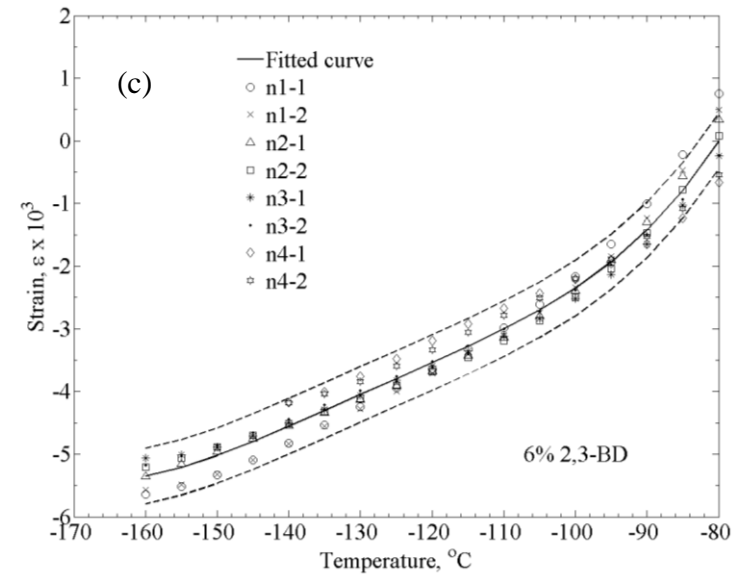
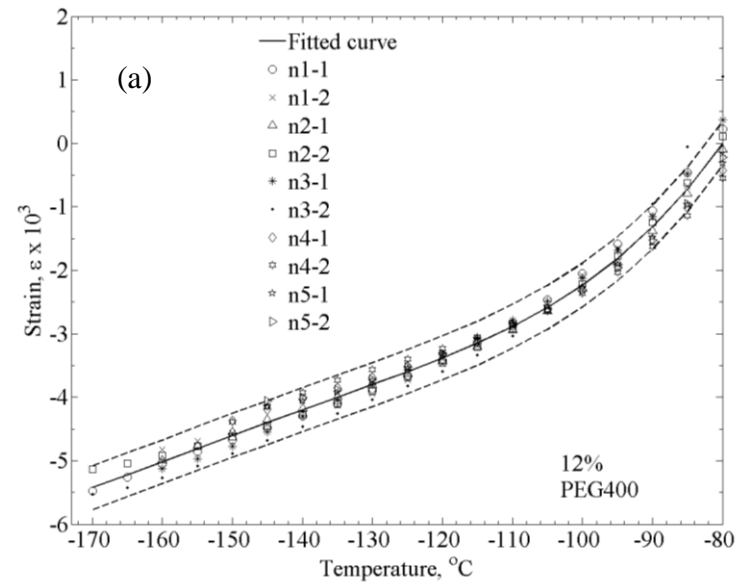
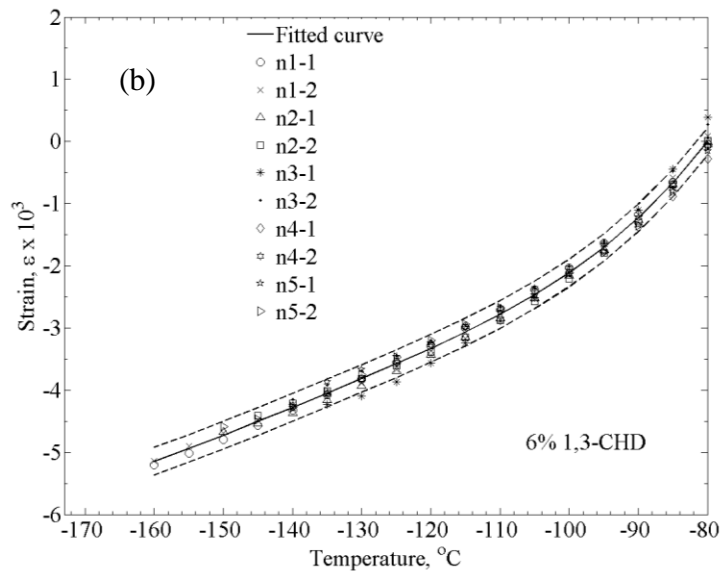
Figure 3.4: A typical strain-temperature curve obtained with the experimental system: (a) section B-C is the analyzed segment, where the material follows the expected thermal behavior of a vitrifying material, and (b) analyzed data from the same experiment using a 2nd and 4th order polynomial; error bars indicate $\pm 2\sigma$ [4].

Finally, a polynomial approximation, $\hat{\epsilon}$, is estimated for the combined shifted data from all the experiments. Figure 3.5 displays the thermal expansion data for goat arteries permeated with each of the three SIMs under investigation. The uncertainty range illustrated in Fig. 3.5 represents a 2σ range, which is consistent with the odds of 1:20 for a particular measurement to be outside of this range [59]).

In the process of estimating uncertainty, a consideration must be given to the fact that the measured parameter is the strain but the inferred parameter is its slope—the linear thermal expansion coefficient. Furthermore, the average slope from all experiments is calculated only after strain curves are shifted to minimize their offset, as described above. It follows that a standard deviation value of the strain distribution, when calculated independently at a particular temperature for all data sets after curve shifting, may represent an overly optimistic estimation of certainty (most likely to occur at the middle of the temperature range). Instead, the uncertainty range in Fig. 3.5 is calculated as the average of all individual uncertainty values calculated at each temperature point, a value which is assumed to better represent the overall uncertainty in experimentation and analysis technique.

Distribution of results for each cocktail out of full range is: $\pm 6.9\%$ for DP6+PEG400, $\pm 4.3\%$ for DP6+1,3-CHD, and $\pm 8.3\%$ for DP6+2,3-BD. The differences between the best fit for each cocktail is within the above uncertainty range as shown in Fig. 3.6, which suggests that differences in thermal expansion between the different cocktails are relatively small. For clarity in presentation, an uncertainty range is presented for DP6+PEG400 only, to display a representative distribution of results.

Figure 3.5: Thermal strain of DP6 combined with (a) 12% PEG400, (b) 6% 1,3-CHD, and (c) 6% 2,3-BD. Symbols represent individual data points, solid lines represent polynomial approximation, and dashed lines represent an uncertainty range of $\pm 2\sigma$ [4].



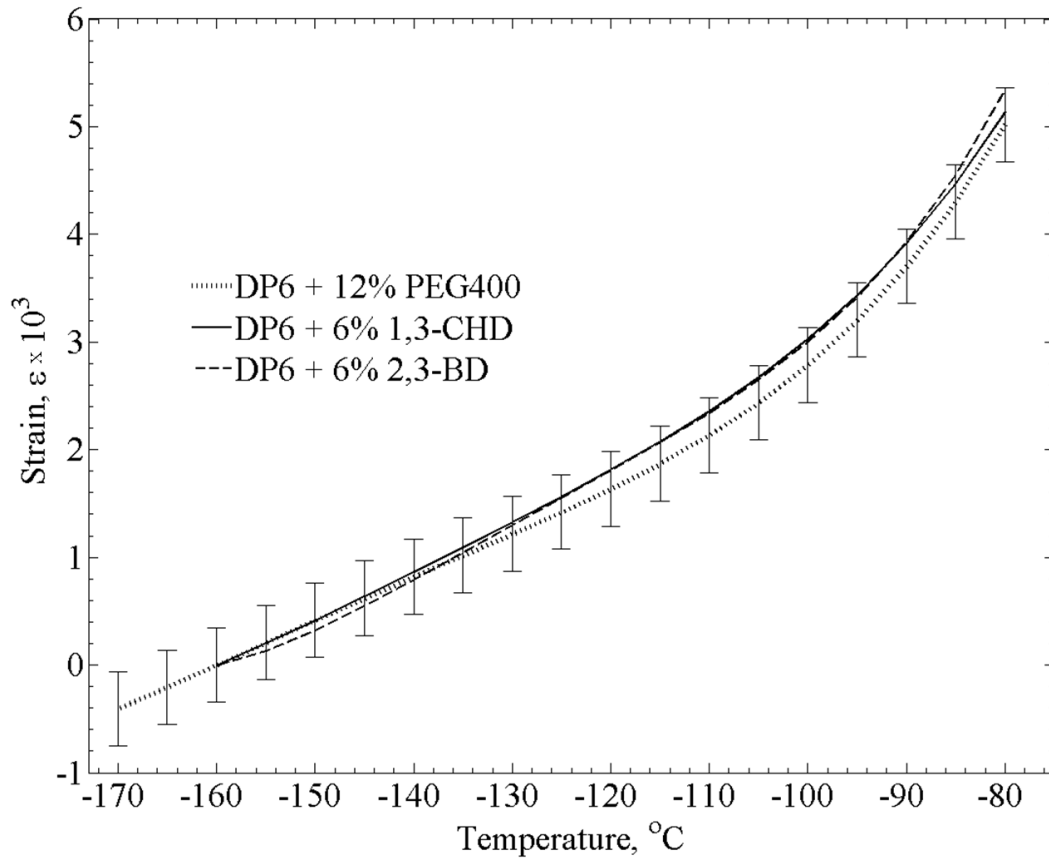


Figure 3.6: Polynomial approximations of the three DP6 + SIM solutions. Since data compilation was performed for the rewarming stage, which started in the temperature range of -170°C to -160°C , a strain value of zero was selected at the reference temperature of -160°C . For clarity in presentation, representative error bars ($\pm 2\sigma$) are displayed for the DP6+12% PEG400 curve only [4]

3.5 Unified Thermal Expansion Curves:

The thermal expansion in the upper part of the cryogenic temperature range, where the material behaves as a fluid, has been recently studied [2], while the current study is focused on the lower part of the cryogenic temperature range, where the material behaves as a solid for the time scale of experimentation. Both datasets include overlapping thermal strain measurements, centered around -80°C , which enables merging the separate sets of data into a unified curve covering the entire cryogenic temperature range. The process for creating the unified thermal expansion curve followed these steps: (i) While taking 0°C as a reference temperature for datasets in the upper part of the cryogenic temperature range, each polynomial approximation for

a specific cocktail was shifted in the ε direction within the ε -T plane, until the strain at this temperature became zero. (ii) While taking -80°C as a reference temperature for datasets in the lower part of the cryogenic temperature range, each corresponding polynomial approximation was shifted, until both datasets for the same cocktail received the same strain value at -80°C . (iii) A fourth order polynomial approximation was fitted to the combined datasets.

Figure 3.7 displays the corresponding three unified curves and Table 3.1 lists the corresponding fitted parameters. For a 2σ range (twice the standard deviation; including 95% of all measured data), distribution of results for each cocktail is found within: $\pm 1.5\%$ for DP6+PEG400, $\pm 1.0\%$ for DP6+1,3-CHD, and $\pm 2.2\%$ for DP6+2,3-BD, all with respect to full range measurements. It was essential to construct the unified thermal expansion curve from the individual polynomial approximations of the subsets (upper and lower parts of the cryogenic temperature range) rather than from the raw data of all experiments combined, in order to resolve issues associated with the variation in conditions inherent to the different experimental studies, such as sampling rate, minimum temperature achieved, and the number of experiments.

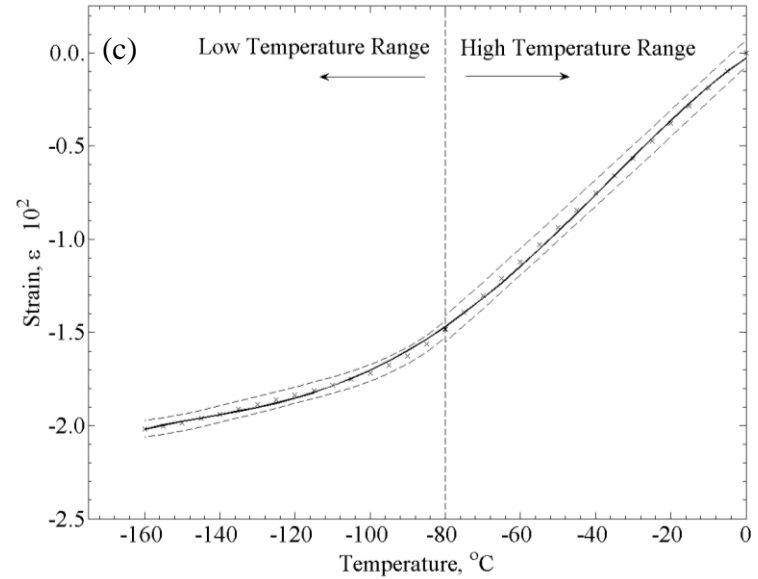
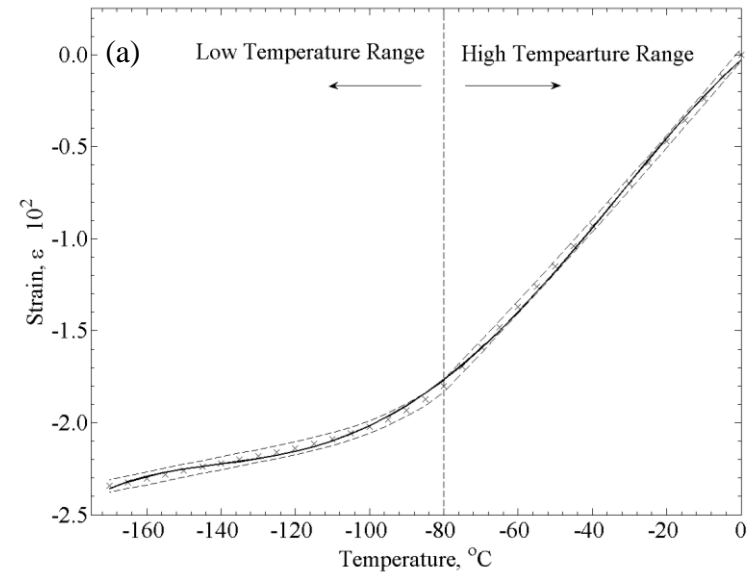
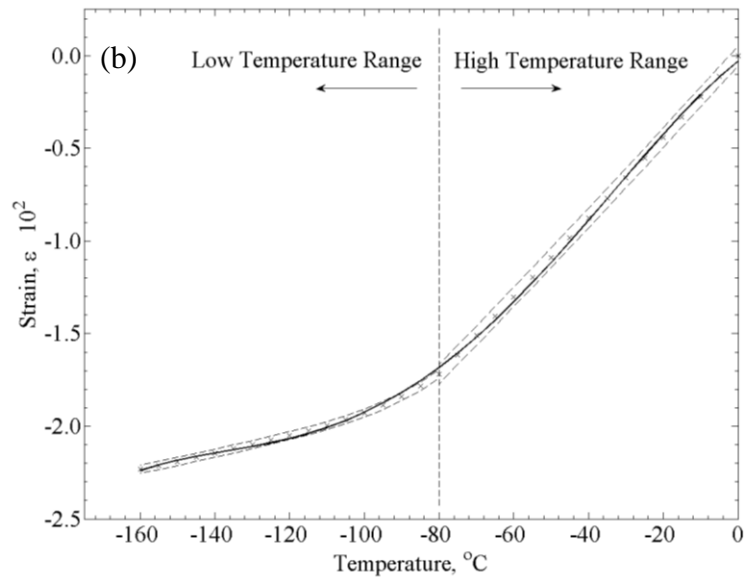
Table 3.1: Coefficients of best-fit approximation of the thermal strain, $\varepsilon = a_1T^4 + a_2T^3 + a_3T^2 + a_4T + a_5$, for selected DP6-SIM mixtures, where the thermal expansion coefficient is given by $\beta = 4a_1T^3 + 3a_2T^2 + 2a_3T + a_4$, and where R^2 is the coefficient of determination.

SIM	Temperature Range, $^\circ\text{C}$	$a_1 \times 10^{10}$ [$^\circ\text{C}^{-4}$]	$a_2 \times 10^7$ [$^\circ\text{C}^{-3}$]	$a_3 \times 10^5$ [$^\circ\text{C}^{-2}$]	$a_4 \times 10^3$ [$^\circ\text{C}^{-1}$]	$a_5 \times 10^2$	R^2	n	Source
12% PEG400	0 to -80	0	0	0.01777	0.2392	0	0.9896	6	[2]
	-80 to -160	1.065	0.6240	1.364	1.358	4.911	0.9833	5	Current
	0 to -160	-0.8668	-0.2995	-0.2358	-0.1757	-0.0275	0.9995	-	Current
6% 1,3-CHD	0 to -80	0	0	0.01054	0.2232	0	0.9974	5	[2]
	-80 to -160	1.155	0.639	1.330	1.283	4.550	0.9943	5	Current
	0 to -160	-0.7969	-0.2771	-0.2210	0.1666	-0.0236	0.9994	-	Current
6% 2,3-BD	0 to -80	0	0	0.007383	0.1912	0	0.9937	5	[2]
	-80 to -160	2.672	1.379	2.668	2.342	7.562	0.9791	4	Current
	0 to -160	-0.5587	-0.2066	-0.1747	0.1442	-0.0209	0.9994	-	Current

In a previous study on DP6 in the absence of SIMs [42], a significant portion of the unified curve had to be interpolated, since the two inherently different measurement techniques did not enable overlapping results. Thermal expansion data of DP6 for the upper part of the cryogenic temperature region [1] only extended down to about -40°C , due to the onset of crystallization for the achievable cooling rate. That necessitated data interpolation, which reduced the quality of the

previously published unified curves [42]. No onset of crystallization was observed for DP6 combined with SIMs in the upper part of the cryogenic temperature range [2], for the same thermal conditions previously applied in the absence of SIMs [1]. Due to this additional ice suppressing ability, data from [2] was combined with data from the current study to form a unified thermal strain curve without the need for any interpolated region. It should be noted that due to the inherent uncertainties associated with fitting and re-fitting, if possible, it is probably better to use the individual fits from either the upper or lower cryogenic temperature regions instead of the unified fit for thermal strain calculations.

Figure 3.7: Unified thermal-expansion curves including data from the upper [2] and lower [current study] parts of the cryogenic temperature range, for DP6 combined with (a) 12% PEG400, (b) 6% 1,3-CHD, and (c) 6% 2,3-BD. Symbols represent data points calculated from the polynomial approximation for each subset (Table 3.1), solid lines represent polynomial approximations of the unified thermal strain, and dashed lines represent the $\pm 2\sigma$ range [4].



3.6 Summary

Thermal expansion of goat arteries permeated with DP6, combined with selected SIMs, was measured in the lower part of the cryogenic temperature range. Results obtained in the current study were combined with recently obtained data from the upper part of the cryogenic temperature range, in order to formulate unified thermal expansion curves. This database is essential for computation of the formation of thermo-mechanical stress in vitrifying CPAs. The application of SIMs enabled obtaining thermal expansion data in the temperature range of -160°C to 0°C , which was not achievable in the same cooling rates in previous studies in the absence of SIMs.

While thermal expansion is the driving mechanism of thermo-mechanical stress, which may shed light on the likelihood of compromising the structural integrity of the material, additional physical properties must be measured in order to fully characterize the special cocktails combining SIMs. Given the demonstrated low cooling rates with no significant crystallization effect (discussed in greater detail in [2]), the application of SIMs appears very promising for the development of new cryopreservation techniques.

Chapter 4: Stress-Strain Measurements in Vitrified Arteries Permeated With Synthetic Ice Modulators

This chapter expands upon a recently published study in [5]. This study investigated the stress strain behavior of vitrified arteries permeated with DP6+SIM cocktails. In particular, the Young's modulus, and failure stress were measured and can be used in future finite element analyses. A previous study by Jimenez [38] investigating 7.05 M DMSO and VS55 found Young's modulus for larger vitrified blood vessels to be in the range of 0.823-1.039 MPa, the data from this study suggested a broader range of 0.922-2.955 MPa.

4.1 Experimental Apparatus

The experimental apparatus used in the current study has been presented previously by Jimenez-Rios and Rabin [38]. This apparatus is described here in brief for the completeness of presentation, while emphasizing a new modification to the system. The experimental apparatus is designed to achieve two main goals: (i) to cool the specimen down to a selected testing temperature at a high enough cooling rate to promote vitrification, and (ii) to subsequently perform tensile testing on the vitrified specimen at a constant temperature. The key elements of the cooling system are illustrated in Fig. 4.1, where the illustrated loading rods are connected to a computer-controlled mechanical testing device (eXpert 1KN-12-M, ADMET,

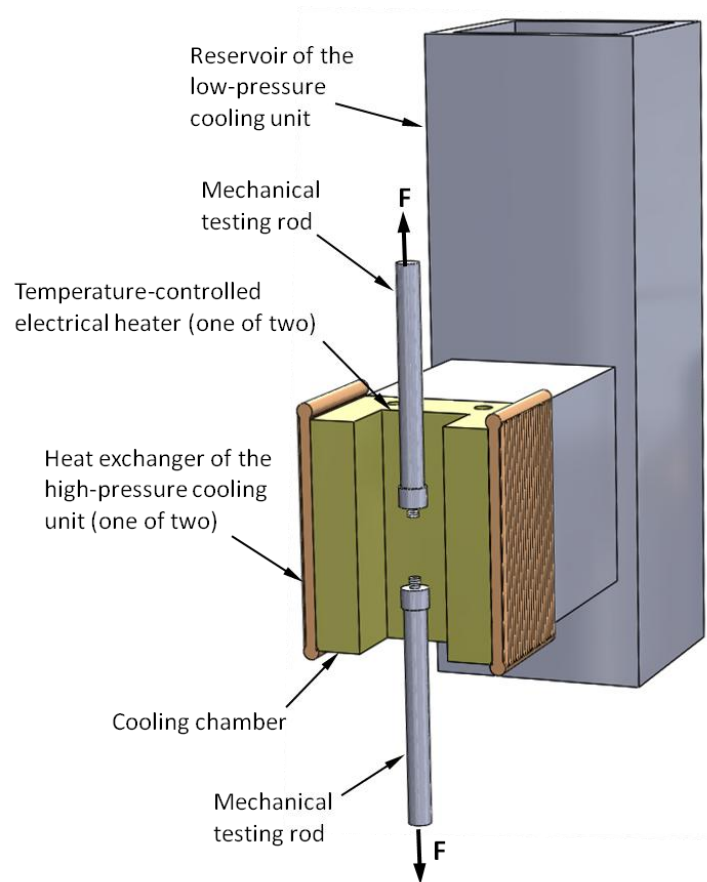


Figure 4.1: Schematic illustration of the key elements of the cooling mechanism for mechanical testing. During experimentation, the artery is attached to the mechanical testing rods (see Fig.4. 2), the cooling chamber is closed with a brass cover, and the system is covered with thermal insulation from all sides [5].

Norwood, MA). In general, the cooling system comprises two units: (i) a couple of heat exchangers powered by compressed liquid nitrogen, to achieve rapid cooling at the beginning of the cooling protocol, and (ii) a reservoir of atmospheric-pressure liquid nitrogen, to cool the specimen during mechanical testing. Thermal control is achieved by means of cartridge heaters embedded in the cooling chamber wall and powered by a cryogenic controller. Automatically logged data during experimentation

includes the mechanical testing parameters (load and elongation histories) and thermal histories by a set of T-type thermocouples, with specific locations described below. Further design considerations and specifications are listed in [38]. Mechanical testing of small-diameter blood vessels has been presented as a new challenge in the current study for two reasons: (i) the diameter of the blood vessels is smaller than the testing-rod diameter, and (ii) heat conduction from the blood vessel to the testing rod (steel) created non-uniform thermal conditions along the specimen.

To overcome this challenge, mechanical-rod thermal-isolators have been designed, as illustrated in Fig. 4.2. Figure 4.3 displays a specimen connected to the thermal insulators, placed in the cooling chamber, and ready for experimentation. Also displayed in Fig. 4.3 is the thick thermal insulation placed around the cooling chamber. Before experimentation, a chamber cover and a thick layer of thermal insulation are also placed between the specimen and the surroundings.

The rod insulator is made in the shape of a Delrin cylinder, having an inner diameter of 4 mm, an outer diameter of 6 mm, and an overall length of 15 mm. The insulator is connected with

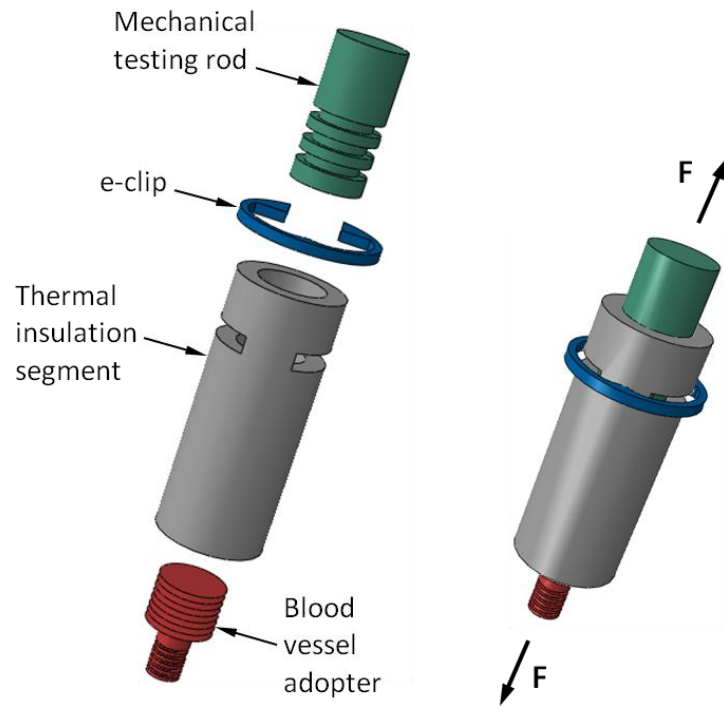


Figure 4.2: Schematic illustration of the mechanical-rod thermal insulators, which were designed to accommodate smaller diameter arteries [5].

an e-clip to the mechanical testing rod, while a threaded adapter is hosted at the other end, to accommodate smaller-diameter blood vessels. This design has reduced temperature non-uniformity along the specimen from 12°C to 4°C (as measured by thermocouples), by reducing the conductive heating effect of the specimen by the mechanical-testing rods.

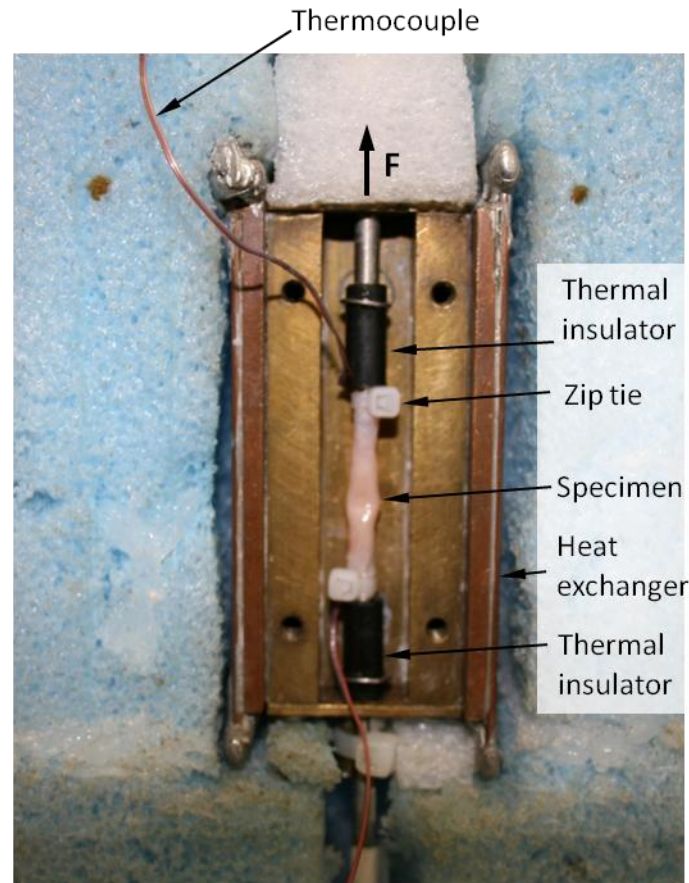


Figure 4.3: An artery sample placed in the cooling chamber and ready for testing, where the cover of the cooling chamber has to be installed and insulated before experimentation. Also shown are thermocouples connected to both ends of the sample, where an additional thermocouple at the center of the sample is yet to be placed [5].

4.2 Materials

All tissue samples used in this experiment were donated by a local slaughterhouse. In order to maintain tissue quality, blood vessel specimens were harvested by members of the research team shortly after the animal was slaughtered. No animals were sacrificed specifically for the purpose of the current study. A main carotid artery was harvested from goats to create samples for testing in a (inner) diameter range from 2.5 to 4.5 mm, a length range from 19 to 35 mm, all with a wall thickness of about 1 mm (wall thickness measurement technique is discussed below). Samples were immersed in SPS-1 organ preservation solution (Organ Recovery Systems, Inc. Itasca, IL) immediately after harvesting and stored at 4°C for a period between one and five days. This range of wait times was necessary due to availability of specimens and based on this study and others [1,2,4,42], appeared to have no effect on experimental results. SPS-1 organ preservation solution is based on the University of Wisconsin solution [60] and is designed to prevent osmotic damage during short term refrigerated storage. Following the procedure outlined in [2], each specimen was immersed in the DP6+SIM or 7.05M DMSO solution before testing. Each sample is placed within a vial containing 3 ml of full concentration CPA. The artery is allowed to drain and the CPA is forced through the artery using a syringe (to insure proper mixing) every twenty minutes. After one hour, the artery is placed into a new 3 ml of full concentration CPA and the process is repeated for another hour.

DP6 is a cocktail of 234.4 g/L DMSO (3M), 228.3 g/L propylene glycol (3M), and 2.4 g/L HEPES in EuroCollins solution. While other CPAs have been found to be a much better at promoting vitrification [1,49], DP6 appears to be more promising due to its reduced overall CPA concentration, and therefore its toxicity. The drawback of reduced CPA concentration is the high cooling rate typically required for vitrification of DP6. Hence, this proposal focuses on DP6 combined with SIMs, in an effort to improve its tendency to promote vitrification.

There are many possible SIMs that could be tested, the particular ones chosen for this report were based on the experience of the current research team [2,7,20]. The following cocktails have been tested: DP6 + 12% PEG400 (n = 6), DP6 + 6% 1,3-CHD (n = 5), and DP6 + 6% 2,3-BD (n = 10) as well as 7.05M DMSO (n=9) as a reference solution, where n is the number of specimens tested. All SIMs: PEG400, 1,3-cyclohexanediol (98% mixture of cis and trans isomers), and 2,3-butanediol (2R,3R isomer), were obtained from Sigma-Aldrich (St. Louis, MO); DP6 was obtained from Cell and Tissue Systems, inc. (Charleston, SC).

4.3 Methods

Specimen Setup: After CPA permeation is completed, the specimen is removed from the solution and held vertically to allow any CPA within the artery to drain. Next, it is placed between the two mechanical-rod thermal isolators (Fig. 4.2) and fastened with cable ties (3.94 inch miniature indoor cable tie) as displayed in Fig. 4.3. The length of the artery between the cable ties is measured with a caliper and T-type thermocouples are placed at the top, middle, and bottom of the artery before the cooling chamber is closed with a brass cover plate.

Experimental protocol: Before the onset of experimentation, the mechanical-testing system is set to zero load control and the temperature controller is set to 20°C. Next, the low-pressure cooling unit is filled with liquid nitrogen, while the temperature controller maintains a cooling-chamber temperature of 20°C, which facilitates precooling for the entire system. The thermal protocol starts by turning the controller off, while simultaneously activating the high-pressure cooling unit, with typical results displayed in Fig. 4.4. In practice, both low-pressure and high-pressure units are working in tandem in this stage, resulting in a high cooling rate sufficient to promote vitrification of the tested samples. Since the critical cooling rate to suppress crystallization needs to be exceeded throughout the domain, and since crystallization is most likely to occur between -30°C and -90°C, the cooling rate was measured for the slowest responding part of the blood vessel between those temperatures. The measured cooling rate between -30°C and -90°C is above 20°C/min for all experiments, where the critical cooling rate for 7.05M DMSO is less than 1.4°C/min and for DP6 without SIMs is 40°C/min, which is why experiments from [38] excluded this cocktail. However, when DP6 is mixed with SIMs, the critical cooling rate is lower than 5°C/min as shown in [2] which facilitates vitrification within the experimental conditions of the current system.

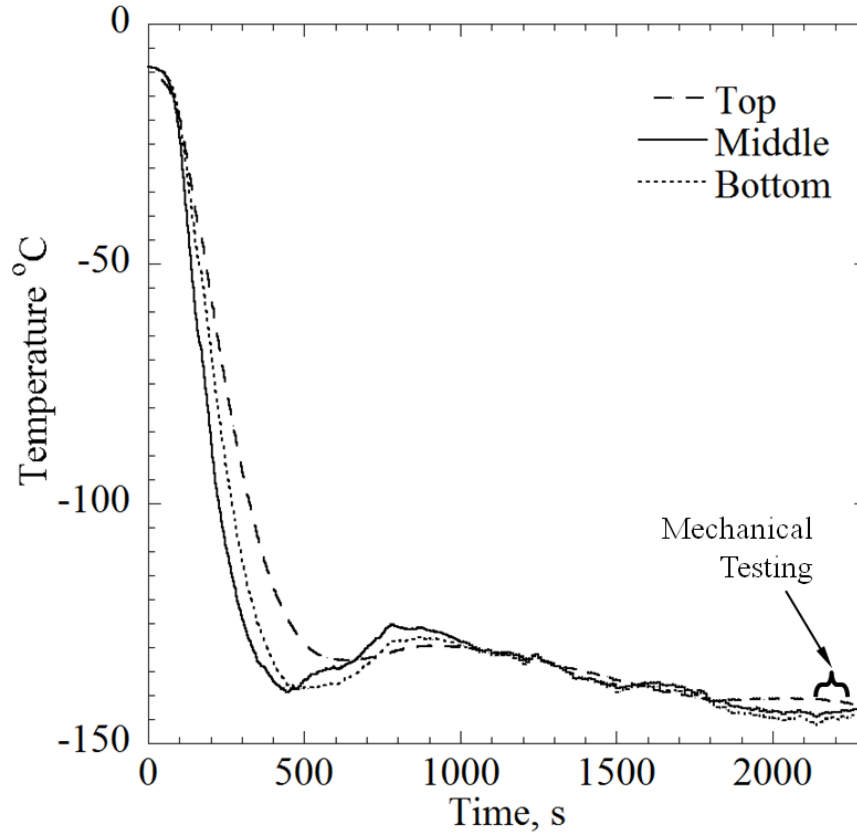


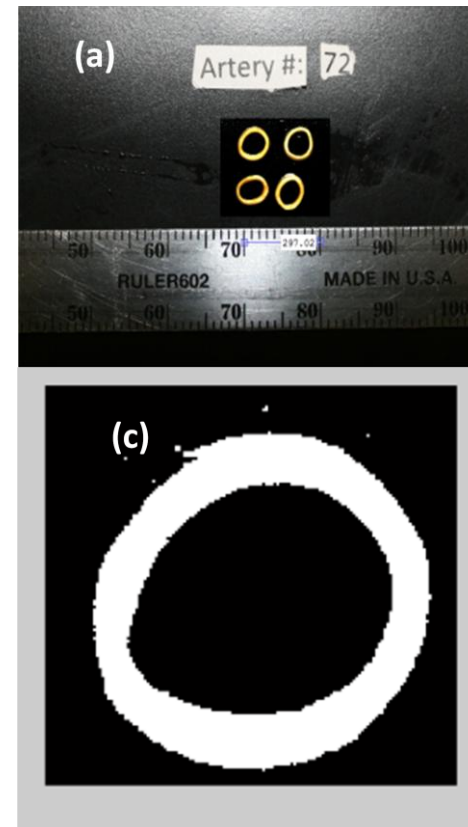
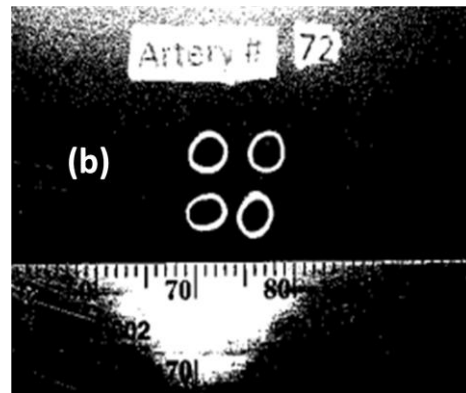
Figure 4.4: A typical thermal history for tensile testing experimentations [5].

Once the specimen approaches the pre-selected testing temperature, the high-pressure cooling unit is deactivated and the temperature controller is reactivated to maintain the specimen at a mechanical-testing temperature. The mechanical-testing temperature range in the current study is between -145°C and -155°C , where the glass transition temperature for DP6 and 7.05M DMSO is -119°C and -123°C , respectively. Next, the cooling chamber is controlled to maintain the mechanical-testing temperature for an intermediate period of time, to allow the specimen and its holders to approach thermal equilibration. This intermediate time period is roughly between 400 s and 2150 s in the representative experiment displayed in Fig. 4.4. The slow-rate, low-magnitude rewarming between 400 s and 800 s is related to a higher order effect resulting from switching between two different cooling mechanisms, thermal inertia of their components, and the change in control parameters. Nevertheless, the temperature during that time period does not exceed the glass transition temperature, and the material can be considered solid over such an extremely short period of time in terms of glassy materials. Finally, the control of the mechanical-testing system is switched from zero-load control to displacement-rate control,

subject to a constant rate of $2.54 \mu\text{m/s}$ until failure, which usually occurs within 80 s.

Cross-section measurements: Once the system has reached room temperature after completing a mechanical-testing experiment, the artery is removed from the cooling chamber and sectioned into four thin rings, approximately 1 to 2 mm thick. These rings are selected away from the top or bottom of the specimen (i.e., the location of the cable ties), and also away from the specimen failure site. Next, the rings are placed on a black background, next to a ruler, and two pictures are taken as displayed in Fig. 4.5. Using the image processing tool *imtool* of Matlab and the ruler (Fig. 4.5a), the number of pixels per unit area is determined. The images are then converted to black and white (Fig. 4.5b) and cropped for each artery (Fig. 4.5c). Next, the cross-sectional area for each processed artery image is calculated via pixel counting. Finally, the process is repeated for the second picture of the same rings, and the characteristic area for further analysis is taken as the average of all the cross sections, from a total of eight images.

Figure 4.5: Images used to calculate the cross sectional area of the artery specimens, including: (a) a stills image of four representative segments and a ruler, to determine area per pixel; (b) a black and white processed image; and (c) an isolated segment used for pixel counting [5].



4.4 Results and Discussion

Three representative stress-strain experimental cases are displayed in Fig. 4.6. Case 1 resembles linear-elastic behavior, which exhibits a sudden stress drop at the point of fracture. All of the specimens permeated with 7.05M DMSO, DP6+1,3-CHD, and DP6+2,3-BD exhibited the same behavior. While most of the specimens permeated with DP6+PEG400 also exhibited the same behavior, selected exceptions are also illustrated in Fig. 4.6, where the response in Case 2 resembles a strain-hardening behavior and the response in Case 3 may be related to plastic deformations. To remove any doubt, it is emphasized that all three specimens were

subject to the same CPA loading protocol, thermal history, and mechanical loading procedure. While the authors cannot currently offer definitive explanations to those exceptional responses, they may be related to aspects of mass-transport during the permeation phase, or to localized crystallization in the tissue, which may be more relevant to DP6+PEG400. Note that early characterizations of the above CPA cocktails were done on small specimens (a differential scanning calorimeter sample size) and in the absence of biological materials, while the current line of investigation focuses for the first time on bulky specimens.

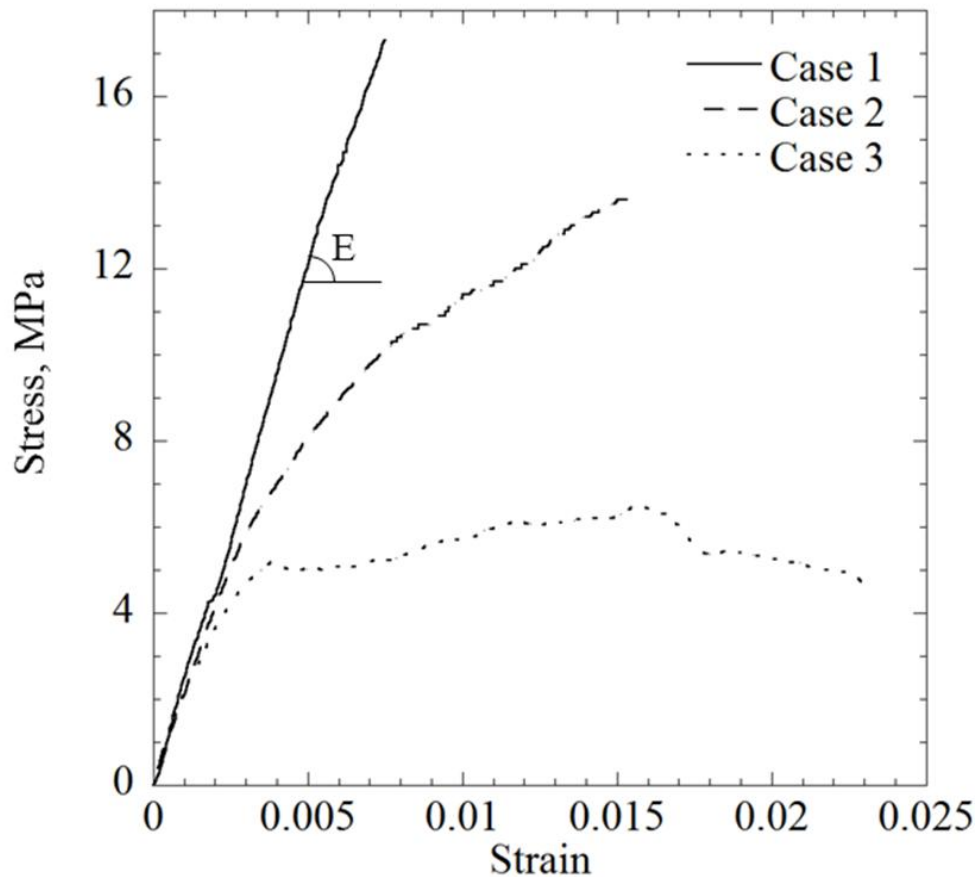


Figure 4.6: Three typical stress-strain curves obtained in the current study: (Case 1) representing the linear-elastic behavior found for specimens permeated with all solutions except for the cocktail DP6+PEG400; (Case 2) a possibly hardening specimen, permeated with DP6+PEG400; and (Case 3) a specimen permeated with DP6+PEG400, possibly exhibiting viscous flow or plastic deformations [5].

In order to study the behavior of the material under repeated loading cycles, several specimens were exposed to such a protocol before failure, where Figs. 4.7(a) and 4.7(b) display the loading and unloading portions of a representative protocol, respectively. In general, the same linear-elastic behavior was maintained throughout the three consecutive loading cycles displayed in Fig. 4.7(a). A closer inspection of the stress-strain curves reveals three step-like changes in strain, labeled A for the first loading cycle, and labeled B and C for the second loading cycle. In the following respective loading cycles, the stress-strain curves coincided at stress levels higher than the respective points—Loads 1 and 2 above point A, and Loads 2 and 3 above point C. Furthermore, these localized incidents did not change the slope of the stress-strain curve (i.e., the Young's modulus), suggesting that the bulk behavior of the specimen has been preserved. It is plausible that the physical event causing such a step-like change in strain is the formation of a

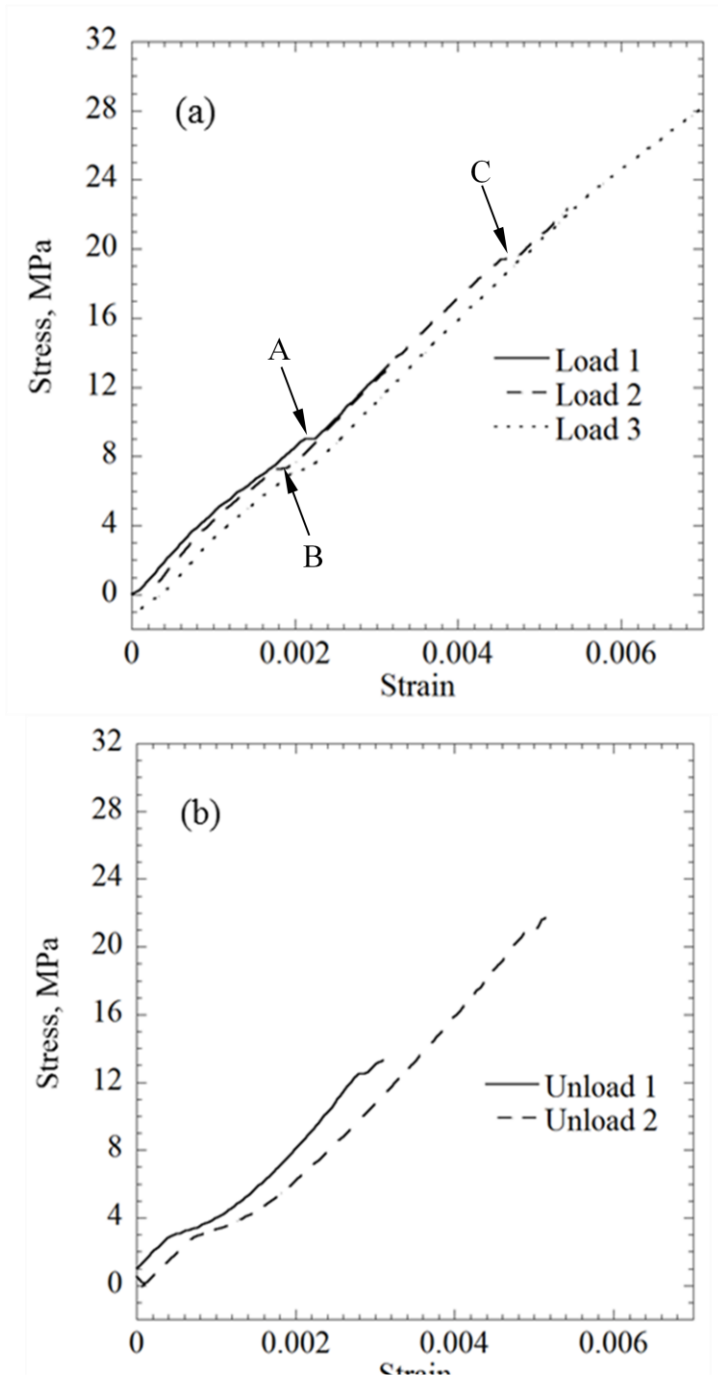


Figure 4.7: Results of repeated loading-unloading cycles in of a blood vessel specimen permeated with DP6 + 12% PEG400: (a) the loading portions of the protocol, and (b) the unloading portions of the protocol; labels A, B, and C point to step-like changes of strain, possibly associated with the formation of microfractures [5].

microfracture, where the area of the fracture is much smaller than the cross sectional area of the

specimen. A similar behavior has been observed under compression in frozen tissues in the absence of cryoprotective agents, where the presence of fractures has been verified using routine histology techniques [61,62]. Figure 4.7(b) displays deviation from the classical linear-elastic behavior during unloading, but the same unloading pattern is preserved between consecutive cycles. It can be concluded from Figs. 4.7(a) and 4.7(b) that no gross damage has occurred prior to the dramatic macrofracture that defined the end of the specific experiment.

In all experiments, the macro-fracture at the end of load testing appeared with clear edges, at the transverse direction to the artery axis. This observation can be explained by one or more of the following reasons: (i) A brittle material under tension tends to fracture along the plane of maximum tensile stress, which is the transverse cross section under uniaxial loading. (ii) Structural failure may follow cell boundaries, which have a circumferential preference in a blood vessel, allowing it to constrict and expand as needed [31].

In a previous study, Jimenez and Rabin measured Young's Modulus of arteries permeated with 7.05M DMSO and VS55, as well as frozen arteries in the absence of CPAs [38]. For arteries permeated with 7.05M DMSO, Jimenez and Rabin measured the Young's Modulus in the range of 823 and 1039 MPa, while results of the current study suggest the Young's Modulus to be in the range of 922 and 2955 MPa. While the lower range values are quite close in both studies, the upper range value in the current study is threefold higher than that in the previous study. The differences between the two studies is the number of specimens ($n=4$ in [38] as opposed to $n=9$ in the current study), and the diameter of the blood vessels is 1 to 2 mm smaller in the current study. The smaller diameter indicates younger animals, but there is no good documentation to the animal ages for those donated specimens. Closer investigation of the differences reveals that the stress-strain behavior reported in [38] more resembles Case 2 than Case 1 in Fig. 4.6, which was found atypical to 7.05M DMSO in the current study. Perhaps this difference is also associated with the lower temperature uniformity in the absence of thermal insulators (Fig. 4.2) in [38]. Interestingly, despite all of the differences listed above, the average fracture stresses as measured in the current study are similar to those measured by Jimenez and Rabin [38]. For the current study, the range of fracture stress is between 6.65 and 19.7 MPa with an average of 13.31 ± 3.74 MPa, which is wider than the range measured in [38], which was between 10.46 and 15.74 MPa, with an average of 12.96 ± 2.03 MPa. This range is particularly wide due to a few outliers, when comparing average fracture stresses between the two studies, the difference is only about 15%.

Table 4.1 provides a summary of all of experimental results. The arteries permeated with DP6 + 6% 2,3-BD exhibited the highest average Young's modulus. However, the variance within each group is high compared with the average difference between the various groups, and no statistical conclusions could be drawn based on a Student's T-test. The current study extends the available knowledge on mechanical properties of vitrified blood vessels at very low temperature [38,39], where no other comparable data has been published elsewhere to the best of the authors' knowledge. By contrast, numerous other studies have measured mechanical properties of blood vessels at room temperature temperatures [63,64]—the only available group of reference. It is difficult to compare those studies, where the blood vessels behaves hyper-elastically, with the current study, but it is interesting to note that the variation in measured mechanical properties in those studies is comparable with the variation in Young's modulus measurements in the current study. It has been suggested previously [38] that the mechanical properties of the vitrified CPA may dominate the behavior of the complex system of CPA-permeated tissue. By contrast, the wide variance of Young's modulus measured in this study, as well as the variance in mechanical properties measured in [63,64], suggest that the tissue structure may actually play a noticeable role in the mechanical response of the CPA-tissue system.

Table 4.1: Summary of experimental data

	Sample #	L, mm	A, mm ²	T, °C	$\dot{\epsilon} \times 10^4, s^{-1}$	$\Delta\epsilon \times 10^3$	E, MPa	R ²	Failure Stress, MPa
PEG400	1	35.00	8.84	-149.3	0.73	0.07	2279	0.999	6.99
	2	31.66	7.54	-145.0	0.80	3.60	2475	0.999	11.21
	3	26.48	8.04	-139.8	0.96	1.91	2006	0.999	9.67
	4	26.00	7.04	-143.0	0.98	2.34	2479	1.000	12.58
	5	30.42	8.84	-139.8	0.84	2.41	2001	0.999	12.44
	6	23.26	8.27	-143.9	1.09	6.21	2426	0.999	15.91
	Average	28.80	8.10	-143.46	0.90	2.07	2248 ± 224*	0.999	10.58 ± 3.01*
7.05 M DMSO	1	28.00	9.40	-150.0	0.91	6.35	922	0.999	7.38
	2	25.70	10.33	-147.5	0.99	5.58	950	0.999	9.80
	3	31.34	10.72	-153.9	0.81	6.88	1011	0.999	12.22
	4	25.93	8.98	-142.9	0.98	10.30	1495	1.000	15.68
	5	31.21	6.78	-167.7	0.81	1.83	2955	0.999	14.81
	6	21.68	9.44	-146.2	1.17	7.88	1839	0.999	13.89
	7	30.48	11.30	-148.6	0.83	4.99	2240	0.999	N/A
	8	24.67	7.26	-163.1	1.03	4.61	2700	0.999	18.01
	9	22.71	12.50	-138.2	1.12	8.15	1631	0.999	12.44
	Average	28.44	9.24	-152.39	0.90	6.19	2143 ± 754*	0.999	11.98 ± 3.36*
1,3-CHD	1	27.39	10.49	-151.0	0.93	2.32	1480	1.000	9.59
	2	22.46	8.03	-142.8	1.11	7.03	2080	0.999	17.96
	3	24.48	8.11	-150.0	1.04	2.69	2310	1.000	10.07
	4	27.19	8.31	-144.3	0.93	3.06	1777	0.999	6.65
	5	25.63	8.66	-145.5	0.99	2.46	2448	0.999	15.92
	Average	25.43	8.72	-146.7	1.00	3.51	2019 ± 394*	0.999	12.04 ± 4.72*
2,3BD	1	21.31	7.21	-148.3	1.19	2.14	2940	0.999	12.83
	2	28.31	10.71	-143.3	0.90	1.77	2868	0.999	10.05
	3	29.07	8.80	-146.0	0.87	1.66	3012	1.000	19.72
	4	22.68	6.93	-153.0	1.12	3.95	2811	0.999	18.68
	5	19.35	8.15	-144.2	1.31	5.10	2062	0.999	15.64
	6	24.24	9.79	-147.0	1.04	5.27	1688	0.999	14.65
	7	24.26	8.67	-141.0	1.05	5.22	2298	0.999	19.32
	8	19.07	8.62	-151.7	1.33	1.92	1675	0.999	12.19
	9	24.01	8.52	-149.8	1.06	7.38	2416	0.999	16.46
	Average	23.59	8.60	-147.14	1.10	3.82	2419 ± 525*	0.999	15.50 ± 3.39*
Frozen	1	23.29	9.79	-146.1	1.09	4.84	1226	0.996	5.25

*Standard deviation

4.5 Summary and Conclusions

This study aims at measuring the Young's modulus in vitrified blood vessels below the glass transition temperature, in conditions relevant to cryogenic storage. This study expands on previously developed data [39], with the unique contribution of testing CPAs mixed with SIMs, a group of compounds of increasing interest in the cryobiology community. The effect of SIMs on the mechanical behavior of the vitrified biomaterial is largely unknown. The experimental apparatus used in the current study has been developed previously [38], and combines a new modification in the form of thermal insulator to: (i) improve temperature uniformity within the specimen, and (ii) facilitate mechanical testing at lower temperatures.

Results of this study indicate a linear-elastic behavior of the vitrified specimens below glass transition. This behavior is regained under repeated loading/unloading cycles. Small step-like strain changes have been observed during the loading without affecting the bulk behavior of the specimen, suggesting microfracture occurrences. This observation agrees with previous observation on microfracture formation under compression in the absence of CPA and SIMs. While small deviation from the classical linear-elastic model during unloading has been observed, this behavior is repeatable and indicates no permanent damage to the specimen due to loading before the dramatic specimen failure defining the end of experimentation.

Results of this study indicate a Young's modulus in the range of 0.92 to 3.01 GPa, with no clear indication that the different SIMs affect the Young's modulus value differently. It is suggested that this range of values is attributed to variations between specimens of the same species and not to the SIMs. Results of this study suggest that past computations of mechanical stress during vitrification may have used values from the lower end of the measured range, most frequently 1 GPa [49–51,65]. This is important for future analysis mechanical stress for cryopreservation by vitrification.

Chapter 5: Effects of Thermal History on Mechanical Stress in Cryopreservation via Vitrification

This chapter expands upon a recently published study in [7]. This study investigated how the cooling and rewarming histories affect the mechanical stress of a vitrifying domain. Two separate cases were studied, one where the surface of the CPA domain was assumed to be traction free (this models the CPA within some kind of highly pliable container, such as a bag) and the other where the CPA was held within a rigid container. A realistic thermal protocol was proposed and the various sections of this protocol were varied in order to investigate the effects of each parameter on the mechanical stress history. This is the first study which quantitatively investigated the effects of annealing on mechanical stress in cryopreservation.

5.1 Background information on mechanical stress in cryopreservation via vitrification

Several studies have investigated the formation of fractures in cryopreserved materials and their dependency on the employed thermal protocols [30,31,33,34,66]. Fractures have been observed in mouse blastocysts [30], blood vessels [31,66], Mexican fruit flies [33], as well as CPA in the absence of biological specimens [34,66]. Pegg and co-workers [31] showed that fractures in cryopreserved arteries generally formed during the initial stages of rewarming, and that fractures could be prevented by lowering the rewarming rate while below -100°C . Kasai and co-workers [30] and Rajamohan and Leopold [33] further suggested that the tendency to fracture can be reduced by both lowering the initial rewarming rate and the final cooling rate. These studies suggest that an optimal thermal protocol should involve two-stage cooling, with rapid cooling to prevent crystallization followed by slower cooling to avoid fracturing, and consistently two-stage rewarming, with slow warming followed by rapid warming. Cryogenic protocols of similar nature are common practice in cryopreservation [20,21], where the specific rates are often explored by trial and error.

Rabin and Steif [67,68] presented a mathematical model for calculating the developing stresses in an inward freezing problem of classical cryopreservation. This model assumes that the unfrozen region, being a low-viscosity material, can only sustain hydrostatic pressures but cannot support deviatoric stresses. The main contribution in that study is that the deviatoric stress must be zero at the freezing front but that the deviatoric stress at the melting front may be non-zero. This outcome of modeling provides an explanation for the counterintuitive experimental

observation that fractures often develop at the beginning of the rewarming phase, when the stress reaches its peak value.

The domain does not crystallize during cryopreservation via vitrification but, instead, over a limited temperature range the viscosity increases dramatically by 12 orders of magnitude, from a liquid-like to a solid-like material. Instead of having two distinct regions as in classical cryopreservation, possibly modeled as a low viscous fluid and a linear-elastic solid, in vitrification the material may be modeled from an engineering mechanics perspective as having three regions, characterized as a low viscous fluid, a transition region, and a highly viscous material—practically a solid. Additionally, since there is no crystallization, the large volume expansion associated with water changing to ice does not occur during vitrification. Nevertheless, the modeling approach in [67,68] remains applicable and the analysis of vitrification protocols calls for further investigation—the subject matter of the current study. Beyond temperature gradients within the domain, thermal stress may also develop in response to differential thermal strain between the CPA and its container [50,52]. This effect is further investigated in the current study in the context of vitrification.

As part of an ongoing effort to investigate thermo-mechanical effects in cryopreservation [1–3,37–39,42,49,50,52,66], the current study aims at investigating the potential contribution of including a temperature-hold step in cryopreservation protocols, in order to facilitate annealing and thereby reducing the risk to structural damage. The current study focuses on large-size specimens, where thermo-mechanical stress may lead to structural failure. While large-size *per se* may commonly refer to specimens measuring a few millimeters or more in the context of cryobiology, large-size in the analysis of thermo-mechanical stress may have a different, outcome-dependent meaning. In the current study we refer to large-size specimens as specimens that exhibit steep temperature gradients which can give rise to significant stresses, possibly reaching the strength of the material. Hence, the term, large-size, is associated with the temperature non-uniformity within the specimen along the thermal history, which may not be known *a priori*. The vast experimental evidence summarized above support the notion of such a relationship, while the current theoretical study is designed to explore it.

5.2 Modeling

Due to the high viscosity of the CPA within the temperature range relevant to the

development of thermo-mechanical stress, heat transfer in the domain is assumed solely by conduction:

$$\rho C_p \dot{T} = \nabla \cdot (k \nabla T) \quad (5.1)$$

where T is temperature, ρ is density, C_p is specific heat capacity, and a superposed dot represents a time derivative. Note that heat generation due to viscous dissipation is negligible compared with changes in energy due to heat flow. This has important computational implications as the temperature field can be computed first, without consideration of stresses, and then the stresses are computed while taking into account the temperature field.

5.2.1 Material Model

The viscosity of a CPA increases with the decreasing temperature until it acts as solid at very low temperatures, which is modeled as a viscoelastic fluid. Following the simplest approach that captures such behavior, the CPA is modeled as a so-called Maxwell fluid, where the total strain rate is the sum of strain rates due to elastic deformation, viscous flow, and thermal expansion. For uniaxial tension in a lumped-capacity system (uniform temperature distribution) this relation is given by:

$$\dot{\epsilon} = \frac{1}{E} \frac{d\sigma}{dt} + \frac{\sigma}{3\eta} + \beta \frac{dT}{dt} \quad (5.2)$$

where $\dot{\epsilon}$ is the total strain-rate, σ is the stress, E is the Young's Modulus, η is the viscosity, and β is the coefficient of linear thermal expansion. Since the viscosity is temperature-dependent, the viscous portion of the strain rate dominates its elastic portion at high temperatures. Conversely, the elastic portion dominates the viscous portion at low temperatures, while at mid-range temperatures both responses are significant.

A non-uniform temperature distribution will give rise to a general state of stress, not necessarily limited to uniaxial tension or compression. The material model for the creep strain rate given by Eq. (5.2) is generalized following a standard approach in mechanics as follows:

$$\dot{\epsilon}_{creep} = \frac{\mathbf{S}}{2\eta} \quad (5.3)$$

where \mathbf{S} is the deviatoric stress tensor, corresponding to the stress tensor with the hydrostatic pressure removed. The elastic strain rate is related to the stresses by the isotropic elastic relation:

$$\dot{\boldsymbol{\epsilon}}_{elastic} = \frac{1}{E} [(1 + \nu)\dot{\boldsymbol{\sigma}} - \nu \mathbf{I} \cdot tr(\dot{\boldsymbol{\sigma}})] \quad (5.4)$$

where ν is the Poisson ratio, \mathbf{I} is identity tensor, and $tr(\dot{\boldsymbol{\sigma}})$ is the trace of the stress tensor. Finally, the container of the CPA is assumed to behave linear-elastically, with its own elastic properties.

5.2.2 Finite Element Solution

Figure 1 displays a simplified vial, which will be used in this study. This geometry is representative of a wide class of cryopreservation applications, and is simulative of recent experimental investigations using cryomacroscopy [6]. Two general cases are investigated in this study, (A) a reduced problem where wall effects are negligible, and (B) a combined problem of container and CPA.

The coupled thermal-stress problem is solved with the commercial finite element code Abaqus (Dassault Systèmes, Inc.). The heat transfer and displacement problems use identical meshes consisting of 8-noded, axisymmetric, quadrilateral DCAX8 elements for heat transfer and CAX8H for displacement calculations. For Case B, 1451 elements are used to geometrically model the CPA subdomain and 190 elements are used for the container, while 414 elements in total are used for Case A. The reduced number of elements in Case A is associated with the simplified CPA boundary condition (Fig. 5.1)

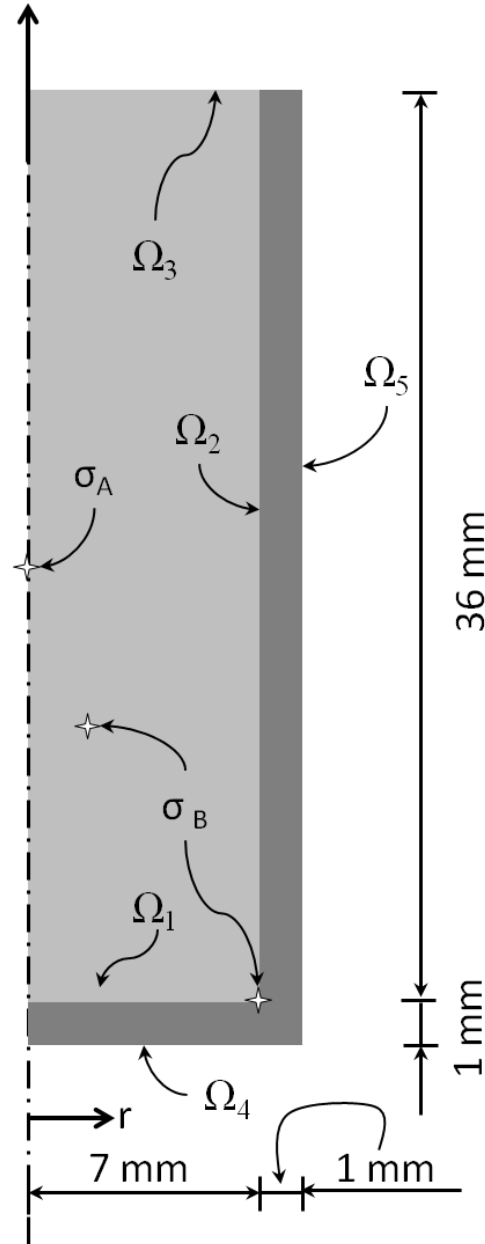


Figure 5.1: Schematic illustration of the axisymmetric model used for FEA in the current study for two key cases: (Case A) CPA in the absence of a container, where identical temperature boundary conditions are imposed on Ω_1 , Ω_2 , and Ω_3 ; and (Case B) CPA contained within a cylindrical vial, where identical temperature boundary conditions are imposed on Ω_4 and Ω_5 , while thermal insulation is assumed on Ω_3 , consistent with [6]. In both cases zero normal stress is assumed on the outer most surfaces. In Case B, continuity in temperature and displacement are assumed on Ω_1 and Ω_2 . Also illustrated for the purpose of discussion the maximum principle-stress points, σ_A and σ_B , for Cases A and B, respectively [7].

5.2.3 Material Properties

The material property values used in the current study are listed in Table 5.1. Due to limited availability of relevant CPA properties and due to its high relevancy to vitrification, the CPA cocktail VS55 is used as a model for material properties. In one case study, properties of the CPA dimethyl sulfoxide (DMSO) and the CPA cocktail DP6 are additionally used. The ingredients of VS55 and DP6 were described previously in section 2.3. Beyond being a classical CPA and a key ingredient in both cocktails, the 7.05M DMSO has been demonstrated as a reference solution for the study of thermo-mechanical stress [37].

With the exception of viscosity, all CPA properties used in the current analysis are temperature independent, which simplifies the analysis. Consistent with recently published studies to explain cryomacroscopy observations [69], the container material properties are assumed similar to polystyrene. Despite all of the work that has been done, some material property data for VS55 is still unavailable. The density of VS55 was assumed to be the same as 8.4M DMSO (which is known) since they have the same solute concentration. Additionally, the Poisson's ratio of VS55 was assumed to be 0.25, which is typical of elastic solids.

Due to the high temperature dependency of the CPA viscosity, changing twelve orders of magnitude in the relevant temperature range for vitrification, special steps were taken to ensure stability and convergence of the FEA analysis in a realistic computer run time. At the beginning of cooling, when the viscosity is extremely low, extremely short time steps would be required in order to ensure stability within the simulation. Conversely, at extremely low temperatures, the viscosity is so high that the material simply acts elastically. In order to simplify the solution, a piecewise functional form was used to approximate the viscosity behavior, as listed in Table 5.1 [43].

While every attempt was made to select the most representative property values for the current study, results of this study are considered somewhat qualitative rather than quantitative for the following reasons: (i) some material properties are not readily available and, therefore, are estimated; (ii) some material properties have been assigned constant values rather than capturing their true temperature-dependent behavior in order to simplify the analysis; (iii) the one term (Maxwell) viscoelastic model that has been chosen for this study may be too simplistic to fully capture the full behavior for a given CPA; and, (iv) the selection of VS55 as a representative CPA cocktail is a choice of practice, where other cocktails may exhibit somewhat

different values. Nevertheless, the physical modeling in the current study is believed by the authors to generate realistic level of stresses, and comparison between the different cases are believed to provide credible guidelines on how to reduce the level of stress in similar protocols. By comparing the effects of the various thermal protocols, it should be possible to determine which protocols are likely to minimize stress (and thus the likelihood to fracture) in comparison with the others.

Table 5.1: Physical properties used in this study

Property	Material	Value	Source
Viscosity	VS55	$\eta = 1.21 \times 10^4 \text{ Pa-s; } -100^\circ\text{C} < T$ $\eta = 4.2783 \times 10^{-23} e^{-0.6091T} \text{ Pa-s; } -140^\circ\text{C} < T < -100^\circ\text{C}$ $\eta = 4.63 \times 10^{14} \text{ Pa-s; } T < -140^\circ\text{C}$	[43]
	7.05M DMSO	$\eta = 1.77 \times 10^4 \text{ Pa-s; } -110^\circ\text{C} < T$ $\eta = 2.8190 \times 10^{-27} e^{-0.6447T}; -147^\circ\text{C} < T < -110^\circ\text{C}$ $\eta = 4.06 \times 10^{14} \text{ Pa-s; } T < -147^\circ\text{C}$	[43]
	DP6	$\eta = 5.11 \times 10^4 \text{ Pa-s; } -100^\circ\text{C} < T$ $\eta = 5.6503 \times 10^{-23} e^{-0.6207T}; -137^\circ\text{C} < T < -100^\circ\text{C}$ $\eta = 4.82 \times 10^{14} \text{ Pa-s; } T < -137^\circ\text{C}$	[43]
Glass Transition Temperature (DSC)	VS55	-123°C	[37]
	7.05M DMSO	-132°C	[70]
	DP6	-119°C	[37]
Density	VS55	1100 kg/m ³	[71]
	Container	1075 kg/m ³	[72]
Thermal Conductivity	VS55	0.3 W/m-°C	[114]
	Container	-0.01274T + 0.02 W/m°C	[73]
Specific Heat	VS55	2400 J/kg-°C	[74]
	Container	03.936T + 1121.1 J/Kg-°C	[72]
Thermal Expansion	VS55	1.1 x 10 ⁻⁴ °C ⁻¹	[1,2,37,42]
	Container	0.7 x 10 ⁻⁴ °C ⁻¹	[115]
Young's Modulus	VS55	800 x 10 ⁶ Pa	[38,39]
	Container	3.45 x 10 ⁹ Pa	[75]
Poisson's Ratio	VS55	0.25	Assumed
	Container	0.35	[75]

5.2.4 Thermal History at the Boundary

The goal of this study is to investigate how the thermal history affects stresses and, thus, the likelihood to fracture, for which a variety of temperature boundary conditions are compared. Consistent with cryopreservation practices [17,99,103], a reference thermal history at the boundary is displayed in Fig. 5.2(a), combining five stages (labeled as R_1 , R_3 , R_4 , R_5 , and R_6). The reference thermal history at the boundary consists of (R_1) fast cooling at a rate of $5^\circ\text{C}/\text{min}$ from room temperature (20°C) down to an intermediate temperature of -100°C , (R_3) slow cooling at a rate of $1^\circ\text{C}/\text{min}$ down to the storage temperature of -196°C (liquid nitrogen boiling), (R_4) hold time of 20 min at the storage temperature, (R_5) slow rewarming at a rate of $7.5^\circ\text{C}/\text{min}$ up to an intermediate temperature of -100°C , and (R_6) fast rewarming at a rate of $100^\circ\text{C}/\text{min}$ back to room temperature. The R_1 and R_6 cooling/rewarming rates were chosen so that the entire specimen would exceed the critical cooling/rewarming rate for VS55, which is estimated to be $2.5^\circ\text{C}/\text{min}$ and $50^\circ\text{C}/\text{min}$ respectively [21,70].

There has been some speculation that an intermediate stage of temperature hold at the vicinity of glass transition would be favorable in reducing stresses, by facilitating annealing or stress relaxation. In order to investigate this proposed practice, an additional thermal history at the boundary is investigated, combining an intermediate temperature hold before cryogenic storage. The latter thermal history is referred to as the modified thermal history, and the additional temperature hold is labeled R_2 , as displayed in Fig. 5.2(a). The modified thermal history extends the cooling rate of R_1 to a lower temperature of -122°C , combined with a hold time of 1200 sec, to potentially facilitate stress relaxation. The remainder of the modified protocol is essentially the same as the reference one. The temperature selection of -122°C is not arbitrary but is related to the glass transition process. Noday et al. [43] have measured viscosity values of 10^{10} and 10^{12} Pa-s at temperatures of -122.4 and -129.9°C , respectively (the temperature at which the viscosity gets to a value of 10^{12} P-s is one common definition of glass transition). DSC studies indicate an intermediate glass transition temperature of -123°C [43].

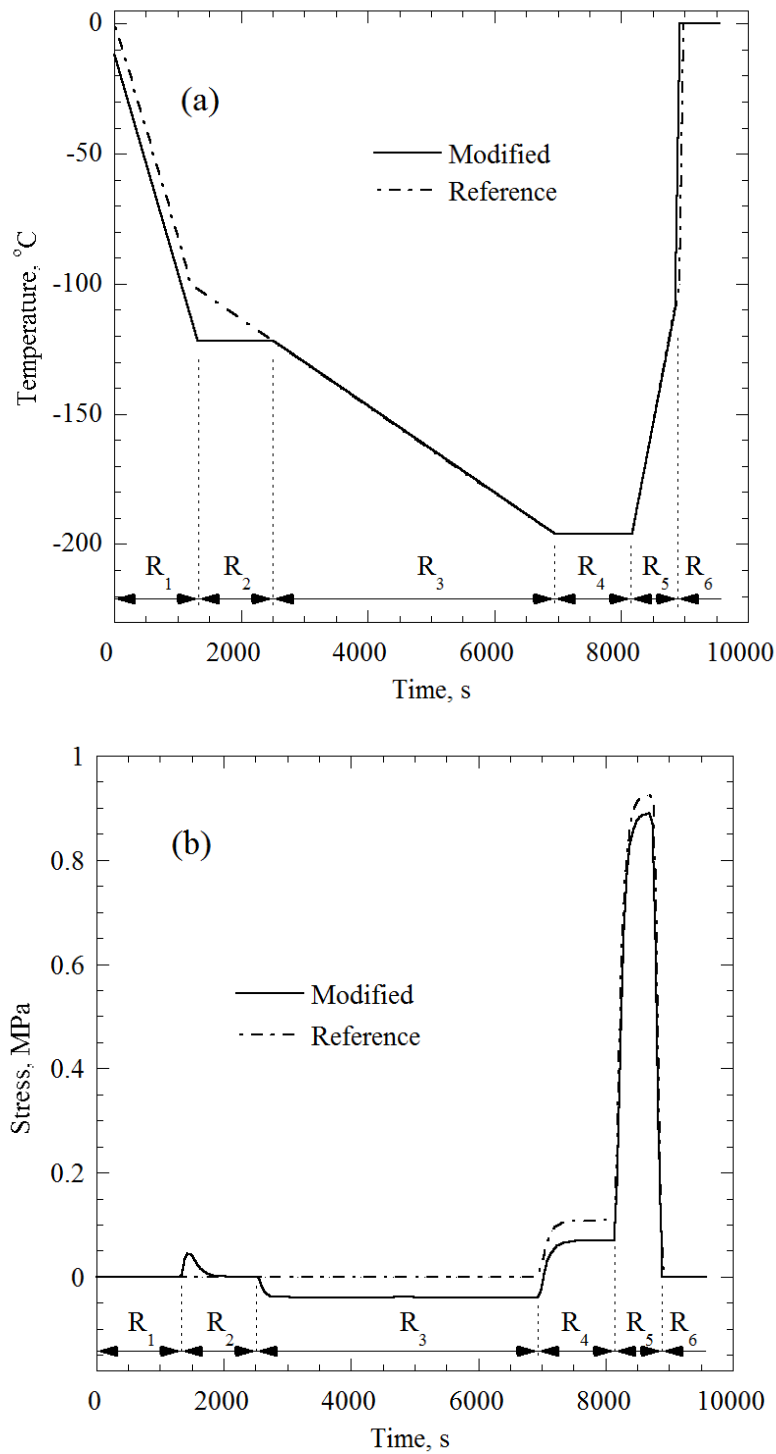


Figure 5.2: The key thermal histories used in the current study and the corresponding principle stress for the case of uncontained CPA (Case A): (a) the thermal history imposed on the external boundary (Fig. 1), where the modified protocol includes an annealing stage; and (b) the corresponding principle stress at the center of the domain, subject to data shifted in time such that both data sets have a common onset of rewarming in stage R5—the stage in which maximum stress is found [7].

In order to investigate the effects of each parameter of the modified case, the different stages are methodically varied from the above nominal values. For the four cooling/rewarming stages (R_1 , R_3 , R_5 , and R_6), four rate variations are further investigated, having slopes of either one fourth, one half, twice, or quadruple the above nominal values. For the annealing stage (R_2), four hold temperature variations are studied, at $+4^\circ\text{C}$, $+2^\circ\text{C}$, -2°C , and -4°C of the nominal value listed above. For the storage stage (R_4), four additional storage temperatures are selected at -140°C , -150°C , -160°C , and -170°C . Recall that the glass transition temperature for VS55 is -123°C and any of the above storage temperatures can be conveniently achieved in the vapor phase storage above liquid nitrogen (common practice in cryopreservation). Finally, the duration of the temperature hold stages (R_2 and R_4) was varied between the different cases to ensure thermal equilibrium at the end of each respective stage. In practice, the material was assumed thermally equilibrated when temperature non-uniformity of less than 0.1°C was achieved at each respective case.

5.3 Results and Discussion

This study is theoretical by nature, encapsulating the underlying principles of thermo-mechanical stress in viscoelastic materials, as they pertain to experimental observations collected in previous studies. The current study does not include in vitro experiments, but is intended to lay out a foundation for future design of in vitro investigations. Given the virtually endless combinations of experimental variables and the cost of experimentations, such a systematic approach to future studies is deemed essential. In a parallel study, polarized light and photoelasticity principles are also explored to augment the design of such future investigations [76]. With this approach in mind, the discussion below starts with thought experiments explaining the key features of stress development in typical cryopreservation cases, and gradually advances to more complex case studies, which may be studied experimentally in a progressive manner.

5.3.1 Thought Experiments

The ideas presented in [67,68] are fundamental to the understanding of stress development during cryopreservation via vitrification, so they will be adapted here to illustrate the effects of a thermal protocol on thermal stress in a simple thought experiment. Consider a very long cylinder

with temperature-independent material properties, initially at a uniform temperature. Starting at room temperature, the boundary is cooled at a constant rate down to a storage temperature of -196°C , held there for some period of time, and then rewarmed at a constant heating rate back to room temperature. During cooling, a temperature gradient will develop, where the outside is colder than the inside. At storage, this gradient will decay towards thermal equilibrium, while during rewarming, the opposite temperature gradient will develop, with the outer surface warmer than the inside. If the material would be an elastic solid throughout the process, then the outside would undergo tension during cooling and correspondingly the inside would undergo compression. With thermal equilibrium, the material would return to a stress-free state at the storage temperature. Finally, from similar arguments, the outside would undergo compression while the inside undergoes tension during rewarming. Through this thought experiment, the stress state of the material is dependent only upon the instantaneous thermal gradient.

Consider another thought experiment where the viscosity of the material transitions smoothly from a low viscous fluid at high temperatures to a highly viscous material at low temperature, with such a high viscosity value that it can be considered solid for all practical applications. Stress relaxation occurs so quickly at high temperatures that, despite the developing temperature gradients during cooling, the material is initially cooled stress free. Further assume that the temperature gradient in the material develops in the same manner during cooling, whether the material behaves linear elastically or viscous. As the material approaches the storage temperature, the vitrified material is stress free, has a thermal gradient built in, but now responds elastically due to the low temperature. So, as the thermal gradient equilibrates, stresses build with tension on the inside and compression on the outside. Thus, at storage temperature, the material has a built in residual stress. This residual stress is equal in magnitude and opposite in direction when compared to the stress that developed in the equivalent purely elastic body during cooling. So, residual stresses left in the body at storage temperature are dependent on the thermal gradient which formed during cooling, hence the current stress state is thermal-history dependent. Finally, as the material rewarms, the inside undergoes additional tension on top of the residual tension and the outside undergoes additional compression. These stresses then disappear as the temperature becomes warm enough to allow for stress relaxation (as the material transitions from elastic solid to viscous fluid). As described in [67,68], this additional tension at the onset of rewarming, coupled with the fact that brittle materials such as glasses tend to fail due

to tensile stress explains theoretically why CPAs are most likely to fracture at the onset of rewarming, as seen empirically in [30,31,33–35].

In practice, many thermal protocols consist of two-stage cooling (fast then slow), storage, and then two-stage rewarming (slow then fast). One can see why this approach may be effective based on the stress history analysis above. Since gradients that form within the liquid phase have no effect on stress, the cooling rate can initially be high; at lower temperatures, as the material begins transitioning towards a more elastically dominated response, lower cooling rates are beneficial because their smaller temperature gradients result in lower stresses at storage. Additionally, the material reacts elastically at the initial stages of rewarming, so slow rewarming is needed in order to reduce stress, but as the material transitions from elastic solid to viscous fluid, faster warming will not lead to higher stresses. The initially high cooling rate and the terminal high rewarming rate are required to suppress crystallization, when the viscosity is low. Hence, high tendency to crystallize and high potential to significant thermal stress mostly reside in complementary parts of the cryopreservation protocol. It is the transition between the different regimes that is critical to the analysis in the current study.

These concepts are qualitatively illustrated in Fig. 5.3, where two infinite cylinders, having the same thermal and mechanical properties are exposed to identical thermal histories. The material that behaves linear elastically displays zero stress each time the temperature equilibrates. The viscoelastic material (vitrified material) displays residual stress at cryogenic storage, increased stress upon rewarming, and relaxation of stress at higher temperatures by means of viscous flow.

Fractures tend to form in brittle materials due to maximum principal stress. The maximum principal (also tensile) stress in the CPA in Case A (no container) always occurs in the axial direction at the geometric center of the specimen. For this reason, all stress history plots for CPA simulations in the current study are taken from that location unless specified otherwise. Finding the location of maximum stress in Case B (with container) is somewhat more complicated as described below.

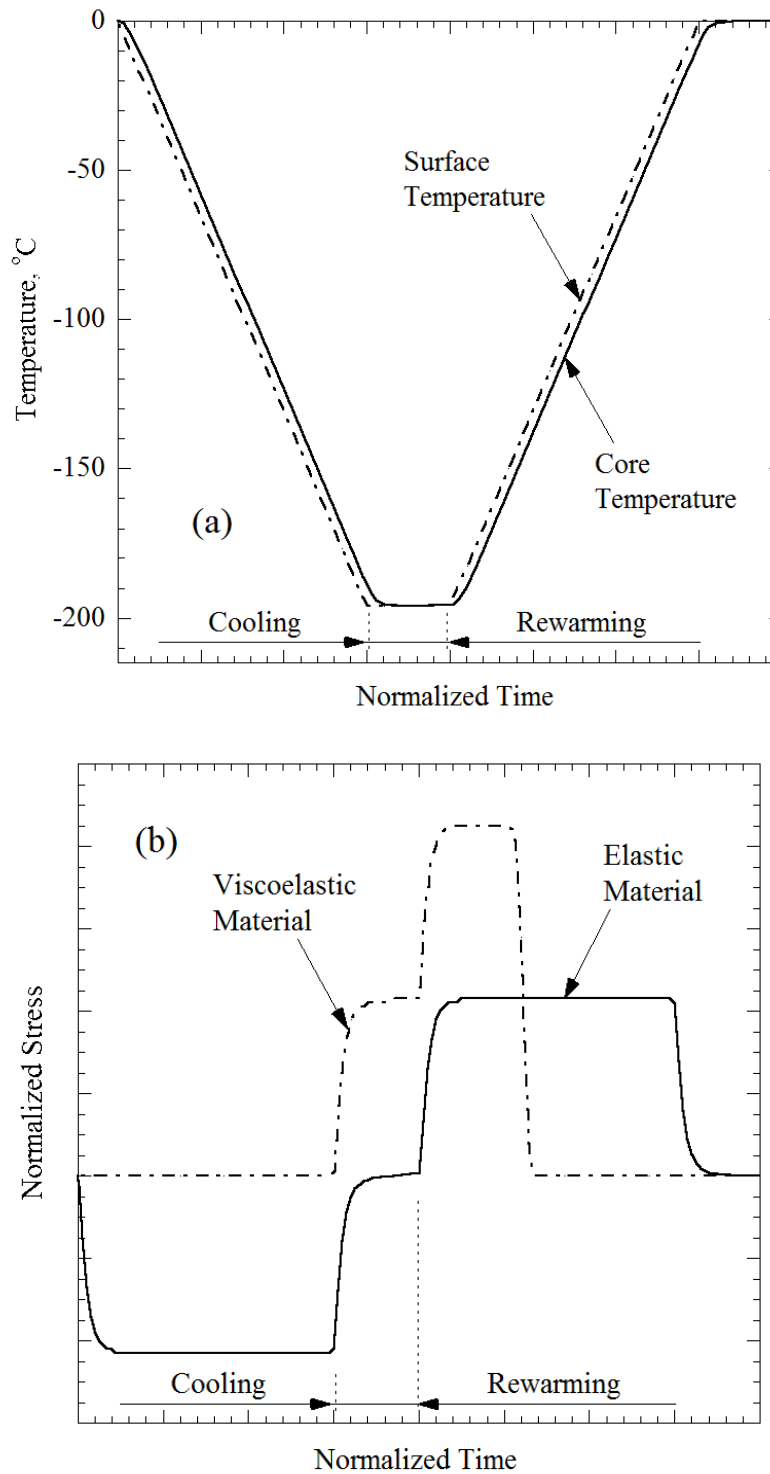


Figure 5.3: Qualitative results of a thought experiment subject to simplified boundary conditions in Case A: (a) the expected thermal history at the center of the domain subject to imposed temperature on the outer surface; and (b) the corresponding principle (also axial) stress at the center of the domain for both an elastic and viscoelastic material models [7].

5.3.2 CPA Simulations – Case A

Figure 5.2(b) displays the axial stress history at the center of the sample for both the reference and modified thermal histories for Case A (no container). The stress due to the reference boundary condition is consistent with the thought experiment described above (see Fig. 5.3). To summarize, there is zero stress state during cooling, residual tensile stress develops during thermal equilibration at storage temperature, additional tensile stress at the onset of rewarming, and stress relaxation as the sample transitions back into a viscous fluid. The maximum stress due to the modified thermal history is somewhat lower and the stress history is more complex: a “blip” in stress during annealing at R_2 , and compression during cooling in R_3 . These effects are explained below. The maximum stress in Fig. 5.2(b) is of the order of 1 MPa, which is similar in magnitude to the stress-to-fracture in prior experimental investigations [65]. Results of other case studies below indicate even higher predicted stresses, which suggest possible fracturing for the corresponding thermal histories.

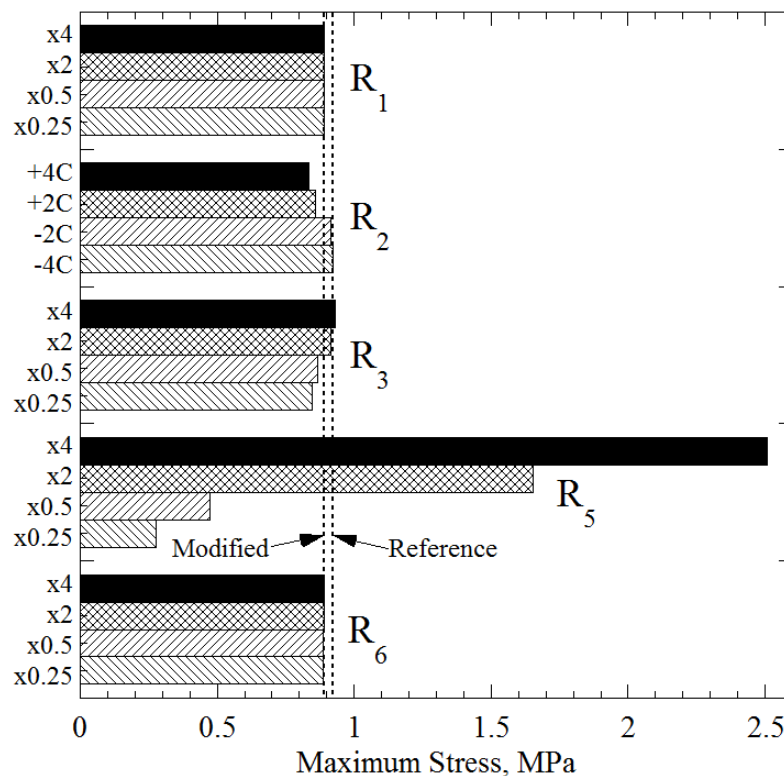


Figure 5.4: Maximum tensile stress for the in general Case A of the modified protocol (stress relaxation stage included) for variable boundary conditions. In each special case, only one parameter is varied at a time, while the maximum stress is always found in R_5 , qualitatively consistent with Fig. 5.2 [7].

Figure 5.4 displays the maximum tensile stress for select boundary conditions and additional numerical detail is summarized in table 5.2 including the cooling/warming rates, and annealing temperatures. Sections R_1 and R_6 occur exclusively at high temperatures, where viscosity is low enough to allow for instantaneous stress relaxation. As a result, the cooling rate in neither section has an appreciable effect on the maximum tensile stress, nor for that matter do they have any appreciable effect on the stress state anywhere in the material. Empirical studies have shown that neither of these sections have an appreciable effect on the likelihood to fracture [30,31,33].

Table 5.2: Summary of thermal-history parameters and the resulting maximum stresses resulting maximum stresses for the cases compared in Fig. 4.

Protocol Section	Description	Label	Value	Max Stress (MPa)
R_1	Initial cooling rate ($^{\circ}\text{C}/\text{min}$)	x0.25	1.25	0.893
		x0.5	2.5	0.893
		Modified	5	0.890
		x2	10	0.893
		x4	20	0.893
R_2	Annealing Temperature ($^{\circ}\text{C}$)	+4	-118	0.924
		+2	-120	0.914
		Modified	-122	0.890
		-2	-124	0.858
		-4	-126	0.835
R_3	Final cooling rate ($^{\circ}\text{C}/\text{min}$)	x0.25	0.25	0.846
		x0.5	0.5	0.868
		Modified	1	0.890
		x2	2	0.915
		x4	4	0.933
R_5	Initial rewarming rate ($^{\circ}\text{C}/\text{min}$)	x0.25	1.875	0.279
		x0.5	3.75	0.473
		Modified	7.5	0.890
		x2	15	1.653
		x4	30	2.508
R_6	Final rewarming rate ($^{\circ}\text{C}/\text{min}$)	x0.25	25	0.888
		x0.5	50	0.888
		Modified	100	0.890
		x2	200	0.892
		x4	400	0.891

The maximum tensile stress is highly dependent on the rewarming rate in section R_5 , as can

be seen in Fig. 5.4. At these low temperatures, the CPA is so viscous, that it acts like an elastic solid. Thus, the stress due to R_5 is directly dependent on the current thermal gradient. Faster rewarming rates lead to higher tensile stresses and slower rates lead to lower stresses. By reducing the rewarming rate in R_5 to 25% of its reference value the additional stress at the onset of rewarming can be reduced by 75%. Multiple studies [30,31,33] have noted that the likelihood to fracture seems to be highly dependent on the rate of the initial rewarming—this effect is borne out by the current model.

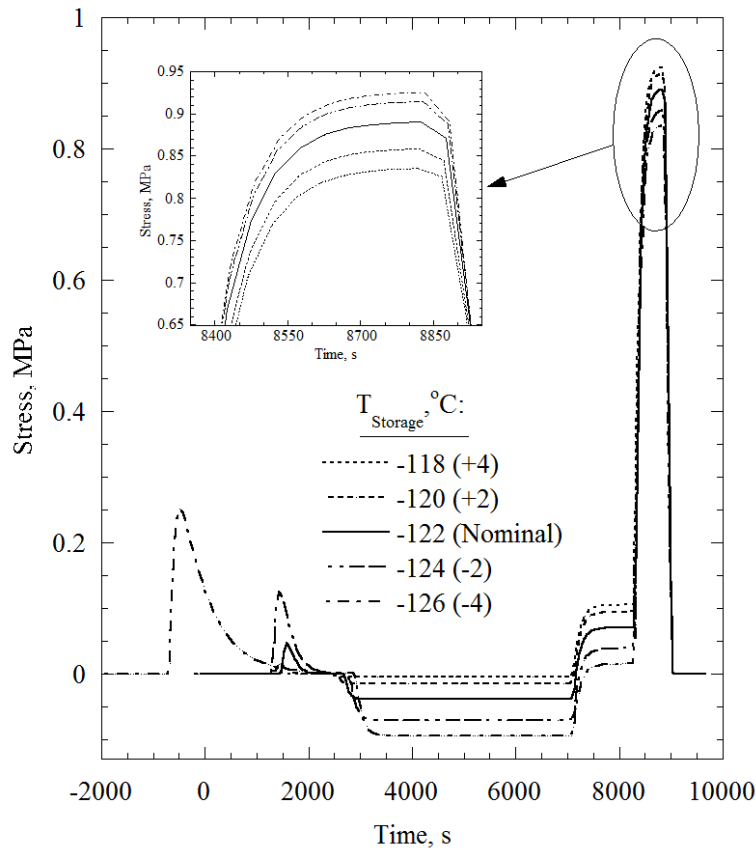


Figure 5.5: Stress history for variable annealing temperatures (stage R2) in Case A. Datasets have been shifted in time such that all have a common onset of rewarming in stage R5—the stage in which maximum stress is found [7].

Temperature hold at a suitable level can noticeably reduce the maximum tensile stress. To the best of the authors' knowledge, this study pioneers the investigation of this effect in the context of cryopreservation, while providing insight into the subtle role of the annealing temperature. It is apparent from Figs. 5.4 and 5.5 that a lower annealing temperature leads to lower maximum tensile stress. Also, a lower annealing temperature leads to higher compressive

stresses during the R_3 section. The change in stress associated with thermal equilibration at the storage temperature is the same in all cases and depends upon the cooling rate R_3 ; the response in this stage is fully elastic. Maximum stress variation with the annealing temperature is associated with how much stress arose when the temperature gradient first develops in R_3 , with the stress range being compressive in this process. If the hold stage is at a sufficiently low temperature, the behavior is akin to the thought experiment for a fully elastic material: the material responds predominantly elastically to the development of the thermal gradient in R_3 and equilibration at storage largely reverses the stress, bringing the storage stress to zero. If the hold stage is at too high temperature, when the viscosity is still relatively low, little stress accompanies the development of the thermal gradient in R_3 (equilibration produces tensile stress at storage like the thought experiment for viscous material transitioning to solid). At intermediate hold temperature level, some stresses arise with the development of the thermal gradient in R_3 and equilibration always producing the same increase in stress, which brings the storage stress to intermediate levels.

Admittedly, lower annealing temperatures lead to slower stress relaxation and, thus, they require longer stress relaxation times (seen in Fig. 5.5). An anneal temperature of -126°C seems appropriate for a glass transition temperature of -129.9°C [43] (viscosity equals 10^{12} Pa-s). This requires a relatively long relaxation time of approximately one hour, while reducing the residual stress at storage by 86% when compared to the reference case. In comparison, achieving a similar reduction in stress merely by slowing the R_3 cooling rate would require excessively slow rates of about $-0.25^\circ\text{C}/\text{min}$, elongating the cryopreservation protocol by 5 to 6 hours.

A limit appears to the extent in which the maximum stress can be reduced by lowering the annealing temperature, when compared with the reference case. All the above scenarios presume zero stresses at the commencement of R_3 , which would be true only if the viscosity is still high enough in R_2 that annealing can occur. Otherwise residual stress from temperature gradients from the R_1 stage can further contribute to the residual stress at storage. To summarize, if a temperature hold is to be beneficial, it must occur within a certain temperature range. At too high temperatures (above, for example, -100°C), the stress relaxation occurs quickly enough during R_3 that residual stress at storage is unaffected by the annealing and is indistinguishable from the stress state due to the reference boundary condition. If the hold temperature R_2 is too low, relaxation is too slow and there is insufficient time to relax the stresses induced by equilibrating

the temperature gradient from R_1 ; the stress at storage can be as high as if the cooling were performed entirely at the high rate R_1 down to storage. Ideally, the anneal takes place at an intermediate temperature that results in low residual stress following a relatively short temperature-hold time.

Note that the stresses prior to equilibration at the storage temperature are tensile at the exterior of the specimen, which can potentially exceed the strength of the material and induce cracking (glassy materials tend to fail due to tension). Hence, an upper limit to R_3 cooling rate exists beyond which fractures would occur. Conversely, the maximum tensile stress during rewarming occurs at the geometric center.

Generally speaking, the storage temperature in R_4 has no effect on the maximum tensile stress. However, this statement comes with one big caveat: the maximum tensile stress is only R_4 independent if the thermal gradient is fully developed (i.e., the material is cooled at the exact same cooling rate regardless of the spatial location) before the sample reaches the glass transition temperature range. One could imagine a situation where R_4 storage occurs at a high temperature (such as R_4 of -140°C) and R_5 is fast enough that before the thermal gradient is fully developed (i.e. before stress reaches its maximum), the material becomes warm enough that stress relaxation begins. For example, this is exactly what happens when the R_5 rewarming rate reaches a value of $7.5^\circ\text{C}/\text{min}$. However, when using a slower R_5 rewarming rate (such as $R_5=1.875^\circ\text{C}/\text{min}$, which also happens to minimize stress), the thermal gradient is fully developed before the glass transition region for all R_4 values tested, thus the maximum stress is completely R_4 -independent.

The attention is now shifted to viscosity near glass transition. The logarithmic slope of the viscosity with temperature is similar for all three solutions analyzed [43], where the primary difference between the datasets is in a temperature shift corresponding to the different glass transition temperatures. Hence, the maximum tensile stress for all three viscosity functions is essentially the same as long as the annealing temperature is also shifted accordingly (-8.2°C for DMSO and $+2.73^\circ\text{C}$ for DP6). While the material properties for the different solutions may vary [1–4,37,39,42], unlike the simplified assumption in the current analysis, the thermal protocol strategy to minimize stress would still work in all cases as long as the R_2 annealing temperature is shifted appropriately.

5.3.3 Simulations for CPA and Container – Case B

Case B models stresses that develop in many realistic cryopreservation protocols, such as in a recent cryomacroscope study [6]. Here, the top surface is assumed to be thermally insulated, which is consistent with negligible heat transfer rate from the CPA upper surface to an air gap above it. This assumption corresponds to free convection above the CPA as opposed to high forced convection of the outer walls. The stress history in the CPA within the container essentially follows the same process as in Case A, with an additional effect resulting from the mechanical interaction between the container and the solution after it has entered into the elastic-dominant state, as schematically displayed in Fig. 5.6.

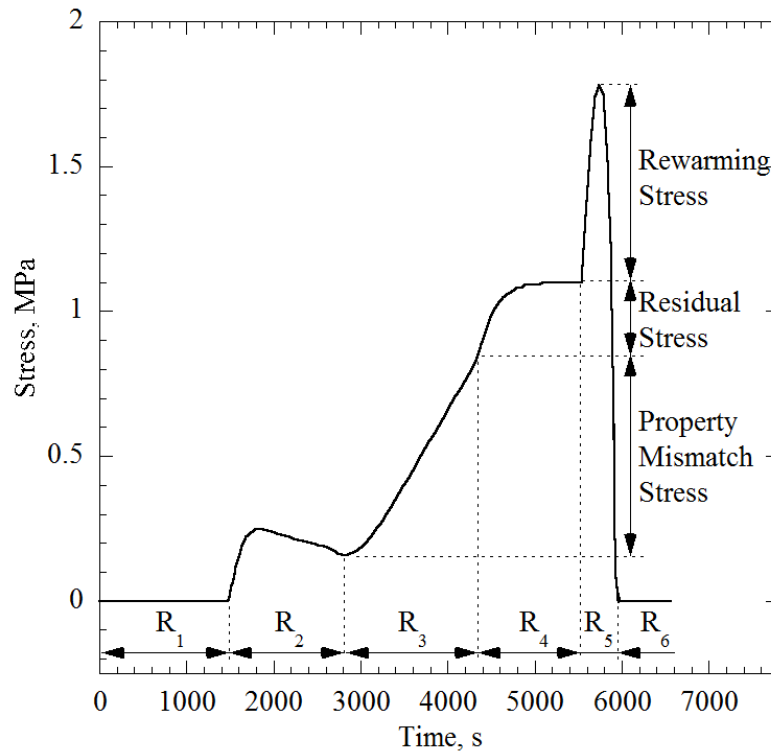


Figure 5.6: stress history for CPA within a container with the three stress components clearly labeled. The stress history was chosen so as to make each component clearly visible. Also, note how the stress relaxation in R2 is slower when compared to the stress relaxation for a CPA without a container [7].

The CPA and the container tend to contract at different rates consistent with their thermal expansion coefficient values, with the CPA tending to contract more. Due to continuity in displacement at the CPA-container interface, the container prohibits the CPA from contracting as

much as unconstrained contraction would yield (Case A), and so the entire CPA domain goes into a state of tensile stress. This effect may intensify the overall tensile stress that would otherwise develop in the absence of a container.

One strategy to minimize the added stress imposed by the container is to reduce its ability to restrain the CPA. A container with a lower Young's modulus or a thinner wall is more compliant, and thus less able to constrain the solution against thermal contraction. A different strategy could be to select a container material with thermal expansion coefficient closer to that of the CPA and, thereby, lower the thermal strain difference between CPA and container. While all of these approaches could reduce the maximum tensile stress in the CPA, the current investigation is focused on the thermal boundary conditions, and so the strategy adopted here is to vary the boundary conditions instead of modifying the material properties or geometry. For example, minimizing the differential thermal strain between the two materials by elevating the storage temperature reduces the stress level.

The location of maximum stress in Case A was always at the geometric center due to symmetric boundary conditions. Due to asymmetric wall effects and thermal boundary conditions in Case B, the location of the maximum stress is now shifted off center. The location of the maximum stress was found in one of two locations, depending on the thermal boundary condition (see Fig. 5.1). When the stress due to differential thermal strain dominates, the maximum stress is found where the base is connected to the wall. Alternatively, when the stress due to thermal gradients (i.e. residual stress at storage and additional stress upon rewarming) are more significant, then the location of maximum stress will be offset down and to the right from the geometric center. Fig. 5.7 displays the differences between the stress histories at these two locations. Using Fig. 5.6 as a guide, one can clearly see the distinct stress modes in Fig. 5.7(a), while only the stresses due to differential thermal strain are visible near the container wall as shown in Fig. 5.7(b).

Comparing the results displayed in Fig. 5.7 with those displayed in Figs. 5.4 and 5.6 it can be concluded that, due to the restraining effects of the container, the rate of stress relaxation in Case B is significantly slower than in Case A. This means that annealing times at R_2 for a given temperature take significantly longer than for CPA without a container (over 100 min vs. approximately 13 min at -120°C for the particular container properties and geometry used in the current study). Even partial annealing can reduce the maximum residual tensile stress, as long as

the portion of stress in R_2 which did not relax is smaller than the residual stress that would be generated due to the thermal gradients in R_3 . However, this significantly slower annealing time makes the benefits of annealing more ambiguous and dependent upon the particular system geometry, container material, and cryopreservation protocol.

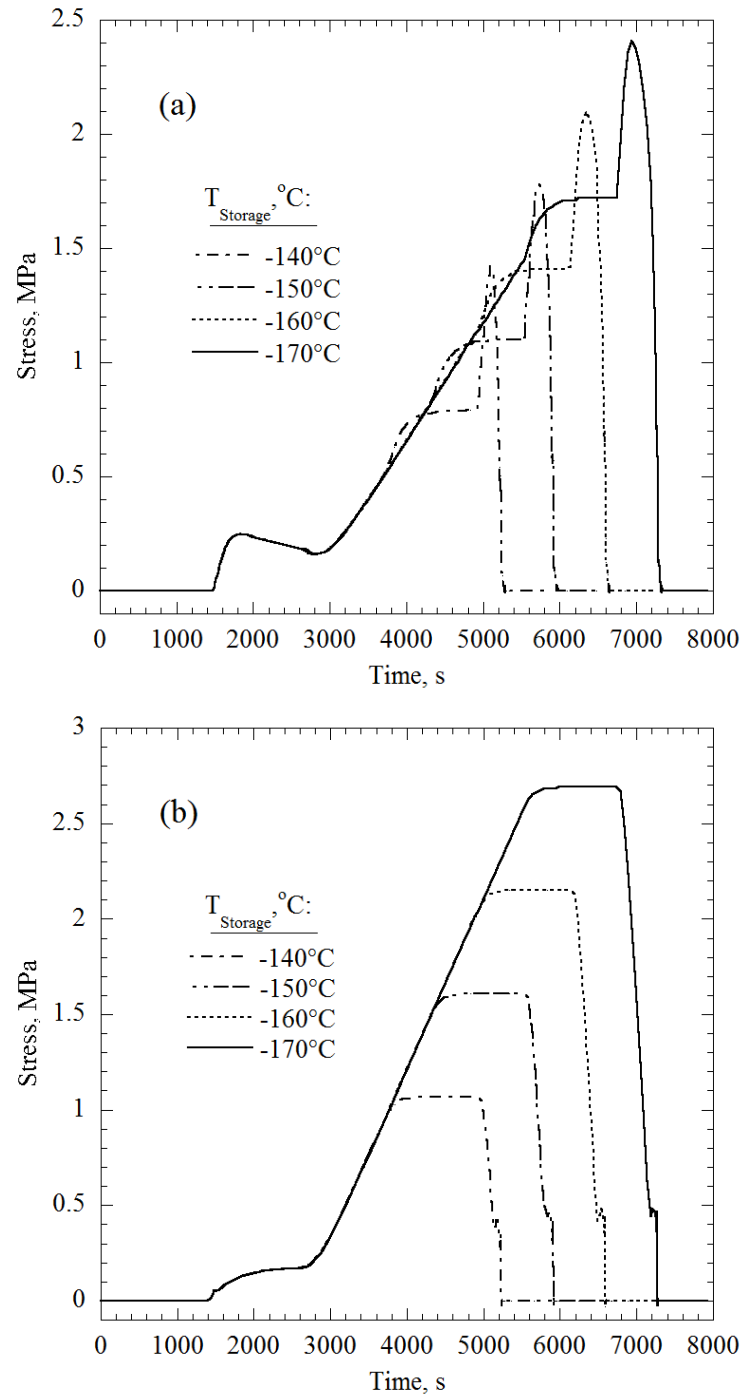


Figure 5.7: (a) Stress history at the location offset from the center for the R4 variations, and (b) stress history at the bottom right corner for the R4 variations; see σ_B in Fig. 5.1 [7].

5.4 Summary and Conclusion

Investigating the effects of the thermal history on the resulting mechanical stress has been the subject of several previous studies and is a staple of efforts to cryopreserve large-size samples. The current study focused on annealing effects, subject to varying thermal history parameters, such as the rate of cooling, rewarming, and storage temperature. Several independent empirical studies have reported on fractures in cryopreserved materials, subject to mechanical stress levels similar to those simulated in the current study. Consequently, empirical studies have suggested that the likelihood to fracture is strongly dependent upon the cooling rate when approaching cryogenic storage (R_3) and the subsequent initial rewarming rate (R_5). The current study provided explanations for those previous observations and further insight into the affecting mechanisms. This study theoretically investigated—for the first time—the effects of annealing, and how it can reduce stress while minimizing its dependence on the cooling rate.

Theoretical results suggest that the residual tensile stress at storage can be reduced by 86% compared with the reference by using low temperature annealing, and that additional stress upon the onset of rewarming can be reduced by 75% by using a slower rewarming rate. Additionally, it was shown that provided that the thermal gradients are fully developed before crossing the glass transition region, the maximum tensile stress is independent of the storage temperature. Finally, it was shown that for the three CPA solutions where viscosity data exists, the viscosity value is not particularly important as long as the annealing temperature is appropriately shifted with respect to the glass transition temperature.

Some of the mechanical effects present in CPA within a container were elucidated in this study. Firstly, it was shown that stresses due to thermal gradients are controlled by the initial rewarming rate (R_5) and by either the annealing time and temperature (R_2) or the cooling rate (R_3). Additionally, it was demonstrated that stresses due to differential thermal strain between CPA and container are dependent on the storage temperature. Also, the parameters that affect the location of maximum stress for CPA within a container were discussed, while the restraining effects of the container on the rate of stress relaxation were investigated. Based on these observations, the authors suggest the following guidelines when developing a cryopreservation thermal protocol: (i) use a container that is as compliant as possible, such as an FEP bag; (ii) if this is not practical, storage temperature should be as high as possible (though still below the

glass transition region); (iii) an annealing stage appears to be a better way of lowering residual stress than using slow cooling rates with a compliant container, but slow cooling rates may be more effective for cryopreservation within a rigid container; (iv) annealing significantly reduces stress when carried out at a few degrees above glass transition; (v) stresses are highly dependent upon the initial rewarming rate, with very slow rewarming up to an intermediate temperature drastically lowering maximum tensile stress; and, (vi) thermo-mechanical analyses of specific container geometry and materials can be used as an effective tool to further reduce the likelihood to structural damage during cryopreservation.

While the critical stress threshold below which fractures will not form may be difficult to evaluate, by learning which boundary conditions minimize stress and what the most significant driving forces are, it is plausible to design more effective thermal protocols for the benefit of cryopreservation practice

5.5 Effect of Container on Annealing Time

When this article was published, the precise method by which the container affects the annealing time was not fully understood. In [104], George Scherer analyzes the thermal stress in a sandwich seal composite, which consists of a panel of elastic material, sandwiched between two panels of a glassy material and are shown schematically in Fig 5.8. The details of the stress

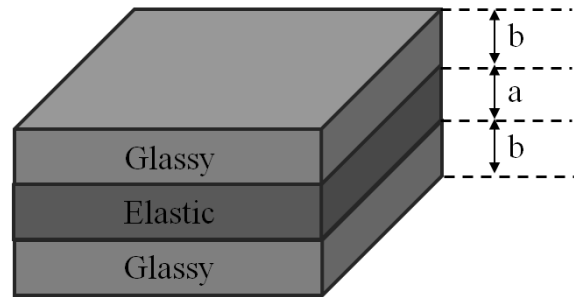


Figure 5.8: Schematic illustration of sandwich seal composite

solution and its derivation are well outside the scope of this section. One very important equation is the stiffness ratio, n :

$$n = \frac{2b}{a} \frac{E_G}{1 - \nu_G} \frac{1 - \nu_E}{E_E} \quad (5.5)$$

The stress relaxation time constant, τ , is proportional to the stiffness ratio, n . This means that as the stiffness ratio increases, the stresses in the system take longer to relax and vice versa. Since the Young's modulus of the elastic part of the sandwich seal is in the denominator, this means that stiffer elastic components lead to faster relaxation times. When n is small, the glassy parts are sustaining most of the stress and strain. Based on Eq. (5.2), the high stress will lead to high

viscous strain rate, which will speed up the relaxation time. On the other hand, when n is small, the elastic parts will be undergoing the majority of stress and strain, then there is very little driving force for viscous strain and the relaxation times will be very slow.

The example of CPA within a container obviously has some very different characteristics than the sandwich seal and Eq. 5.5 probably cannot accurately describe the relaxation time constant. However, the basic idea of how stiffness ratio between the glassy and elastic parts will affect relaxation time constant should still hold. This hypothesis was tested by using the same model as in case B of the annealing study. The thermal protocol was simplified so that it was just a single cooling rate followed by a hold at -120°C .

The CPA is initially stress free, then it undergoes tensile stress at its center as the temperature gradient flattens at the beginning of the hold. As the hold continues, the stress relaxes toward zero. The elastic modulus of the container was varied from 0.8625 GPa to 13.8 GPa to investigate its effects on the relaxation rate. As shown in Fig. 5.9, stiffer containers initially lead to higher stresses as the thermal gradient equilibrates. However, the stiffer containers also lead to faster stress relaxation, and if allowed to relax long enough, can actually lead to lower stress [104]. It is generally assumed that mechanical stress is reduced by using a more compliant container. This is often the case, but there are definitely instances, especially when employing annealing, when a stiffer container may actually help to reduce stress as shown in this simple analysis.

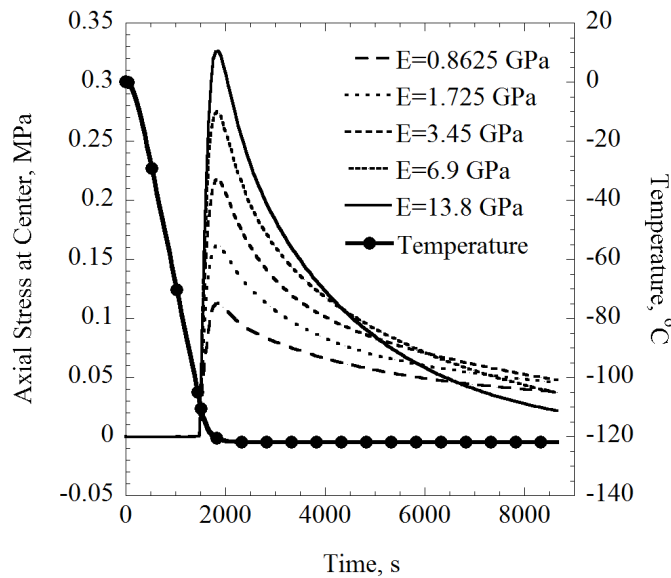


Figure 5.9: Effect of container stiffness on stress relaxation time

Chapter 6: Photoelastic Analysis

The cryomacroscopic is a proprietary device invented at the Biothermal Technology Laboratory for the *in situ* visualization of physical events in large-scale cryopreservation [6,34,49,65,77,116,117]. The current study provides insight into thermo-mechanical effects in scanning-cryomacroscopy experiments [6], as they pertain to polarized light and photoelasticity effects [116,117]. Feig and Rabin [76,116,117] designed and constructed a scanning cryomacroscopic that integrates polarized light means with two primary objectives: to enhance the visualization of physical effects associated with the kinetics of crystallization, and to provide means for photoelasticity investigation. From the wide range of effects demonstrated previously [116,117], this chapter focuses on interpretation of thermo-mechanical stress associated with visualized photoelasticity.

6.1 History of the Cryomacroscopic

At the cellular level, visualization of cryoprotocols is commonly done with the cryomicroscope [15,77–79,105–107]. In cryomicroscopy, representative micro-slices are exposed to conditions similar to those that would prevail in a large-scale specimen at selected points, such that a complete picture of the process can be piecewise-assembled. Due to the large differences in surface-area-to-volume ratio, thin samples may behave conceptually different than bulk volumes under the same conditions. As a part of an ongoing effort to develop means for cryopreservation of bulky specimens and organs, an early device prototype was developed to visualize macro-scale physical events [49], which we termed the cryomacroscopic. In cryomacroscopy, the large-scale specimen is analyzed as a whole—in situ. The applications of cryomicroscopy and cryomacroscopy are considered complementary, as observations made by both applications may be useful to develop scale-up cryopreservation techniques.

The evolution of cryomacroscopy has resulted in four prototypes for various applications. The first generation prototype (Cryomacroscopic I) was developed to study vitrification in a 15 mL vial, using a dedicated passive cooling mechanism, where physical events were VHS recorded with a monochrome CCD camera [49,108] Results obtained with Cryomacroscopic I demonstrated—for the first time—that micro-fractures in the glassy state may serve as nucleation sites during the rewarming phase of the cryopreservation protocol. Furthermore, this device was demonstrated as a critical tool for the investigation of mechanical stresses induced by the

contraction of the container walls [34]. Additional investigations with Cryomicroscope I were focused on correlating physical events of crystallization and fracture formation with functional recovery of blood vessels [58,81].

Cryomicroscope II was developed to study solid-mechanics effects in thin films [65]. This device was designed to measure the yield strain (strain to fracture), the repeatability of fracturing events, patterns of fracture formation, and the potential effect of tissue specimens on stress concentrations in a large vitrified domain [109]. Unlike Cryomicroscope I which was used to study representative common cryopreservation protocols, Cryomicroscope II was designed specifically to investigate solid mechanics effects and improve modeling. The thin-film model was chosen due to its simplicity in solid mechanics analyses.

Cryomicroscope III has been recently presented to investigate physical events associated with vitrification in the presence of synthetic ice modulators (SIMs) [77]. The main improvement in Cryomicroscope III is that it has been redesigned as an add-on to a commercially available top-loading controlled-rate cooler, thereby improving its potential dissemination for the benefit of the cryobiology community. This device further benefits from an improved high-speed color camera and illumination via fiber optics. Another significant development is a computer code for process control and post-processing of experimental data, with a single digital movie as the Cryomicroscope III end product. Results obtained with this device indicate improved suppression of crystallization with the application of SIMs and unexpected phenomenon of solutes precipitation during rewarming [77].

While Cryomicroscopes I-III are designed to visualize physical events with a stationary camera in a similar arrangement to the cryomicroscope setup (top-down viewing), Cryomicroscope IV is designed for vertical scanning of samples larger than the field of view of the camera, using a computer-controlled stepper motor and a carriage system. Cryomicroscope IV is design as an add-on unit for commercially available, top-loading, controlled-rate cooling chambers. These scanning capabilities enable cryopreservation investigations on a wide range of specimen configurations, containers, and commonly practiced thermal protocols. This setup serves as the platform for development of polarized-light cryomicroscopy in the current study.

6.2 Introduction to Photoelasticity

The history of light polarization began with the discovery of double refraction by Erasmus Bartholinus in 1669 [110]. Visualization of stresses in transparent amorphous materials using polarized light was first documented in 1815 by Brewster [111,112] and is commonly referred to as photoelasticity [113]. The physical principles of light, optics, and their role in photoelasticity have been well documented in the literature over the past two centuries and are addressed herein in brief only, for the completeness of experimental-setup presentation.

When two similar polarization filters are placed on a common axis parallel to one another in an orthogonal polarization orientation, any light ray pointing in the same direction through the filters couple will be blocked. The filter closer to the light source is commonly referred to as the polarizer and the other filter is commonly referred to as the analyzer or decoder. Any object placed in between the two filters may refract the propagating light, which may cause some of it to pass through the analyzer. It is this refraction effect that may enhance visualization, even from small objects that otherwise could not have been seen using the same available optics. In the context of microscopy and cryobiology for example, Luyet [82] used polarized light to better view intermixed frozen and glassy regions in cells, whereas Menz and Luyet [106] enhanced the appearance of fractured surfaces at the cellular level.

Photoelasticity is a whole-field, graphic stress-analysis method based on an optical-mechanical property called birefringence which is possessed by many transparent media [113]. When a photoelastic specimen is placed between the polarizer and analyzer, fringe patterns are exhibited, related to the difference between the principal stresses. For “dark-field” photoelasticity, as used in this study, any unstressed area will appear dark as all the light will be blocked by the orthogonally oriented filters. Areas of relatively higher stress will brighten due to the increase in light refraction from increased mechanical stress. The increasing stress may refract the light through the entire visible spectrum, and even create a spectrum-repetition pattern when the stress range is very high [113]. An experimenter may estimate the magnitude of the stress by quantifying the light spectra, but this process requires some a priori knowledge about the field of stress for calibration purposes.

The current study combines for the first time polarized light with cryomacroscopy, using Cryomacroscopy IV as a development platform. Polarized light is used for visualization enhancement as well as for demonstration of photoelasticity effects, as they pertain to the study

of cryobiology. In particular, the current study builds upon recent studies by the authors [6,77], where polarized light is now replacing non-polarized light.

6.3 Experimental Apparatus

Since Cryomacroscopy IV [6] serves as the platform for developing polarized cryomacroscopy, the cryomacroscopy is presented here in brief only for the completeness of presentation, while emphasis is given to the currently added polarization setup. With reference to Fig. 6.1, due to the harsh environment surrounding the sample, all electronic components and mechanisms are placed externally to the cooling chamber. Light is delivered by various fiber-optics bundles, while the image of the specimen is delivered by means of a borescope (Hawkeye HH2992, Gradient Lens Corporation, Inc., NY, USA). The cryomacroscopy comprises of the following key elements:

- (i) A commercial cooling chamber and controller (Kryo 10-16 controlled by Kryo 10-20, Planer PLC, UK).
- (ii) A cryogenic stage placed within the cooling chamber, Fig. 6.2. This unit is essentially the experimentation platform, which has been modified for the purpose of the current study and is described in more detail below.
- (iii) A high-speed, light-sensitive, CCD camera (Grasshopper, Point Grey Research, Inc., BC, Canada), connected to the external end of the borescope.
- (iv) A stepper motor and a controller (AMH-22 controlled with DCB-274, Advanced Micro Systems, Inc., VT, USA) to facilitate vertical scanning by the camera and borescope.
- (v) A T-type thermocouples array for monitoring the thermal history, attached to a data acquisition system (OMB-DAQ-56, Omega Engineering, Inc., controlled by DaqViewTM).
- (vi) An LED light source and fiber-optics bundles to provide diffuse illumination onto the sample (End Glow 5/16" cables illuminated with Photon-Lite, FO Products, Inc.).
- (vii) A polarized-light source, a dedicated fiber-optics bundle, a mirror, and filters, to provide polarized-light conditions as described below.
- (viii) A proprietary cryomacroscopy control code (C³) to control the various cryomacroscopy components, real-time monitoring of images and temperatures, data streamlining, and post-processing to create a digital movie with time and temperature data overlaid.

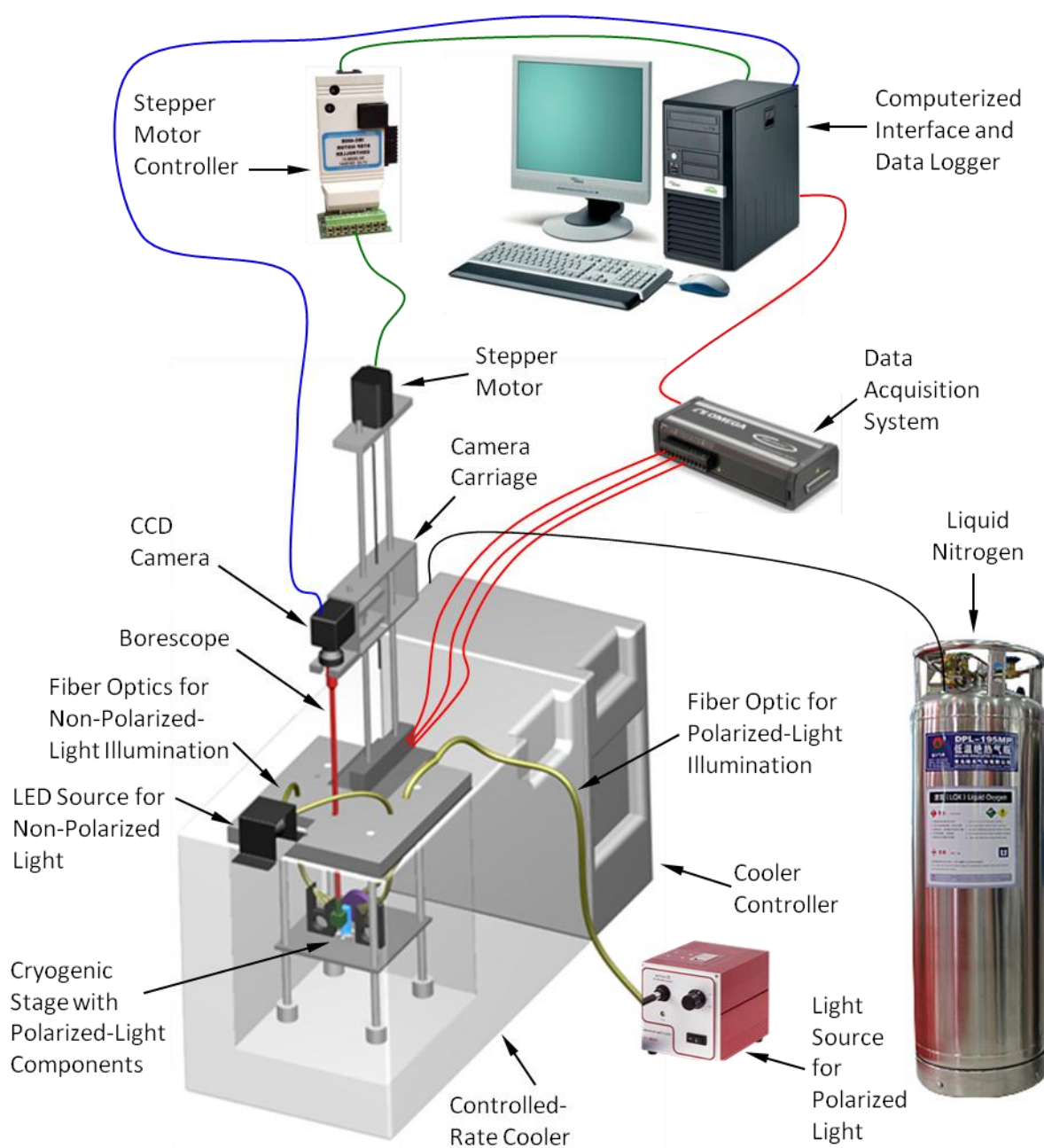


Figure 6.1: Schematic illustration of the Cryomicroscope IV assembly incorporating polarized-light illumination. A personal computer is used for hardware control, data acquisition, and post-processing [116].

Figure 6.2 displays the modified cryomicroscope stage and its components. While different transparent containers and vials can contain the specimen, the current study uses a cuvette due to its superior optical properties and minimal specimen distortion. Two cuvette materials have been tested: a disposable polystyrene cuvette (Plastibrand, BRAND GMBH + CO KG, Germany) and

a quartz cuvette for cryogenic temperatures (NSG Precision Cells Inc.). While the polystyrene cuvette was found to be inexpensive and of acceptable optical clarity in non-polarized-light conditions [6], residual stresses and photoelastic effects prohibited its use in polarized-light conditions. While the quartz cuvette was found to be superior for photoelastic investigation, it is much more expensive and far more susceptible to structural failure when fractures form in the CPA domain. The quartz and polystyrene cuvettes are of the same dimensions ($12.5 \text{ mm} \times 12.5 \text{ mm} \times 45 \text{ mm}$) and preserve continuity in data analysis with previous studies [6].

The cryogenic stage is designed to alternate between non-polarized light and polarized light on demand. With reference to Fig. 6.2(a), the non-polarized light is directed perpendicular to the field of view, which was found to best enhance effects such as fractures and crystallization. The fiber-optics spreader has been designed and 3D-printed (ABS) for illumination at 45° to the cuvette surface, in order to further prevent reflections from the cuvette outer surfaces.

To facilitate the polarized-light investigation, light was delivered from an external halogen-light source (150W at 3200K, Thorlabs Inc.), through a high-quality fiber-optics bundle (91 cm in length, 6.4 mm in diameter; Core Fiber Bundle, Thorlabs Inc.) to an aluminum housing of a silver-coated, beam-turning mirror (97.5% reflectivity, Thorlabs Inc.). The mirror directs the light perpendicular to polarizer (50 mm in diameter), illuminating the cuvette in the direction of the red-dashed arrows in Fig. 6.2(b). An analyzer (12.5 mm in diameter) has been retrofitted to the tip of the borescope by means of a 3D-printed (ABS) housing. Note that the borescope setup includes an internal 45° mirror to reflect the polarized light into the axial direction of the borescope. Both polarizer and decoder are made of a 0.3 mm-thick dichroic polarizing film sheet (>99% efficiency, Thorlabs Inc.), sandwiched between two protective glass windows. Each window has an antireflective coating which is optimized for the visible spectrum of 400 nm to 700 nm.

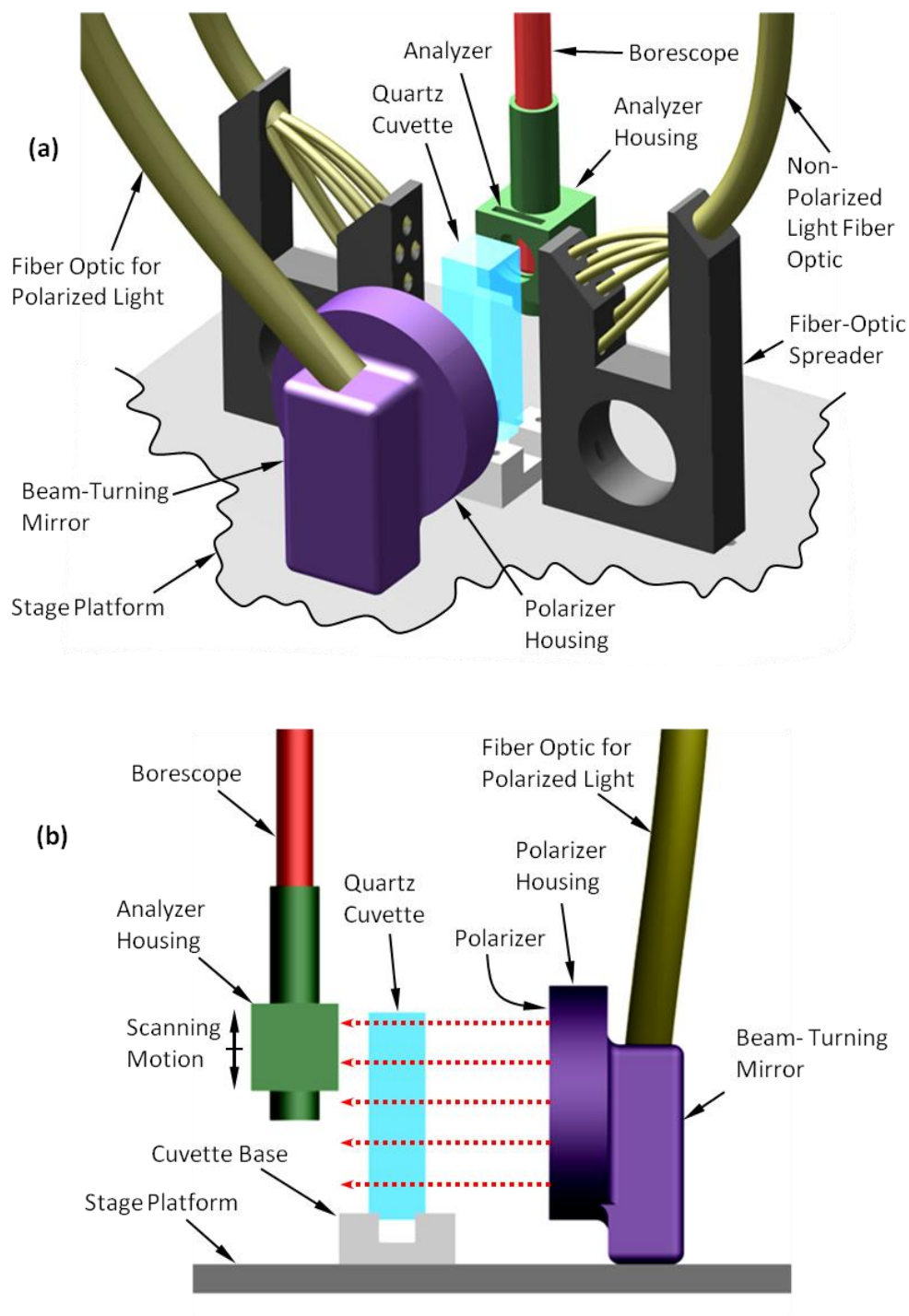


Figure 6.2: Schematic illustration of the Cryomicroscope IV stage incorporating components for polarized-light visualization: (a) isometric view including components used for non-polarized light, (b) side view showing polarized-light components only, where the red-dashed arrows mark the direction of polarized light propagation [116].

6.3.1 Polarized-light Protocol

Prior to experimentation, the rotational orientation of the polarizer and analyzer are set perpendicular to one another. In practice, this is achieved by rotating the polarizer in its housing until the illuminated image under investigation appears dark. Next, the brightness dial on the halogen-light source is set in the range of 0 to 11, which corresponds to a power range of 0 to 150 W, respectively. Maintaining repeatable illumination power is critical for a comparative study of visualization effects under similar conditions. While the highest brightness level may be optimal for detecting the onset of crystallization and early stress formation, the increasing stress may cause saturation to the CCD sensors, leading to blurring and low definition between repeated color spectra created by photoelasticity. At the extreme, this artifact may lead to a complete white image preventing any discernible observations. For the current combination of CCD camera, polarizer, decoder, and optical components, a power range of 4 to 7 was found effective (55 to 95 W, respectively). Analysis of captured images outside of this range led to inconclusive observations, either too dark or too bright, respectively. In the current study, a power setting of 4 (55 W) was found most efficient to visualize photoelasticity effects below glass transition. Furthermore, a power setting of 7 (95 W) was chosen for experiments when early stress development and the onset of crystallization were investigated.

6.4 Analysis of previously unknown phenomenon

Understanding the following section requires a little bit of knowledge about the structure of glasses, so the next two paragraphs will take a slight detour in order to explain the relevant issues. For a more exhaustive explanation, see [104]. As described by Tool [83] and refined by Narayanaswamy [84], certain properties of a glassy material such as thermal strain and enthalpy have temperature dependent derivatives composed of a glassy (time independent) component and a structural (time dependent) component. Analogous to a step change in the strain for a Maxwell fluid, a step change in temperature for a glassy material causes an instantaneous (glassy) response as well as a transient (structural) response. The amount of time required for the structural response to achieve structural equilibrium is characterized by the structural relaxation time constant.

As temperature decreases, the structural relaxation time constant increases, meaning that it takes longer for the material to achieve structural equilibrium. A property known as Fictive

Temperature is the temperature the material would have to be at, while in structural equilibrium, to have the same structure as the material at its current temperature. At high temperatures, the material is in structural equilibrium and the fictive temperature equals the actual temperature. As it cools, and the structural relaxation time constant becomes slower, the material deviates from structural equilibrium and the fictive temperature falls behind the actual temperature. Once the material is cold enough that the structural relaxation time constant is effectively infinite, the fictive temperature cannot go any lower despite possible additional cooling (this is one definition of the glass transition temperature). Just as actual temperature gradients can cause mechanical stress, fictive temperature gradients (through material property gradients) have also been known to cause mechanical stress [104].

Figure 6.3 displays a sequence of photoelastic images of the CPA within a container as it rewarms. The thermal history of the free stream thermocouple is presented in Fig. 6.3(f); the power setting of the polarized-light source is 65 W. In Fig. 6.3(a), the material is highly stressed relative to the later images in Fig. 6.3(b) – 6.3(d) as evidenced by the comparatively bright regions. This stress is mostly due to the thermal strain mismatch between the quartz cuvette and the vitrified CPA. The temperature at the walls is in the proximity of the glass transition temperature for 7.05 M DMSO [85]. In Fig. 6.3(b), the domain is at a higher temperature than in Fig. 6.3(a), this has lessened the thermal strain mismatch, and is clearly visible from the reduced intensity of the brightness, particularly in the center of the CPA domain. The temperature at the walls is just above the glass transition temperature, allowing the material to relax as shown by the dark front starting at the walls moving inward; this is expected for external warming in our chamber.

As the material continues to warm, the material near the wall re-brightens (Fig. 6.3(c)), then that brightness moves toward the center (Fig. 6.3(d)) until the entire domain darkens when the material is finally warm enough to undergo significant stress relaxation (Fig. 6.3(e)). Assuming constant thermal and mechanical properties, one would expect the stress in the material to be decreasing everywhere in the domain during rewarming due to the reduced thermal strain mismatch. To the best of the authors' knowledge, this re-brightening at the walls which then moves towards the center of the domain has not been viewed before in the context of cryopreservation, and its cause is currently unknown. What follows is one plausible explanation based on the ideas of fictive temperature as described above.

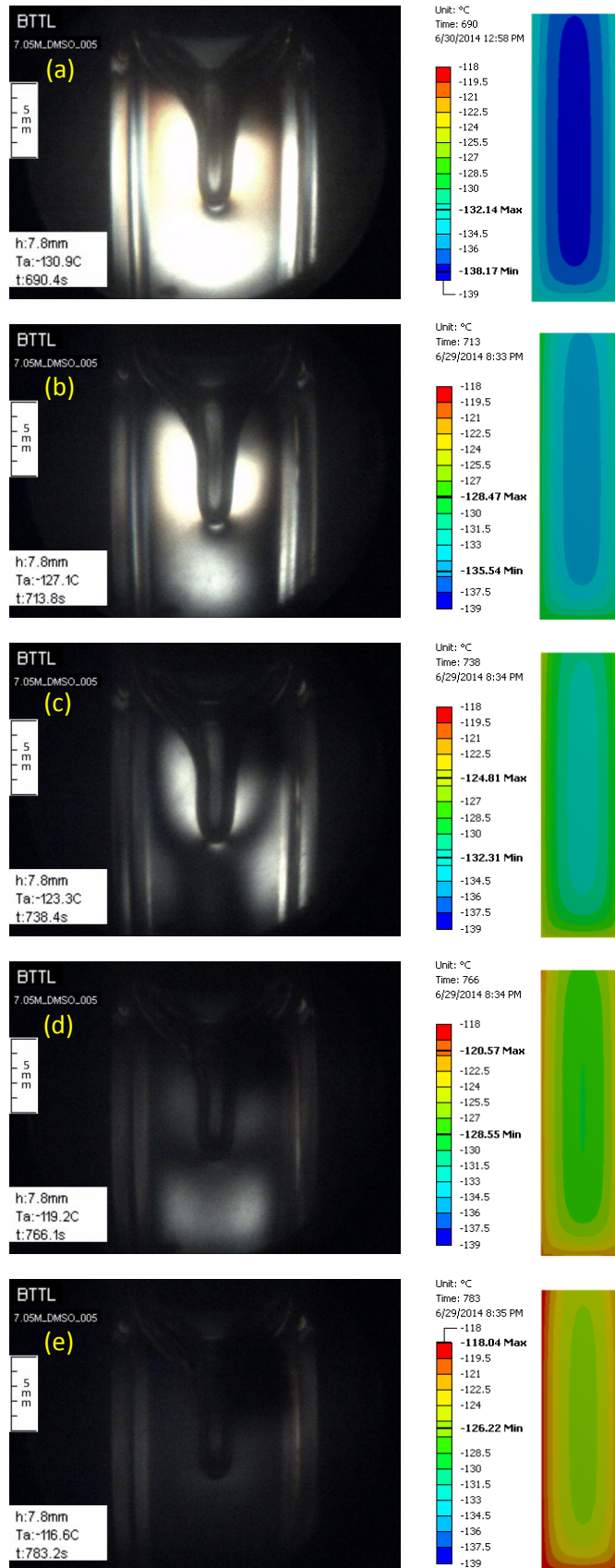


Figure 6.3: Photoelastic effects during rewarming of vitrified material: (a) beginning of rewarming with relaxation at the wall (warmest point); (b) relaxation continues with stresses staying higher in the region trapped between the cavity and the wall; (c) the development of additional stresses at the walls as the CPA passes through glass transition; (d) the propagation of these additional stresses during glass transition towards the CPA center; (e) complete relaxation; (f) thermal history of the free stream thermocouple; and (g) Illustration of fictive temperature: the fictive temperature is calculated by connecting a line beginning at the current value of a property, p , parallel to the glassy modulus, α_g , to a line collinear with the liquidy modulus, α_l . [117].

For a constant cooling/rewarming rate, the effect of structural relaxation can be thought of as causing a non-linear thermal strain curve as shown in Fig. 6.3(g). The slope of this curve, known as the coefficient of thermal expansion, transitions from a high value, α_l , to a low value, α_g , during the glass transition process and is equivalent to a change in the fictive temperature gradient. This change in the coefficient of thermal expansion causes the material to experience a jump in its stress value as it goes through glass transition even though the thermal gradient remains unchanged. This effect has been well documented within the glasses literature [83,84]; however, to the best of the authors' knowledge, it has never been observed, measured, or even discussed within the cryobiology literature.

Based on this understanding of structural relaxation in glassy materials and how they can affect stress, the following hypothesis is proposed to explain the “re-brightening” in Figs. 6.3(c) and 6.3(d). There are two issues effecting stress (and thus the brightness of the image) in Fig. 6.3. Firstly, as the material warms the thermal strain mismatch between the CPA and the cuvette decreases, thus decreasing stress (and dimming the image as visible in Figs. 6.3(a) and 6.3(b)). Additionally, as the CPA goes through glass transition (beginning at the walls and proceeding inwards), there is a change in the fictive temperature gradient, accompanied by a change in coefficient of thermal expansion, which increases the stress (brightening the image in Figs. 6.3(c) and 6.3(d)) until the glass transition process is complete and stress relaxation takes over and the image darkens again (Fig. 6.3(e)). During cooling, stresses would be forming around glass transition both because of changes in fictive temperature gradient and thermal expansion mismatch between the CPA and cuvette, thus it would be difficult to differentiate between the two. However, during rewarming, stress due to thermal expansion mismatch would be decreasing while stress due to fictive temperature gradients would be increasing; this could potentially allow somebody to isolate the effects of the fictive temperature gradient.

6.5 Experimental Investigation of Annealing

A study investigating the effects of annealing via FEA was presented in chapter 5 and has previously been published [7]. Here, photoelasticity is used to experimentally validate that study. Figure 6.4 displays annealing effects by means of photoelasticity in 7.05 M DMSO subject to

illumination power of 95 W. This CPA type and concentration have been selected for investigation due to superior glass forming ability and the low critical cooling rate to form glass of $2.5^{\circ}\text{C}/\text{min}$ [86]. DMSO at this concentration is very toxic and cannot be used for practical cryopreservation applications. However, 7.05 M DMSO has been identified as a preferred reference solution to study thermal stress in cryopreservation [37]. An intermediate hold temperature at -125°C was selected for this experiment based on FEA [7], which is about 5°C above the glass transition temperature as measured by DSC (T_g in the range of -130°C to -132°C [37,85]).

The cavity formed at the center of the CPA-air interface shown in Fig. 6 is the result of differential contraction [6], as the spatially distributed temperature field is cooled at a close-to-uniform rate of $20^{\circ}\text{C}/\text{min}$ throughout most of the initial cooling phase, Fig. 6.4(e). Figure 6.4(a) displays the photoelastic effect in the specimen at the onset of the intermediate temperature hold, implying stresses first forming closer to the outer walls. Figures 6.4(b) – 6.4(d) display how the stress magnitude increases with time up to about 90 seconds from the beginning of the temperature-hold phase, and anneal away thereafter. The domain was considered annealed when there was no stress visible in the real-time image, and when the intensity of a screenshot image closely resembled the original intensity before stresses start to develop at the onset of the temperature-hold, with the comparison of Figs. 6.4(a) and 6.4(d) as examples. The annealing process in this protocol took approximately 5 minutes.

Figure 6.5 compares the stress field at storage in a sample of 7.05 M DMSO for a protocol that includes annealing against one that does not. Again, an intermediate hold-temperature at -125°C was selected for this experiment. In the experiment presented in this section the saturation properties of the camera are altered at the beginning of the experiment to enable a gray scale image, opposed to the color images which were presented before. The purpose of the gray scale image is to enable intensity analysis without having the loss of information when converting a colored image to a gray scale format.

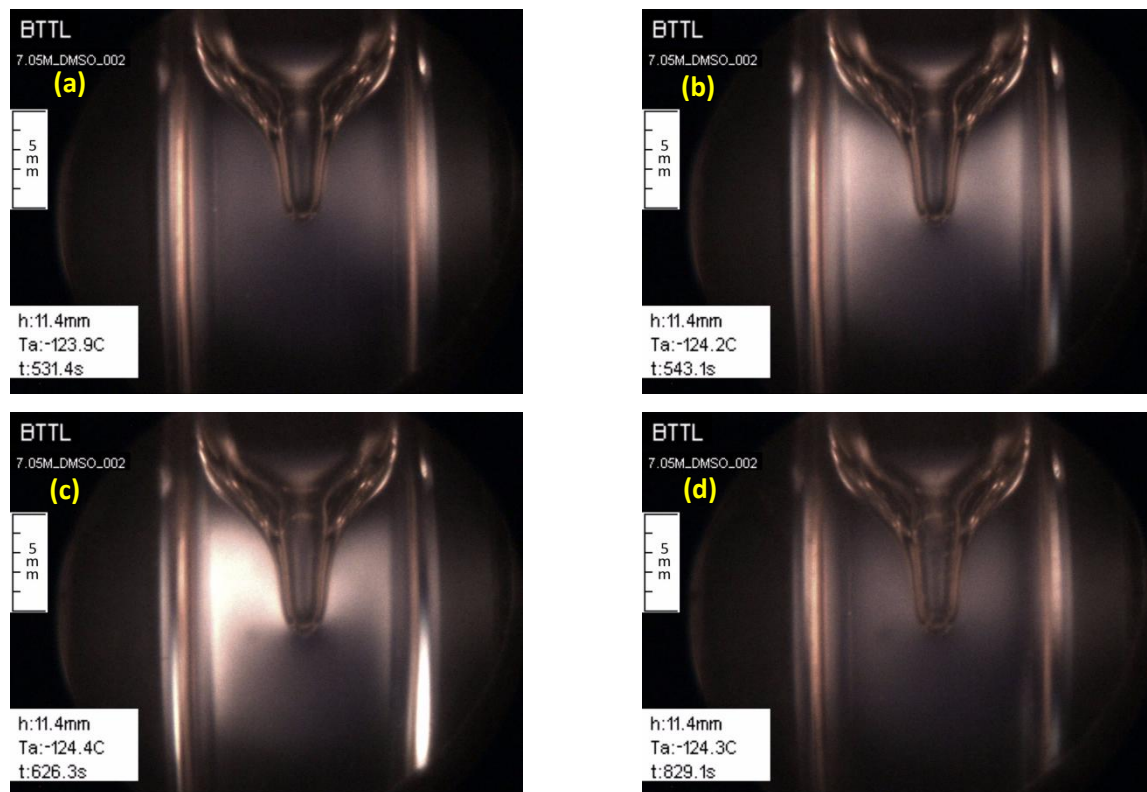
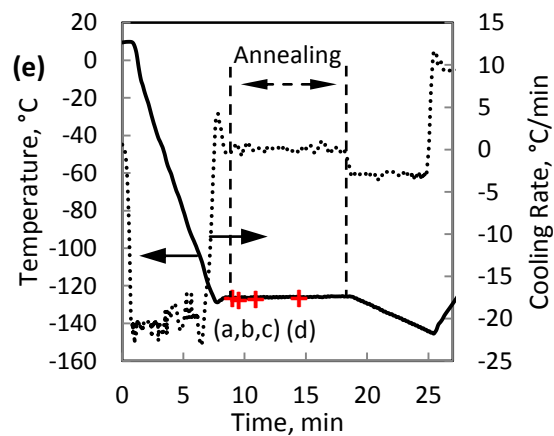


Figure 6.4: Representative images showing the process of stress build-up and subsequent annealing in 7.05 M DMSO at 95 W, with an intermediate temperature-hold of -125°C , which is 5°C above the glass transition temperature: (a) stress starts to build up at the beginning of the temperature-hold period, with the highest level appearing at the walls; (b) the stress level continues to increase with its maximum value propagating inwards towards the cavity; (c) the maximum stress was observed approximately 90 seconds after the beginning of the temperature-hold time; (d) significant decrease in stress at the end of the annealing process about 5 minutes after starting, displaying a brightness level comparable with the image presented in (a); and (e) thermal history of the free stream thermocouple [116].



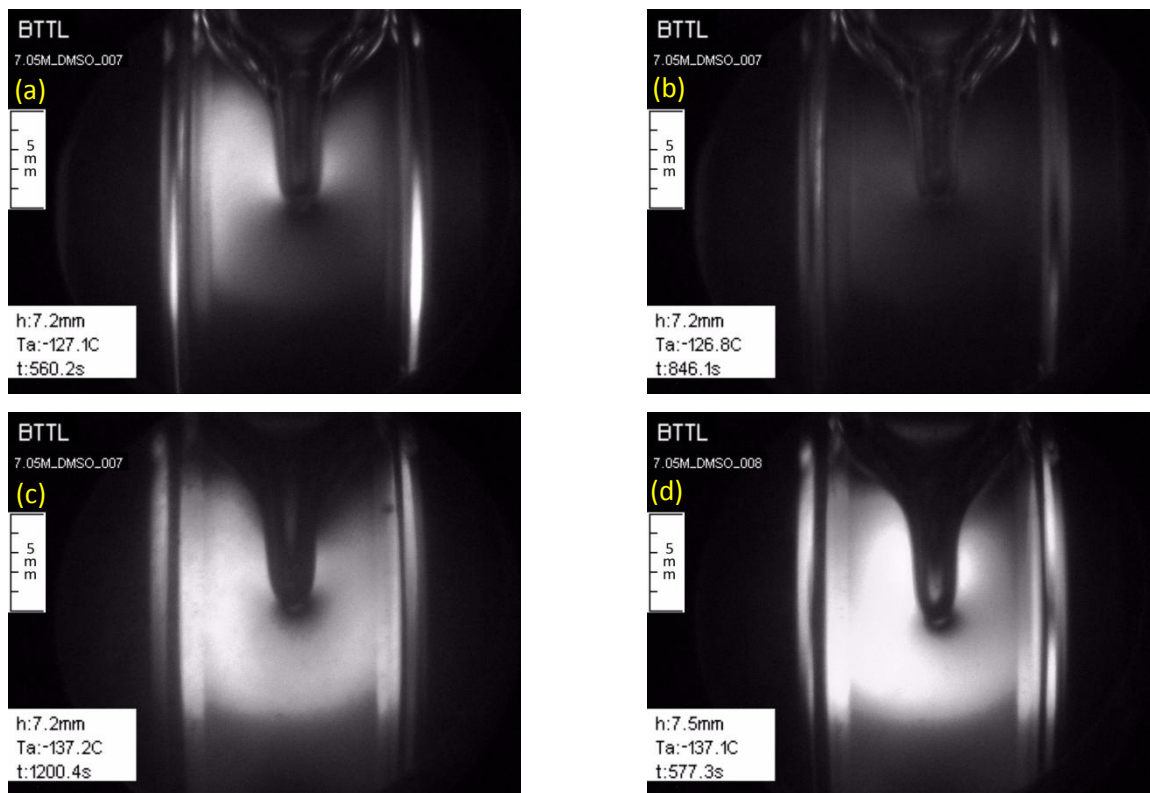


Figure 6.5: Scanning cryomicroscope images of photoelasticity effects in the study of annealing on 7.05M DMSO: (a) experiment #7 showing the beginning of annealing at -125°C with a polarized-light source power of 100 W; (b) stress-relaxed sample at the end of the temperature-hold stage in experiment #7; (c) the stress field in experiment #7 at 7°C below the glass transition temperature as measured by the free stream thermocouple, using a polarized-light source power of 45 W; (e) the stress field in experiment #8 at 7°C below the glass transition temperature as measured by the free stream thermocouple, using the same cooling protocol and illumination settings as in experiment #7 but in the absence of an annealing stage [117].

Figure 6.5(a) presents the onset of annealing where stress initially increases as the thermal gradient flattens as previously. Due to the viscoelastic nature of the CPA at this temperature, stress will relax away over time as indicated by an absence of localized bright regions in the image and as represented in Fig. 6.5(b). After annealing, any stress in the CPA at storage will then mostly be due to thermal strain mismatch between the CPA and cuvette instead of residual stress from thermal gradients. Figures 6.5(a) and 6.5(b) were captured when the polarized-light source was set to a power of 100 W to enable detection of stresses early in the viscoelastic regime.

Figures 6.5(c) and 6.5(d) display the stress in the vitrified material at 7°C below the glass transition temperature (as measured by the free stream thermocouple) for thermal protocols with

and without annealing respectively. These images are captured at a polarized light power setting of 45 W to avoid the potential for any saturation of the CCD sensors, and to promote the ability to detect any discrepancies in brightness between the two experiments (annealed vs. non-annealed). From visual inspection, the stress in the annealed CPA appears to be lower (based on image brightness) than in the non-annealed CPA, despite the fact that the temperature fields are essentially equivalent for the two protocols, as shown in Figs. 6.6(c) and 6.6(d) respectively. This implies that any excessive stress is not due to differences in thermal expansion mismatch between the two experiments. The thermal histories of the two cryoprotocols shown in Figs. 6.5(c) and 6.5(d) as recorded by free stream thermocouples are presented in Figs. 6.6(a) and 6.6(b) respectively.

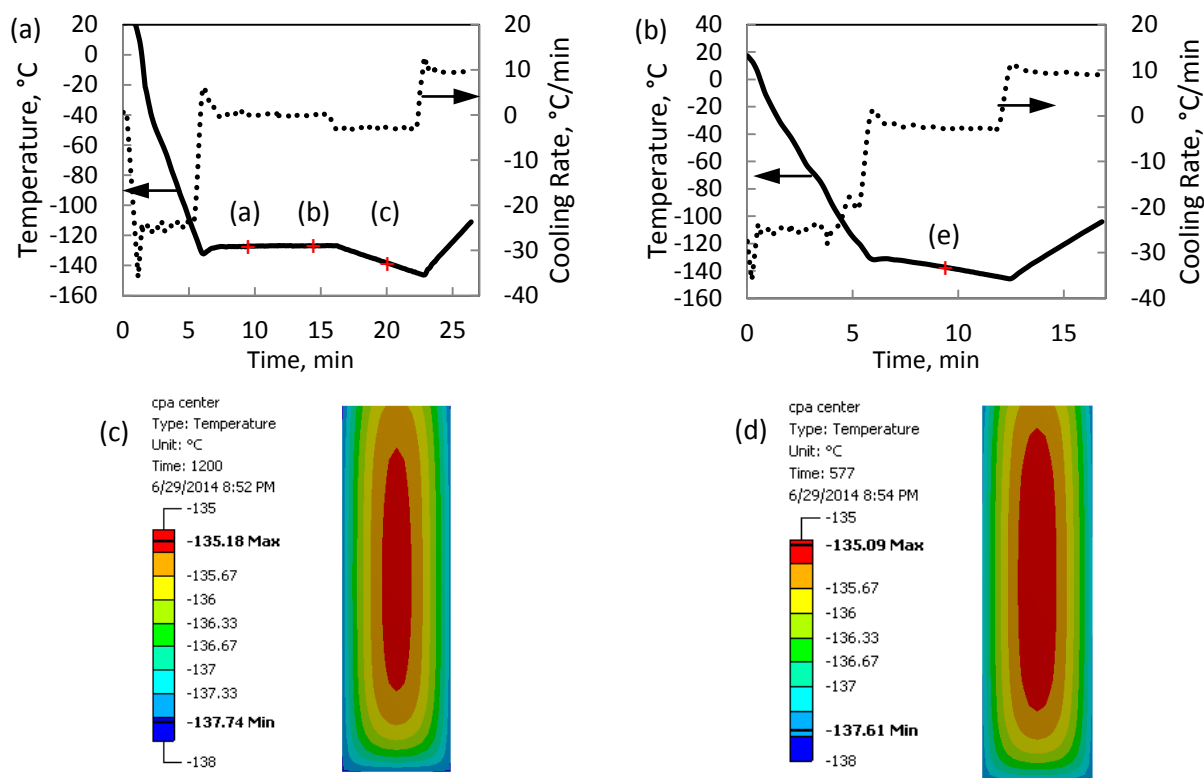


Figure 6.6: Thermal history of the experiments displayed in Fig. 8: (a) free stream thermocouple data from experiment #7 (with annealing at -125°C); (b) free stream thermocouple data from experiment #8 (no annealing); (c) ANSYS simulation results showing the temperature field at the center of the CPA from experiment #7 when the outer surface of the specimen reaches a temperature of 7°C below the glass transition temperature at 1200 seconds (corresponding to Fig. 8(c)); (d) ANSYS simulation results showing the temperature field at the center of the CPA from experiment #8 when the outer surface of the specimen reaches a temperature of 7°C below the glass transition temperature at 577 seconds (corresponding to Fig. 8(d)) [117].

The authors analyzed thermal stress in a vitrifying CPA within a rigid container via FEA [7]. While annealing could not reduce stress due to material property mismatch, it could reduce the residual stress due to thermal gradients. The experimental photoelastic results displayed in this section agrees with the analysis performed in [7], and indicates that proper annealing can be an effective strategy for minimizing residual stress during cryopreservation. To the best of our knowledge, this is the first time that structural annealing has been visualized in the context of cryopreservation by vitrification.

6.6 Summary of Photoelastic experiments

Polarized light was incorporated into the cryomicroscope device. It was used for (a) aiding in detection of crystallization, (b) identifying contaminants and (c) visualizing the stress field via photoelasticity, but in this chapter, the focus is on the analysis of photoelasticity. This allowed the authors to visualize the stress field in real time of an ongoing cryopreservation protocol. Using this method, the authors were able to identify a previously unseen phenomenon in the context of cryobiology involving increased stress during rewarming as the CPA traverses the glass transition temperature range. It is hypothesized in the current study that mechanical stress is dominated by fictive temperature gradients. Finally, photoelasticity, coupled with thermal FEA and image processing software was used to analyze annealing in-situ, and compare its effectiveness with a non-annealing protocol. These results qualitatively confirm the effects of annealing from the coupled thermal-structural FEA results presented in chapter 5.

Chapter 7: Volumetric Rewarming in Cryopreservation

This chapter expands upon a recently published paper [7] to include ferromagnetic nanoparticles heating in an oscillating magnetic field [118]. This work has been performed in collaboration with Dr. John Bischof and his research team at the Bioheat and Mass Transfer Laboratory at the University of Minnesota.

7.1 Volumetric warming techniques—background

In effort to implement a successful cryopreservation via vitrification protocol, designing the rewarming phase represents key challenges [13]. Firstly, the critical warming rate (i.e. the rate necessary to suppress crystallization) is about an order of magnitude faster than the critical cooling rate [87]. For example, the critical cooling and warming rates for VS55 are 2.5 and 50 °C/min respectively [70]. This means that without extremely rapid warming throughout the domain, the risk for rewarming phase crystallization is significant [88]. Since conventional rewarming techniques are applied at the outer surface of the specimen, and thermal conductivity of CPAs tend to be low (thermal conductivity of 7.05M DMSO is approximately 0.25 W/m-K [114]) the achievable rewarming rate at the center of the domain decreases as the size of the domain increases. Furthermore, under common rewarming protocols, there is additional rewarming stress that builds on top of the residual stress [7,51] which makes fractures most likely to occur during rewarming [31,32]. The need for high warming rates in order to suppress rewarming phase crystallization leads to higher thermal gradients, and thus, higher mechanical stress.

For the above reasons, a growing interest in rewarming means which can uniformly heat the entire volume of a vitrified sample has developed. This can potentially enable rapid heating, even at the center of a bulky specimen, to avoid rewarming phase crystallization without large thermal gradients and the mechanical stress that they cause. Most of these attempts have centered on using electromagnetic waves in the microwave frequency range (100's of MHz to GHz) [48,89–93]. However, the absorption properties of CPAs and tissues are frequency and temperature dependent subject to a non-linear relationship which may lead to problems for practical applications associated with field attenuation resulting in a skin depth for absorption, and spatial variation of the dielectric properties [94–96]. When these difficulties are coupled with

the positive feedback of temperature dependent absorptivity, hot spots may develop, which may lead to thermal runaway (i.e. some areas are far too hot while others are still too cold) [94,96,97].

Etheridge et al. [88] at the University of Minnesota have recently advanced an alternative rewarming modality. First, the tissue is perfused with magnetic nanoparticles in a CPA solution (5-10 mg Fe/ml of Fe_3O_4 particles with a diameter of $10 \pm 2.5\text{nm}$). Then electromagnetic waves in the radio frequency range (100's of KHz) are used. Radiofrequency electromagnetic waves can pass through tissues without any attenuation and with extremely high uniformity. Additionally, the absorptivity has very little temperature dependence, so there is little concern for thermal runaway, which is the aspect major challenge in microwave rewarming [88]. Ideally, uniform nanoparticle distribution and perfect insulation on the surfaces would lead to uniform heating which could prevent stress from continuing to develop during rewarming, although residual stress developed during cooling is not affected by the proposed rewarming technique. Unfortunately, reducing this concept to practice comes with great challenges. Based on the viscoelastic model developed in Chapter 5, if there has to be non-uniform heating, it would be better (from a mechanical stress standpoint) to engineer the thermal gradients so that the inside is hotter than the outside, as opposed vice versa, which is generally the case for boundary heating.

At high temperatures, the CPA behaves as a low viscous fluid, while the tissue behaves hyper-elastically; at low temperatures, both CPA and tissue can be approximated as having linear-elastic behavior [7,51,67]. It has been shown in those studies that when dealing with a standard cryopreservation protocol, which cools at the boundaries, and then rewarms at the boundaries, the stress induced during rewarming builds in addition to the residual stress formed at storage (see Section 5.3.1 for an in depth explanation). This explains why cryopreservation protocols often employ two stage cooling followed by two stage warming, a protocol which has been found experimentally. The slow cooling down to storage is designed to minimize residual stress, while the slow warming out of storage is designed to minimize the additional rewarming stress. Annealing can also be used to minimize residual stress, in which case, slow cooling is unnecessary [7].

However, a simple change to the thermal protocol can radically alter this picture. If after boundary cooling, the rewarming is done from the inside out, then the rewarming stress will act in the opposite direction of the residual stress. Instead of trying to minimize both the residual stress and the rewarming stress, the two effects can be balanced so that only the total maximum

stress needs to be minimized. That is, excessive rewarming stress can be mitigated by using higher residual stress induced by a higher cooling rate. By designing the nanoparticle rewarming protocol so that the temperatures are highest at the center and coolest at the surface, it will be possible to take advantage of this competition between rewarming stress and residual stress instead of having to fight against the cooperation between rewarming stress and residual stress.

7.2 Mathematical Model

The FEA model used to analyze the effects of nanoparticle warming is similar to that from Chapter 5 (plus the inclusion of volumetric warming) with dimensions similar to those used in [88]. It consists of a 1ml, axisymmetric cylinder with a radius of 5mm (thus a height of approximately 12.7mm). During cooling and storage, temperature boundary conditions are imposed on its surface. During rewarming, the domain has both convection at its surface (uniform on all surfaces), and uniform heat generation throughout the volume. Displacement boundary conditions are imposed radially and axially at the bottom corner on the axis of symmetry and axially at the bottom corner on the outer surface in order to preclude rigid body motions.

First the thermal analysis is performed, then the temperature history is used as input for a displacement analysis. Thus, coupling between the thermal problem and the solid mechanics problem is unidirectional, where the thermal results affect the displacement, but the displacement has no effect on the thermal analysis. The equation governing the thermal analysis is:

$$\rho C_p \dot{T} = \nabla \cdot (k \nabla T) + q''' \quad (7.1)$$

$$T(R) = T_R \quad (7.2)$$

$$q(R) = h(T_R - T_\infty) \quad (7.3)$$

Equation 7.1 is the same as Eq. 5.1, except for the inclusion of q''' , which is the volumetric heat generation term (only nonzero during warming). The boundary conditions are realized in Eqns 7.2 and 7.3 which are the temperature boundary condition during cooling, and the convection boundary condition during warming respectively. The convection coefficient, h , is set to 150 W/m²K, which is typical of forced convection. Equations 5.2-5.4 are used for the displacement analysis.

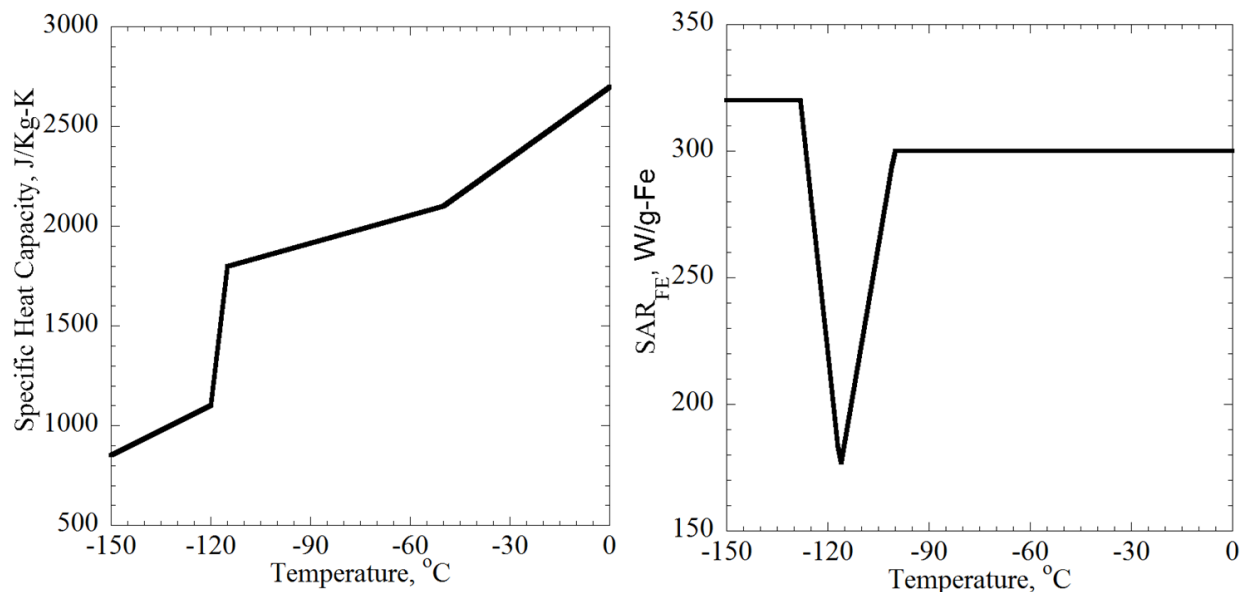


Figure 7.1: Specific heat capacity (left) and specific absorption rate (right) of VS55 combined with 10 mg/ml of Fe_3O_4 Nanoparticles

The specific absorption rate (SAR) and specific heat capacity of the CPA cocktail, VS55, were measured in [88]. These are shown in Fig. 7.1. The specific heat capacity ranges from approximately 850-2700 J/Kg-K and the SAR is about 300 W/g-Fe. The other material properties are the same as were tabulated for the simulations performed in chapter 5. One thousand elements were used for both analyses, using the same elements as was done for the simulations in chapter 5. Figure 7.2 displays the ambient temperature history of the domain.

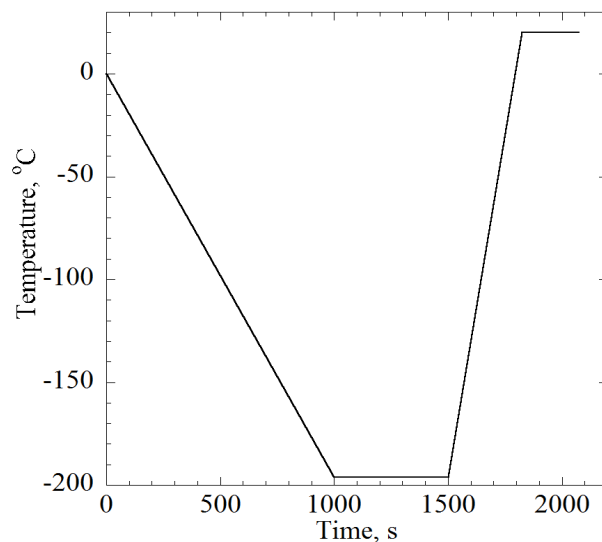


Figure 7.2: Ambient temperature history consists of one stage cooling (-11.76 C/min), 500s hold at storage, one stage warming (39.88C/min), and 250 s hold at room temperature

7.3 Results and Discussion

Figure 7.3 displays a typical axial stress history at the center of the domain for two cases: (i) boundary heating and (ii) volumetric heating at a rate of 3MW/m^3 (conversion from SAR shown in Fig. 7.1 to volumetric heat generation is done through dimensional analysis) so that the resultant temperature distribution is hottest at the center and coolest at the boundaries. It can be seen from Fig. 7.3 that the boundary rewarming causes a thermal gradient that induces tensile stress which builds on top of the residual stress at storage. On the other hand, the volumetric warming generates a thermal gradient which induces compressive stress, working against the residual stress at storage temperature.

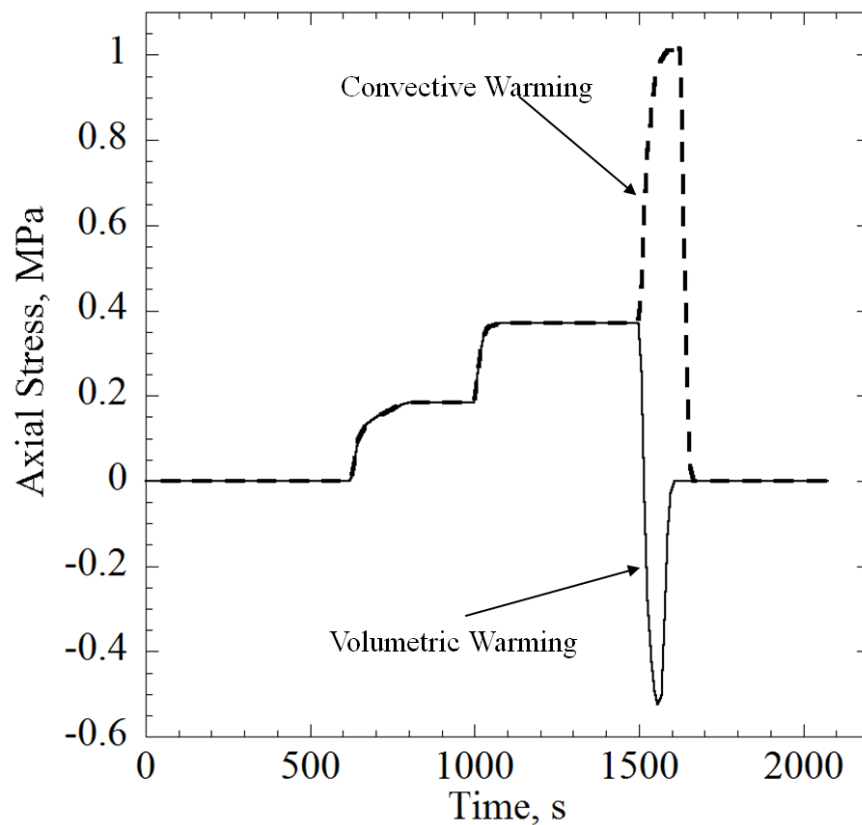


Figure 7.3: Axial stress at center of domain. Both protocols consist of identical cooling profiles and ambient rewarming temperatures. The volumetric rewarming case also includes uniform heat generation due to nano-particle RF warming

Figure 7.4 displays the stress history for volumetric warming at both the center and the wall. There are three distinct stress mechanisms. The first occurs around glass transition and is due to the change in specific heat capacity associated with structural relaxation issues (see section 6.4 or [104] for an explanation.) Note that the specific heat capacity was assumed

constant in the analysis performed in chapter 5, while the specific heat value is temperature dependent (as shown in Fig 7.1) in this analysis and so this stress mode is not seen in those simulations. The second stress mode is due to the equilibration of the thermal gradient at storage and the last one is due to the thermal gradient that forms at the onset of rewarming. The stresses at the center and the wall act in opposite directions to create force equilibrium in this static system. Since brittle materials such as vitrified tissue are most likely to fail due to excessive tensile stress, the stress at the wall is the area of greatest concern (as opposed to boundary warming where the stress at the center is of greatest concern).

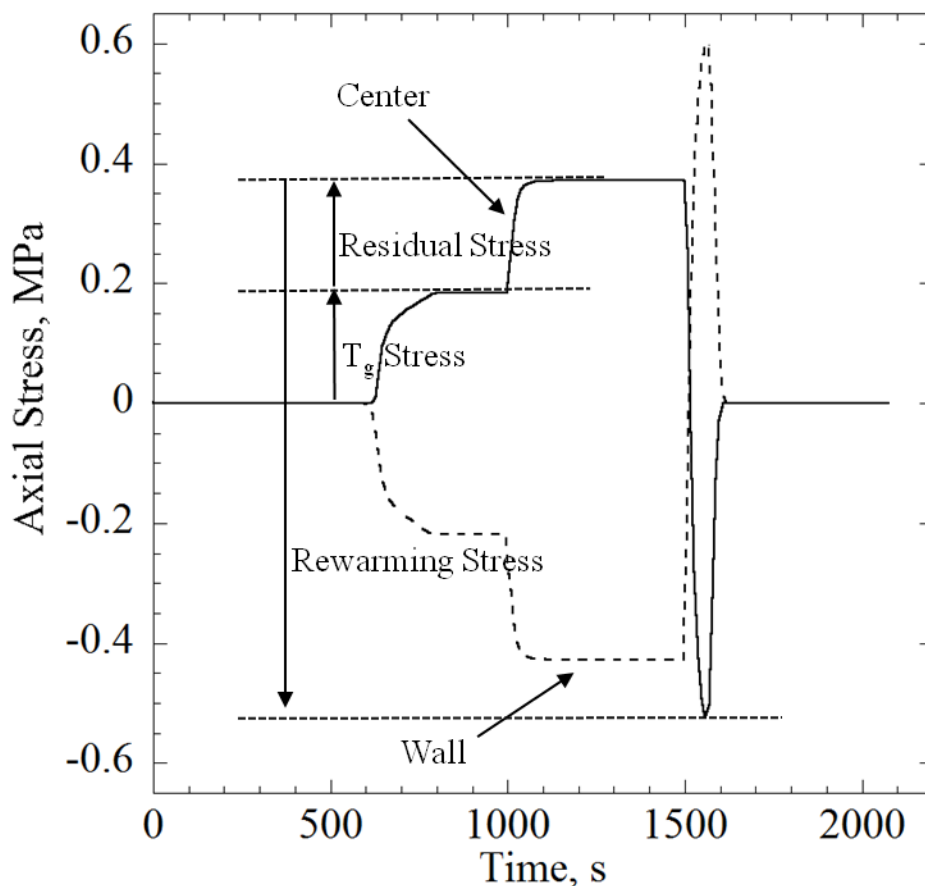


Figure 7.4: Stress history due to ambient temperature history shown in Fig. 7.2.

Since residual stress and rewarming stress work against each other in the volumetric warming scenario, excessive rewarming stress can be mitigated through higher residual stress. This effect is displayed in Fig. 7.5. The cooling rate can be increased in order to raise the residual stress, and thus decrease the maximum tensile stress. This indicates a paradigm shift in terms of designing cryopreservation protocols. The current art required extremely slow cooling

rates, followed by extremely slow rewarming rates in order to minimize both residual stress and rewarming stress. Unfortunately, these extremely slow rates ($0.1^{\circ}\text{C}/\text{min}$ and $1^{\circ}\text{C}/\text{min}$ cooling and warming rate respectively for the M22 CPA cocktail) require extremely high CPA concentration (M22 is 9.3M) in order to prevent crystallization. This high CPA concentration causes problems with both toxicity, and mass transfer due to the higher viscosity. By using inside out warming instead of boundary warming, excessive rewarming stress can be mitigated through higher residual stress. This allows for high warming rates and high cooling rates without exceeding the maximum tensile stress threshold. Higher cooling and warming rates offer the possibility of using lower CPA concentrations while still suppressing crystallization, thus alleviating problems associated with CPA toxicity and mass transfer.

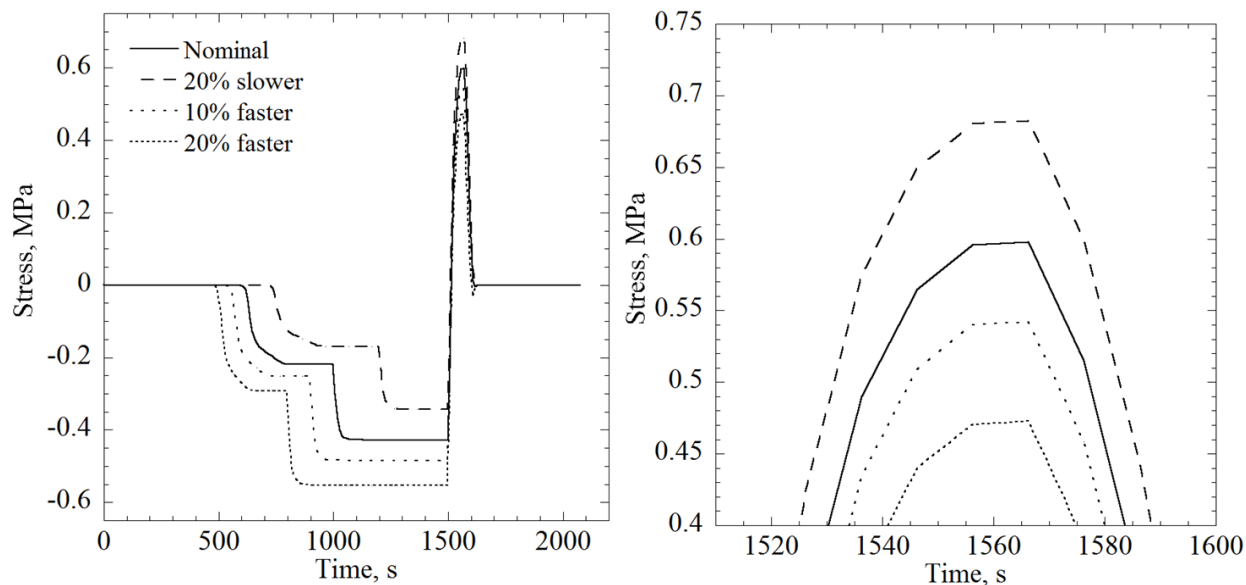


Figure 7.5: (left) stress history for four different cooling rates, (right) zoomed in maximum rewarming stress for those same cooling rates

7.4 Summary

Radiofrequency heating using magnetic nanoparticles could radically improve the rewarming rate at the center of bulky specimens, thus minimizing problems associated with rewarming phase crystallization without the same threat of thermal runaway as microwave heating suffers. One of the potential drawbacks to this technology is the possibility of non uniform temperature field due to either non uniform particle distribution or thermal interactions with the surroundings. This study demonstrates—for the first time—that if there must be non uniform heating in the domain, inside out heating offers significant advantages in terms of stress

compared to outside in heating. By using inside out heating, we can engineer stresses to remain within tolerable limits, even with extremely rapid cooling and warming rates.

Chapter 8: Future Work

The overarching goal of this work is to develop tools for analyzing coupled phenomena of heat transfer and mechanical stress in order to evaluate current cryopreservation protocols and to aid in the design of new ones in terms of minimizing structural damage due to excessive mechanical stress. This chapter begins with a brief summary of the work that has been accomplished toward this goal, and continues with suggested areas for further research.

8.1 Synopsis of Research Projects

This thesis is a part of an ongoing research activity at the Biothermal Technology Laboratory, with the unique contribution specified in Section 1.3, above. In the course of the work described above, a class of CPA additives known as synthetic ice modulators (SIM) was introduced. These SIMs were added to the CPA cocktail, DP6, in order to increase its effectiveness. The material properties of these DP6-SIM cocktails were then investigated experimentally in order to characterize their material properties. In particular, the thermal expansion of DP6+SIM cocktails in the upper part of the cryogenic temperature range, where the materials are still fluid (down to approximately -80°C) was measured. We also measured the thermal expansion of tissues permeated with the DP6+SIM cocktails throughout the entire cryogenic temperature range. Finally, we measured the stress strain properties such as Young's modulus, and fracture stress of vitrified tissues permeated with DP6+SIM cocktails.

A common cryopreservation thermal protocol (two stage cooling followed by two stage warming) as well as a modified version that included a temperature hold between the two cooling stages was modeled using finite elements. Using this work, we reproduced the empirical results which showed that the initial cooling rate and final warming rate have little effect on mechanical stress while the initial warming rate has a huge effect on mechanical stress. We also showed—for the first time—that a low temperature thermal hold can drastically reduce the amount of residual stress at storage, and renders the final cooling rate unimportant in terms of mechanical stress. We also investigated the effect of the container properties on mechanical stress. It was found that raising the storage temperature could reduce the mechanical stress due to thermal strain mismatch between the container and the CPA. Additionally, based on viscoelastic analysis of sandwich seals, we showed that rigid containers slow down the stress relaxation rate

during annealing, and that—counter intuitively—this effect is exacerbated by less stiff containers.

Furthermore, in collaboration with Dr. Justin Feig, we analyzed photoelastic images of vitrifying specimens using the cryomicroscope. We verified the ability to reduce mechanical stress via annealing. We also identified the novel phenomena of an increase in mechanical stress as the material rewarms through glass transition and provided a plausible hypothesis to explain it based on stresses due to fictive temperature gradients as discussed in [104].

Finally, we used finite element analysis to investigate the effects of volumetric rewarming on mechanical stress. We showed that using volumetric warming not only reduces mechanical stress due to reduced thermal gradient, but that by heating from the inside out, we can have the rewarming stress work against the residual stress, instead of in concert as is usually the case. This allows for a new paradigm with regard to stress minimization. Instead of trying to minimize mechanical stress by minimizing the residual stress and minimizing the rewarming stress, by heating from the inside out, the maximum stress can be reduced by increasing the residual stress and using it to work against the rewarming stress.

8.2 Future Experimental Work

The experiments described in this thesis as well as others performed in the BTTL have only measured a limited number of thermal and mechanical properties of a small number of CPAs, CPA cocktails, and tissues permeated with those CPAs. In order to create a truly comprehensive database to facilitate truly quantitative models, these efforts will need to be expanded greatly. Some of this work is relatively straightforward, such as using the systems already built to run similar experiments as before, but on a wider variety of materials. Obviously, the same experiments described previously could be applied to additional CPAs or CPA cocktails or tissues permeated with them.

We still have not measured the thermal expansion vitrified CPAs. Additionally, we need to measure Poisson's ratio and the extent of anisotropy of vitrified tissue. We will also need to experimentally investigate the mechanical response of tissues embedded within a glassy matrix. So far, there has been no effort to measure the structural relaxation properties (as described in section 6.4) of vitrifying tissues and CPAs. Both of these issues could become important for scale up of cryopreservation via vitrification.

8.3 Future Theoretical Work

The models presented throughout this thesis were more qualitative than quantitative. They could provide insight into the general nature of mechanical stress during cryopreservation via vitrification protocols, but couldn't accurately predict the actual level of stress for a given scenario. Firstly, some material properties were unknown, such as Poisson's ratio, and others were simplified for ease of analysis, such as coefficient of thermal expansion in the study presented in Chapter 5. Additionally, the viscoelastic model employed in these finite element analyses appears to have been sufficient to capture salient features such as residual stress at storage and stress relaxation, but is definitely not comprehensive. It is likely that there is actually a spectrum of stress relaxation times, which would need to be measured experimentally and could be modeled via a Prony series. In addition to stress being time dependent, the CPA is a glassy material, and some of the material properties should also be time dependent as described in section 6.4 (or in [104] in more detail). If these material properties are measured, then an even more accurate, Narayanaswamy type material model could be incorporated into the finite elements model in a manner similar to [98].

As discussed above, the tissue properties will need to be modeled in more detail in order to generate truly quantitative models. The material properties of tissues permeated with CPAs will need to be studied in more detail, particularly in terms of the interactions between the tissue and the CPA and any possible anisotropy. Finally, the geometries investigated in the previous finite element studies were unrealistically simple (axisymmetric cylinders). In an actual cryopreservation via vitrification protocol, tissues with complex shapes may be vitrified in pliable containers. Clearly, future modeling efforts will need to take these geometric issues into account. After all relevant material properties of CPAs and tissues permeated with CPAs are incorporated and complex Narayanaswamy finite element models are developed, we can realize the goal of truly quantitative models for cryopreservation via vitrification.

REFERENCES

- [1] Y. Rabin, J. Plitz, Thermal expansion of blood vessels and muscle specimens permeated with DMSO, DP6, and VS55 at cryogenic temperatures., *Ann. Biomed. Eng.* 33 (2005) 1213–28. doi:10.1007/s10439-005-5364-0.
- [2] D.P. Eisenberg, M.J. Taylor, Y. Rabin, Thermal expansion of the cryoprotectant cocktail DP6 combined with synthetic ice modulators in presence and absence of biological tissues, *Cryobiology*. 65 (2012) 117–125. doi:10.1016/j.cryobiol.2012.04.011.
- [3] J.L. Jimenez Rios, Y. Rabin, Thermal expansion of blood vessels in low cryogenic temperatures Part I: A new experimental device., *Cryobiology*. 52 (2006) 269–83. doi:10.1016/j.cryobiol.2005.12.005.
- [4] D.P. Eisenberg, M.J. Taylor, J.L. Jimenez-Rios, Y. Rabin, Thermal expansion of vitrified blood vessels permeated with DP6 and synthetic ice modulators, *Cryobiology*. 68 (2014) 318–326. doi:10.1016/j.cryobiol.2014.04.010.
- [5] D.P. Eisenberg, Y. Rabin, Stress-Strain Measurements in Vitrified Arteries Permeated With Synthetic Ice Modulators, *J. Biomech. Eng.* (2015). doi:10.1115/1.4030294.
- [6] J.S.G. Feig, Y. Rabin, The scanning cryomicroscope – A device prototype for the study of cryopreservation, *Cryogenics* (2014) 118–128. doi:10.1016/j.cryogenics.2014.04.017.
- [7] D.P. Eisenberg, P.S. Steif, Y. Rabin, On the effects of thermal history on the development and relaxation of thermo-mechanical stress in cryopreservation, *Cryogenics* (2014) 86–94. doi:10.1016/j.cryogenics.2014.09.005.
- [8] Y. Wang, D.J. Blasioli, H.-J. Kim, H.S. Kim, D.L. Kaplan, Cartilage tissue engineering with silk scaffolds and human articular chondrocytes., *Biomaterials*. 27 (2006) 4434–4442. doi:10.1016/j.biomaterials.2006.03.050.
- [9] L.E. Freed, F. Guilak, X.E. Guo, M.L. Gray, R. Tranquillo, J.W. Holmes, et al., Advanced tools for tissue engineering: scaffolds, bioreactors, and signaling., *Tissue Eng.* 12 (2006) 3285–3305. doi:10.1089/ten.2006.12.3285.
- [10] A.R. Costa-Pinto, R.L. Reis, N.M. Neves, Scaffolds Based Bone Tissue Engineering: The Role of Chitosan, *Tissue Eng. Part B Rev.* 17 (2011) 331–347. doi:10.1089/ten.teb.2010.0704.
- [11] A. Hadjizadeh, C.J. Doillon, Directional migration of endothelial cells towards angiogenesis using polymer fibres in a 3D co-culture system., *J. Tissue Eng. Regen. Med.* 4 (2010) 524–531. doi:10.1002/term.

- [12] P. Mazur, S.P. Leibo, E.H.Y. Chu, A two-factor hypothesis of freezing injury, *Exp. Cell Res.* 71 (1972) 345–355. doi:10.1016/0014-4827(72)90303-5.
- [13] S. Seki, P. Mazur, The Dominance of Warming Rate Over Cooling Rate in the Survival of Mouse Oocytes Subjected to a Vitrification Procedure, *Cryobiology*. 59 (2009) 75–82. doi:10.1016/j.cryobiol.2009.04.012.
- [14] D.E. Pegg, Principles of cryopreservation., *Methods Mol. Biol.* 368 (2007) 39–57. doi:10.1007/978-1-59745-362-2_3.
- [15] R. Spindler, B. Rosenhahn, N. Hofmann, B. Glasmacher, Video analysis of osmotic cell response during cryopreservation, *Cryobiology*. 64 (2012) 250–260. doi:10.1016/j.cryobiol.2012.02.008.
- [16] M.J. Taylor, L.H. Campbell, R.N. Rutledge, K.G. Brockbank, Comparison of Unisol with Euro-Collins solution as a vehicle solution for cryoprotectants., *Transplant. Proc.* 33 (2001) 677–9. <http://www.ncbi.nlm.nih.gov/pubmed/11267013>.
- [17] D.E. Pegg, I. a Jacobsen, W.J. Armitage, M.J. Taylor, Mechanism of Cryoinjury In Organs, in: D.E. Pegg, I.A. Jacobson (Eds.), *Organ Preserv. II*, Churchill Livingstone, Edinburgh, United Kingdom, 1979: pp. 132–146.
- [18] G.H. Almassi, B. Farahbakhsh, T. Wooldridge, N.J. Rusch, G.N. Olinger, Endothelium and vascular smooth muscle function in internal mammary artery after cryopreservation., *J. Surg. Res.* 60 (1996) 355–360. doi:10.1006/jsre.1996.0057.
- [19] B. Lehalle, C. Geschier, G. Fiévé, J.F. Stoltz, Early rupture and degeneration of cryopreserved arterial allografts., *J. Vasc. Surg. Off. Publ. Soc. Vasc. Surg. [and] Int. Soc. Cardiovasc. Surgery, North Am. Chapter.* 25 (1997) 751–752.
- [20] M. Taylor, Y. Song, K. Brockbank, 22 Vitrification in Tissue Preservation: New Developments, in: B.J. Fuller, N. Lane, E.E. Benson (Eds.), *Life Frozen State*, CRC Press, 2004: pp. 604–641. http://www.researchgate.net/publication/52002273_Vitrification_in_Tissue_Preservation_New_Developments/file/79e41511282cb4a314.pdf (accessed August 8, 2014).
- [21] Y.C. Song, B.S. Khirabadi, F. Lightfoot, K.G. Brockbank, M.J. Taylor, Vitreous cryopreservation maintains the function of vascular grafts., *Nat. Biotechnol.* 18 (2000) 296–9. doi:10.1038/73737.
- [22] P.J. Schmidt, Basile J. Luyet and the Beginnings of Transfusion Cryobiology, *Transfus. Med. Rev.* 20 (2006) 242–246. doi:10.1016/j.tmr.2006.03.004.
- [23] B. Luyet, The vitrification of organic colloids and of protoplasm, *Biodynamica*. 1 (1937) 1–14. doi:10.1016/S0011-2240(66)80032-9.

- [24] G.M. Fahy, B. Wowk, J. Wu, S. Paynter, Improved vitrification solutions based on the predictability of vitrification solution toxicity., *Cryobiology*. 48 (2004) 22–35. doi:10.1016/j.cryobiol.2003.11.004.
- [25] H. Meryman, Cryoprotective agents, *Cryobiology*. 8 (1971) 173–183. <http://onlinelibrary.wiley.com/doi/10.1002/cbdv.200490137/abstract> (accessed August 8, 2014).
- [26] B. Wowk, E. Leidl, C.M. Rasch, N. Mesbah-Karimi, S.B. Harris, G.M. Fahy, Vitrification enhancement by synthetic ice blocking agents., *Cryobiology*. 40 (2000) 228–36. doi:10.1006/cryo.2000.2243.
- [27] B. Wowk, G.M. Fahy, Inhibition of bacterial ice nucleation by polyglycerol polymers., *Cryobiology*. 44 (2002) 14–23. doi:10.1016/S0011-2240(02)00008-1.
- [28] C. Budke, T. Koop, Ice recrystallization inhibition and molecular recognition of ice faces by poly(vinyl alcohol)., *Chemphyschem*. 7 (2006) 2601–6. doi:10.1002/cphc.200600533.
- [29] D. Kami, J. Kasuga, K. Arakawa, S. Fujikawa, Improved cryopreservation by diluted vitrification solution with supercooling-facilitating flavonol glycoside., *Cryobiology*. 57 (2008) 242–5. doi:10.1016/j.cryobiol.2008.09.003.
- [30] M. Kasai, S.E. Zhu, P.B. Pedro, K. Nakamura, T. Sakurai, K. Edashige, Fracture damage of embryos and its prevention during vitrification and warming., *Cryobiology*. 33 (1996) 459–64. doi:10.1006/cryo.1996.0046.
- [31] D.E. Pegg, M.C. Wusteman, S. Boylan, Fractures in cryopreserved elastic arteries., *Cryobiology*. 34 (1997) 183–92. doi:10.1006/cryo.1996.1997.
- [32] C.J. Hunt, Y.C. Song, E. a Bateson, D.E. Pegg, Fractures in cryopreserved arteries., *Cryobiology*. 31 (1994) 506–15. doi:10.1006/cryo.1994.1061.
- [33] A. Rajamohan, R.A. Leopold, Cryopreservation of Mexican fruit flies by vitrification: stage selection and avoidance of thermal stress., *Cryobiology*. 54 (2007) 44–54. doi:10.1016/j.cryobiol.2006.10.192.
- [34] P.S. Steif, M. Palastro, C.-R. Wan, S. Baicu, M.J. Taylor, Y. Rabin, Cryomacroscopy of vitrification, Part II: Experimental observations and analysis of fracture formation in vitrified VS55 and DP6., *Cell Preserv. Technol*. 3 (2005) 184–200. <http://www.pubmedcentral.nih.gov/articlerender.fcgi?artid=1533993&tool=pmcentrez&rendertype=abstract>.
- [35] P.S. Steif, M.C. Palastro, Y. Rabin, Continuum Mechanics analysis of fracture progression in the vitrified cryoprotective agent DP6, *J*. 130 (2008) 997–1003. doi:10.1115/1.2898716.

- [36] G.M. Fahy, B. Wowk, R. Pagotan, A. Chang, J. Phan, B. Thomson, et al., Physical and biological aspects of renal vitrification., *Organogenesis*. 5 (2009) 167–75.
<http://www.pubmedcentral.nih.gov/articlerender.fcgi?artid=2781097&tool=pmcentrez&rendertype=abstract>.
- [37] J. Plitz, Y. Rabin, J. Walsh, The effect of thermal expansion of ingredients on the cocktails VS55 and DP6, *Cell Preserv. Technol.* (2004).
<http://online.liebertpub.com/doi/abs/10.1089/cpt.2004.2.215> (accessed August 8, 2014).
- [38] J.L. Jimenez Rios, Y. Rabin, A New Device for Mechanical Testing of Blood Vessels at Cryogenic Temperatures., *Exp. Mech.* 47 (2007) 1741–2765. doi:10.1007/s11340-007-9038-8.
- [39] J.L. Jimenez Rios, P.S. Steif, Y. Rabin, Stress-strain measurements and viscoelastic response of blood vessels cryopreserved by vitrification., *Ann. Biomed. Eng.* 35 (2007) 2077–86. doi:10.1007/s10439-007-9372-0.
- [40] Y. Rabin, E. Bell, Thermal expansion measurements of cryoprotective agents. Part I: A new experimental apparatus, *Cryobiology*. 46 (2003) 254–263. doi:10.1016/S0011-2240(03)00042-7.
- [41] Y. Rabin, E. Bell, Thermal expansion measurements of cryoprotective agents. Part II: Measurements of DP6 and VS55, and comparison with DMSO, *Cryobiology*. 46 (2003) 264–270. doi:10.1016/S0011-2240(03)00041-5.
- [42] J.L. Jimenez Rios, Y. Rabin, Thermal expansion of blood vessels in low cryogenic temperatures, Part II: Vitrification with VS55, DP6, and 7.05 M DMSO., *Cryobiology*. 52 (2006) 284–94. doi:10.1016/j.cryobiol.2005.12.006.
- [43] D.A. Noday, P.S. Steif, Y. Rabin, Viscosity of cryoprotective agents near glass transition: a new device, technique, and data on DMSO, DP6, and VS55., *Exp. Mech.* 49 (2009) 663–672. doi:10.1007/s11340-008-9191-8.
- [44] G.M. Fahy, methods of using ice-controlling molecules, 6773877, 2004.
- [45] T. Inada, P.R. Modak, Growth control of ice crystals by poly(vinyl alcohol) and antifreeze protein in ice slurries, *Chem. Eng. Sci.* 61 (2006) 3149–3158.
doi:10.1016/j.ces.2005.12.005.
- [46] T. Inada, S.-S. Lu, Thermal hysteresis caused by non-equilibrium antifreeze activity of poly(vinyl alcohol), *Chem. Phys. Lett.* 394 (2004) 361–365.
doi:10.1016/j.cplett.2004.07.021.
- [47] M.J. Taylor, S. Baicu, Review of vitreous islet cryopreservation: Some practical issues and their resolution., *Organogenesis*. 5 (2009) 155–66.

<http://www.pubmedcentral.nih.gov/articlerender.fcgi?artid=2781096&tool=pmcentrez&rendertype=abstract>.

- [48] E. Burdette, S. Wiggins, R. Brown, A.K. Jr, Microwave thawing of frozen kidneys: a theoretically based experimentally-effective design, *Cryobiology*. 402 (1980) 393–402. <http://www.sciencedirect.com/science/article/pii/0011224080900462> (accessed August 8, 2014).
- [49] Y. Rabin, M.J. Taylor, J.R. Walsh, S. Baicu, P.S. Steif, Cryomacroscopy of Vitrification I: A Prototype and Experimental Observations on the Cocktails VS55 and DP6, *Cell Preserv. Technol.* 3 (2005) 169–183. doi:10.1089/cpt.2005.3.169.
- [50] P.S. Steif, M.C. Palastro, Y. Rabin, Analysis of the effect of partial vitrification on stress development in cryopreserved blood vessels., *Med. Eng. Phys.* 29 (2007) 661–70. doi:10.1016/j.medengphy.2006.07.010.
- [51] P. Steif, M. Palastro, Y. Rabin, The effect of temperature gradients on stress development during cryopreservation via vitrification, *Cell Preserv. Technol.* 5 (2007) 104–115. <http://online.liebertpub.com/doi/abs/10.1089/cpt.2007.9994> (accessed August 8, 2014).
- [52] P.S. Steif, D.A. Noday, Y. Rabin, Can thermal expansion differences between cryopreserved tissue and cryoprotective agents alone cause cracking?, *Cryo-Letters*. 30 (2009) 414–421.
- [53] L.H. Campbell, R.N. Rutledge, M.J. Taylor, K.G.M. Brockbank, Abstracts of Papers Presented at the Thirty-Sixth Annual Meeting of the Society for Cryobiology, Jointly with France Cryo and the Society for Low Temperature Biology, in: *Cryobiology*, 1999: p. 362. doi:10.1016/S0011-2240(99)92210-1.
- [54] R.L. Sutton, Critical cooling rates for aqueous cryoprotectants in the presence of sugars and polysaccharides, *Cryobiology*. 29 (1992) 585–598. doi:10.1016/0011-2240(92)90063-8.
- [55] P. Boutron, Erratum: levo- and dextro-2,3-Butanediol and their racemic mixture: Very efficient solutes for vitrification (Volume 27, Number 1 pp. 55-69 (1990)), *Cryobiology*. 27 (1990) 343. doi:10.1016/0011-2240(90)90034-2.
- [56] M.J. Taylor, J. Foreman, Abstracts of papers presented at the 16th annual meeting of the Society for Cryobiology., in: *Cryobiology*, 1991: pp. 566–567.
- [57] P. Boutron, J.F. Peyridieu, Reduction in toxicity for red blood cells in buffered solutions containing high concentrations of 2,3-butanediol by trehalose, sucrose, sorbitol, or mannitol., *Cryobiology*. 31 (1994) 367–373. doi:10.1006/cryo.1994.1044.
- [58] S. Baicu, M.J. Taylor, Z. Chen, Y. Rabin, Cryopreservation of carotid artery segments via vitrification subject to marginal thermal conditions: Correlation of freezing visualization

- with functional recovery, *Cryobiology*. 57 (2008) 1–8.
doi:10.1016/j.cryobiol.2008.03.002.
- [59] J.P. Holman, *Experimental methods for engineers*, in: *Exp. Methods Eng.*, 7th ed., McGraw-Hill, 2000.
 - [60] A.M. D'Alessandro, J.H. Southard, R.B. Love, F.O. Belzer, *Organ preservation.*, *Surg. Clin. North Am.* 74 (1994) 1083–1095.
 - [61] Y. Rabin, P. Olson, M.J. Taylor, P.S. Steif, T.B. Julian, N. Wolmark, *Gross damage accumulation on frozen rabbit liver due to mechanical stress at cryogenic temperatures.*, *Cryobiology*. 34 (1997) 394–405.
 - [62] Y. Rabin, P.S. Steif, M.J. Taylor, T.B. Julian, N. Wolmark, *An experimental study of the mechanical response of frozen biological tissues at cryogenic temperatures.*, *Cryobiology*. 33 (1996) 472–482. doi:10.1006/cryo.1996.0048.
 - [63] G. Gamble, J. Zorn, G. Sanders, S. MacMahon, N. Sharpe, *Estimation of arterial stiffness, compliance, and distensibility from M-mode ultrasound measurements of the common carotid artery.*, *Stroke*. 25 (1994) 11–16. doi:10.1161/01.STR.25.1.11.
 - [64] J. Zhou, Y.C. Fung, *The degree of nonlinearity and anisotropy of blood vessel elasticity.*, *Proc. Natl. Acad. Sci. U. S. A.* 94 (1997) 14255–14260. doi:10.1073/pnas.94.26.14255.
 - [65] Y. Rabin, P.S. Steif, K.C. Hess, J.L. Jimenez-Rios, M.C. Palastro, *Fracture formation in vitrified thin films of cryoprotectants*, *Cryobiology*. 53 (2006) 75–95.
doi:10.1016/j.cryobiol.2006.03.013.
 - [66] P.S. Steif, M.C. Palastro, Y. Rabin, *Continuum mechanics analysis of fracture progression in the vitrified cryoprotective agent DP6.*, *J. Biomech. Eng.* 130 (2008) 021006.
doi:10.1115/1.2898716.
 - [67] Y. Rabin, P.S. Steif, *Letter to the editor: Analysis of thermo-mechanical stress in cryopreservation [1]*, *Cryo-Letters*. 26 (2005) 409–411.
 - [68] Y. Rabin, P.S. Steif, *Thermal Stresses in a Freezing Sphere and its Application to Cryobiology*, *J. Appl. Mech.* 65 (1998) 328. doi:10.1115/1.2789058.
 - [69] Y. Rabin, J.S.G. Feig, A.C. Williams, C.C. Lin, C. Thaokar, *Cryomacroscopy in 3D: A device prototype for the study of cryopreservation*, in: *Proc. ASME 2012 Summer Bioeng. Conf.*, Fajardo, Puerto Rico, 2012: pp. 1–2.
 - [70] P.M. Mehl, *Nucleation and Crystal Growth in a Vitrification Solution Tested for Organ Cryopreservation by Vitrification.*, *Cryobiology*. 30 (1993) 509–518.
doi:10.1006/cryo.1993.1051.

- [71] T.M. Aminabhavi, B.Gopalakrishna, Density, Viscosity, Refractive-Index, and Speed of Sound In Aqueous Mixtures of N,N, Dimethylacetamide, Acetonitrile, Ethylene-Glycol, Diethylene Glycol, 1,4-Dioxane, Tetrahydrofuran, 2-Methoxyethanol, and 2-Ethox, J. Chem. Eng. Data. 40 (1995) 856–861. doi:10.1021/je00020a026.
- [72] U. Gaur, B. Wunderlich, Heat capacity and other thermodynamic properties of linear macromolecules. V. polystyrene, J. Phys. Chem. Ref. Data. 11 (1982). <http://scitation.aip.org/content/aip/journal/jpcrd/11/2/10.1063/1.555663> (accessed August 8, 2014).
- [73] X. Zhang, W. Hendro, M. Fujii, Measurements of the thermal conductivity and thermal diffusivity of polymer melts with the short-hot-wire method, Int. J. Thermophys. 23 (2002) 1077–1090. <http://link.springer.com/article/10.1023/A:1016394104244> (accessed August 8, 2014).
- [74] P. Westht, Thermal Expansivity, Molar Volume, and Heat Capacity of Liquid Dimethyl Sulfoxide-Water Mixtures at Subzero Temperatures, J. Phys. Chem. 98 (1994) 3222–3225. doi:10.1021/j100063a028.
- [75] D.S. Hughes, E.B. Blankenship, R.L. Mims, Variation of Elastic Moduli and Wave Velocity with Pressure and Temperature in Plastics, J. Appl. Phys. 21 (1950) 294. doi:10.1063/1.1699656.
- [76] J.S.G. Feig, Y. Rabin, 005 Integration of polarized light into scanning cryomacroscopy, in: CRYO2013, Elsevier Inc., N. Bethesda, 2013: pp. 399–400. doi:10.1016/j.cryobiol.2013.09.011.
- [77] Y. Rabin, M.J. Taylor, J.S.G. Feig, S. Baicu, Z. Chen, A new cryomicroscope device (Type III) for visualization of physical events in cryopreservation with applications to vitrification and synthetic ice modulators, Cryobiology. 67 (2013) 264–273. doi:10.1016/j.cryobiol.2013.08.005.
- [78] K.R. Diller, E.G. Cravalho, A cryomicroscope for the study of freezing and thawing processes in biological cells., Cryobiology. 7 (1971) 191–199. doi:10.1016/0011-2240(70)90021-0.
- [79] S.L. Stott, J.O.M. Karlsson, Visualization of intracellular ice formation using high-speed video cryomicroscopy, Cryobiology. 58 (2009) 84–95. doi:10.1016/j.cryobiol.2008.11.003.
- [80] M. Toner, E.G. Cravalho, M. Karel, D.R. Armant, Cryomicroscopic analysis of intracellular ice formation during freezing of mouse oocytes without cryoadditives., Cryobiology. 28 (1991) 55–71. doi:10.1016/0011-2240(91)90008-C.
- [81] S. Baicu, M.J. Taylor, Z. Chen, Y. Rabin, Vitrification of Carotid Artery Segments: An Integrated Study of Thermophysical Events And Functional Recovery Toward Scale-Up

- for Clinical Applications, *Cell Preserv. Technol.* 4 (2006) 236–244.
doi:10.1089/cpt.2006.9994.
- [82] B. Luyet, An attempt at a systematic analysis of the notion of freezing rates and at an evaluation of the main contributory factors, *Cryobiology*. 19 (1966).
<http://www.sciencedirect.com/science/article/pii/S0011224066801670> (accessed August 8, 2014).
- [83] A.Q. Tool, Relation Between Inelastic Deformability and Thermal Expansion of Glass in Its Annealing Range, *J. Am. Ceram. Soc.* 29 (1946) 240–253. doi:10.1111/j.1151-2916.1946.tb11592.x.
- [84] O.S. Narayanaswamy, A Model of Structural Relaxation in Glass, *J. Am. Ceram. Soc.* 54 (1971) 491–498. doi:10.1111/j.1151-2916.1971.tb12186.x.
- [85] D.H. Rasmussen, A.P. MacKenzie, Phase diagram for the system water-dimethylsulphoxide, *Nature*. 220 (1968) 1315–1317.
- [86] A. Baudot, L. Alger, P. Boutron, Glass-forming tendency in the system water-dimethyl sulfoxide., *Cryobiology*. 40 (2000) 151–158. doi:10.1006/cryo.2000.2234.
- [87] J.B. Hopkins, R. Badeau, M. Warkentin, R.E. Thorne, Effect of common cryoprotectants on critical warming rates and ice formation in aqueous solutions., *Cryobiology*. 65 (2012) 169–78. doi:10.1016/j.cryobiol.2012.05.010.
- [88] M.L. Etheridge, Y. Xu, L. Rott, J. Choi, B. Glasmacher, J. Bischof, RF heating of magnetic nanoparticles improves the thawing of cryopreserved biomaterials, *Technology*. 2 (2014). doi:10.1142/S2339547814500204.
- [89] C. Gordon, Rewarming mice from hypothermia by exposure to 2450-MHz microwave radiation, *Cryobiology*. 434 (1982) 428–434.
<http://www.sciencedirect.com/science/article/pii/0011224082901717> (accessed August 8, 2014).
- [90] D. Cooper, F. Ketterer, H. Holst, Organ temperature measurement in a microwave oven by resonance frequency shift., *Cryobiology*. 18 (1981) 378–85.
<http://www.ncbi.nlm.nih.gov/pubmed/7307528>.
- [91] T. Wang, G. Zhao, X.M. Liang, Y. Xu, Y. Li, H. Tang, et al., Numerical simulation of the effect of superparamagnetic nanoparticles on microwave rewarming of cryopreserved tissues, *Cryobiology*. 68 (2014) 234–243. doi:10.1016/j.cryobiol.2014.02.002.
- [92] M. Schmehl, E. Graham, S. Kilkowski, Thermographic studies of phantom and canine kidneys thawed by microwave radiation, *Cryobiology*. 318 (1989) 311–318.
<http://scholar.google.com/scholar?hl=en&btnG=Search&q=intitle:Thermographic+Studies>

- +of+Phantom+and+Canine+kidneys+Thawed+by+microwave+radiation#0 (accessed August 8, 2014).
- [93] M. Phelan, F. Douglas, Controlled-Rate Liquid N₂-Microwave biological freeze-thaw device, 391 (1982) 372–391.
 - [94] M.P. Robinson, M.C. Wusteman, L. Wang, D.E. Pegg, Electromagnetic re-warming of cryopreserved tissues: effect of choice of cryoprotectant and sample shape on uniformity of heating., *Phys. Med. Biol.* 47 (2002) 2311–2325. doi:10.1088/0031-9155/47/13/309.
 - [95] M. Wusteman, M. Robinson, D. Pegg, Vitrification of large tissues with dielectric warming: Biological problems and some approaches to their solution, *Cryobiology*. 48 (2004) 179–189. doi:10.1016/j.cryobiol.2004.01.002.
 - [96] S. Evans, Electromagnetic rewarming: the effect of CPA concentration and radio source frequency on uniformity and efficiency of heating., *Cryobiology*. 40 (2000) 126–138. doi:10.1006/cryo.2000.2232.
 - [97] K.G.M. Brockbank, M.J. Taylor, tissue preservation, in: J.G. Baust, J.M. Baust (Eds.), *Adv. Biopreservation*, CRC Press, 2006: pp. 157–196.
 - [98] J. Nielsen, H. Stang, J. Olesen, P. Poulsen, *Tempered Glass: bolted connections and related problems*, 2009.
<http://scholar.google.com/scholar?hl=en&btnG=Search&q=intitle:Tempered+Glass+-+bolted+connections+and+related+problems#0> (accessed August 8, 2014).
 - [99] D.E. Pegg, I.A. Jacobson, W.J. Armitage and M.J. Taylor, Mechanism of Cryoinjury In Organs. in: D.E. Pegg, I.A. Jacobson (Eds.), *Organ Preservation II*, Churchill-Livingston, London, 1979, pp. 132–146.
 - [100] D.E. Pegg, Principles of tissue preservation. In: Morris PJ, Tilney NL, eds. *Progress in Transplantation*. Edinburgh, United Kingdom: Churchill Livingstone; 1985:69-105
 - [101] Pegg DE. Ice crystals in tissue and organs. In: Pegg DE, Karow AM, Jr., eds. *The Biophysics of Organ Preservation*. New York: Plenum Publishing Corp.; 1987:117-140
 - [102] K.G.M. Brockbank, J.R. Walsh, Y.C. Song, M.J. Taylor, Vitrification. *Encyclopedia of Biomaterials and Biomedical Engineering*. Informa Healthcare, Chap. 292 (2008) 3046-3057; <http://informahealthcare.com/doi/abs/10.3109/9781420078039.292>
 - [103] C.J. Hunt, M.J. Taylor, D.E. Pegg, Freeze substitution and isothermal freeze fixation studies to elucidate the pattern of ice formation on smooth muscle at 252K (-21°C), *J. Microsc.* 125 (1982) pp. 177-186

- [104] Scherer, G. W. (1986): *Relaxation in Glass and Composites*, New York, NY, John Wiley & Sons, Inc.
- [105] B. Luyet, G. Rapatz, An automatic regulated refrigeration system for small laboratory equipment and a microscope cooling stage. *Biodynamica* 7 (1957) pp. 337-345
- [106] J.J. Menz, B.J. Luyet, A study of the lines of fracture observed in freeze-drying of aqueous solutions crystallized into spherulites. *Biodynamica* 9 (1965) pp.265-275
- [107] C. Kroener, B.J. Luyet, Formation of cracks during the vitrification of glycerol solutions and disappearance of the cracks during rewarming. *Biodynamicca* 10 (1966) pp. 47-52
- [108] <http://www.andrew.cmu.edu/user/yr25/CryomacroscopyImages01.htm>
- [109] <http://www.andrew.cmu.edu/user/yr25/CryomacroscopyImages02/index.htm>
- [110] Bartholin, E. (1669) *Experimenta crystalli islandici disdiaclastici quibus mira & insolita refractio detegitur* (Copenhagen ("Hafniæ"), Denmark: Daniel Paulli). English translation: *Experiments with the double refracting Iceland crystal which led to the discovery of a marvelous and strange refraction*, tr. by Werner Brandt. Westtown, Pa., 1959
- [111] Brewster, D. (1815) *Experiments on the depolarization of light as exhibited by various mineral, animal and vegetable bodies with a reference of the phenomena to the general principle of polarization*. *Phil. Tras.*, 29-53
- [112] Brewster, D. (1816) *On the communication of the structure of doubly-refracting crystals to glass, murite of soda, flour spar, and other substances by mechanical compression and dilation*. *Phil. Tras.*, 156-178
- [113] Jessop, H.T., Harris, F.C. (1949) *Photoelasticity: Principles and Methods*, Dover Publications, New York
- [114] Ehrlich, L.E., Feig, J.S.G., Schiffres, S.N., Malen, S.N., Rabin, Y., 2013, "Integration of transient hot-wire method into scanning cryomacroscopy in the study of thermal conductivity of dimethyl sulfoxide," 50th meeting of the society of cryobiology, Bethesda, Md, July 28-31 2013
- [115] *Thermal Analysis and Properties of Polymers*, Engineered Materials Handbook Desk

Edition, ASM International, 1995, p. 367–392

- [116] J.S.G. Feig, D.P. Eisenberg, Y. Rabin, Polarized Light Scanning Cryomacroscopy, Part I: Experimental Apparatus and Observations of Vitrification, Crystallization, and Photoelasticity Effects, *in preparation*
- [117] J.S.G. Feig, D.P. Eisenberg, and Y. Rabin, Polarized Light Scanning Cryomacroscopy, Part II: Thermal Analysis, *in preparation*
- [118] D.P. Eisenberg, M. Etheridge, J. Bischoff, Y. Rabin, Inside-out warming radically reduces mechanical stress in cryopreservation via vitrification, *in preparation*

APPENDIX: Material Property Summary

Medium	Property	Tissue	Temperature Range	Value	Source
7.05M DMSO	Fracture Stress	Goat Arteries	-138.5 to -142.2	13.93 ± 1.83	[38]
	Fracture Stress	Goat Arteries	-138.2 to -167.7	11.98 ± 3.36	[5]
	Strain to Fracture	Pure Solution	Below Tg	0.28% to 0.36%	[65]
	Thermal Conductivity	Pure Solution	25.5 to -180.0	$-2.95 \times 10^{-10}T^4 - 5.76 \times 10^{-8}T^3 - 2.31 \times 10^{-6}T^2 + 5.57 \times 10^{-4}T + 3.23 \times 10^{-1}$	[114]
	Thermal Expansion	Pure Solution	22.5 to -48	$5.574 \times 10^{-7}T^2 + 1.637 \times 10^{-4}T - 3.995 \times 10^{-3}$	[37]
	Thermal Expansion	Bovine Muscles	19.0 to -65.3	$1.033 \times 10^{-6}T^2 + 2.136 \times 10^{-4}T - 3.901 \times 10^{-3}$	[1]
	Thermal Expansion	Goat Arteries	18.8 to -93.1	$6.127 \times 10^{-7}T^2 + 1.995 \times 10^{-4}T - 4.895 \times 10^{-4}$	[1]
	Thermal Expansion	Goat Arteries	-93.1 to -167.7	$4.434 \times 10^{-7}T^2 + 1.849 \times 10^{-4}T$	[42]
	Thermal Expansion	Goat Arteries	18.8 to -167.7	$4.796 \times 10^{-7}T^2 + 1.890 \times 10^{-4}T - 4.939 \times 10^{-3}$	[42]
	Viscosity	Pure Solution	-123 to -134	$2.8190 \times 10^{-27}e^{(-0.6447T)}$	[43]
	Young's Modulus	Goat Arteries	-138.5 to -142.2	921 ± 93	[38]
	Young's Modulus	Goat Arteries	-138.2 to -167.7	2143 ± 754	[5]
VS55	Fracture Stress	Goat Arteries	-129.4 to 143.9	11.98 ± 1.94	[38]
	Specific Heat Capacity	Pure Solution	20 to -50	$11T + 2650$	[88]
	Specific Heat Capacity	Pure Solution	-50 to -120	$4.2857T + 2314.3$	[88]
	Specific Heat Capacity	Pure Solution	-120 to -150	$8.333T + 2100$	[88]
	Strain to Fracture	Pure Solution	Below Tg	0.23%	[65]
	Thermal Expansion	Pure Solution	17.5 to -77.1	$2.012 \times 10^{-7}T^2 + 1.841 \times 10^{-4}T - 3.839 \times 10^{-3}$	[37]
	Thermal Expansion	Bovine Muscles	19.3 to -47.8	$4.118 \times 10^{-7}T^2 + 1.852 \times 10^{-4}T - 2.655 \times 10^{-3}$	[1]
	Thermal Expansion	Goat Arteries	19.4 to -63.6	$9.425 \times 10^{-7}T^2 + 2.081 \times 10^{-4}T - 3.711 \times 10^{-3}$	[1]
	Thermal Expansion	Goat Arteries	-82.5 to -165.3	$4.781 \times 10^{-7}T^2 + 1.785 \times 10^{-4}T$	[42]
	Thermal Expansion	Goat Arteries	19.4 to -165.3	$5.312 \times 10^{-7}T^2 + 1.911 \times 10^{-4}T - 3.652 \times 10^{-3}$	[42]
	Viscosity	Pure Solution	-117 to -124	$4.2783 \times 10^{-23}e^{(-0.60917T)}$	[43]
	Young's Modulus	Goat Arteries	-129.4 to 143.9	973 ± 157	[38]

DP6	Strain to Fracture	Pure Solution	Below Tg	0.18%	[65]
	Thermal Expansion	Pure Solution	18.6 to -67.9	$3.899 \times 10^{-7}T^2 + 1.935 \times 10^{-4}T - 4.130 \times 10^{-3}$	[2]
	Thermal Expansion	Bovine Muscles	19.4 to -35.5	$1.017 \times 10^{-6}T^2 + 1.512 \times 10^{-4}T - 4.286 \times 10^{-3}$	[37]
	Thermal Expansion	Goat Arteries	19.2 to -40.5	$1.041 \times 10^{-6}T^2 + 1.653 \times 10^{-4}T - 4.447 \times 10^{-3}$	[37]
	Thermal Expansion	Goat Arteries	-85.1 to -167.2	$5.114 \times 10^{-7}T^2 + 1.893 \times 10^{-4}T$	[42]
	Thermal Expansion	Goat Arteries	19.2 to -167.2	$3.825 \times 10^{-7}T^2 + 1.564 \times 10^{-4}T - 4.321 \times 10^{-3}$	[42]
	Viscosity	Pure Solution	-114 to -121	$5.6503 \times 10^{-23} e^{(-0.6207T)}$	[43]
DP6 + 12% PEG400	Fracture Stress	Goat Arteries	-139.8 to -149.3	10.58 ± 3.01	[5]
	Thermal Expansion	Pure Solution	0 to -95	$-0.2188 \times 10^{-7}T^2 + 2.313 \times 10^{-4}T - 4.959 \times 10^{-4}$	[2]
	Thermal Expansion	Bovine Muscles	0 to -85	$1.697 \times 10^{-7}T^2 + 2.118 \times 10^{-4}T + 9.822 \times 10^{-4}$	[2]
	Thermal Expansion	Goat Arteries	0 to -80	$1.777 \times 10^{-7}T^2 + 2.392 \times 10^{-4}T - 4.866 \times 10^{-4}$	[2]
	Thermal Expansion	Goat Arteries	-80 to -160	$1.065 \times 10^{-10}T^4 + 0.624 \times 10^{-7}T^3 + 1.364 \times 10^{-5}T^2 + 1.358 \times 10^{-3}T + 4.911 \times 10^{-2}$	[4]
	Thermal Expansion	Goat Arteries	0 to -160	$-0.8668 \times 10^{-10}T^4 - 0.2995 \times 10^{-7}T^3 - 0.2358 \times 10^{-5}T^2 - 0.1757 \times 10^{-3}T - 0.0275 \times 10^{-2}$	[4]
	Young's Modulus	Goat Arteries	-139.8 to -149.3	2248 ± 224	[5]
DP6 + 6% 1,3- CHD	Fracture Stress	Goat Arteries	-142.8 to -151.0	12.04 ± 4.72	[5]
	Thermal Expansion	Pure Solution	0 to -80	$-0.6272 \times 10^{-7}T^2 + 1.957 \times 10^{-4}T + 0.2699 \times 10^{-4}$	[2]
	Thermal Expansion	Bovine Muscles	0 to -80	$4.411E \times 10^{-7}T^2 + 2.175 \times 10^{-4}T - 13.66 \times 10^{-4}$	[2]
	Thermal Expansion	Goat Arteries	0 to -80	$1.054 \times 10^{-7}T^2 + 2.232 \times 10^{-4}T - 5.477 \times 10^{-4}$	[2]
	Thermal Expansion	Goat Arteries	-80 to -160	$1.155 \times 10^{-10}T^4 + 0.639 \times 10^{-7}T^3 + 1.330 \times 10^{-5}T^2 + 1.283 \times 10^{-3}T + 4.550 \times 10^{-2}$	[4]
	Thermal Expansion	Goat Arteries	0 to -160	$-0.7969 \times 10^{-10}T^4 - 0.2771 \times 10^{-7}T^3 - 0.2210 \times 10^{-5}T^2 + 0.1666 \times 10^{-3}T - 0.0236 \times 10^{-2}$	[4]
	Young's Modulus	Goat Arteries	-142.8 to -151.0	2019 ± 394	[5]
DP6 + 6% 2,3- BD	Fracture Stress	Goat Arteries	-141.0 to -153.0	15.50 ± 3.39	[5]
	Thermal Expansion	Pure Solution	0 to -90	$0.6309 \times 10^{-7}T^2 + 2.080 \times 10^{-4}T + 4.518 \times 10^{-4}$	[2]
	Thermal Expansion	Bovine Muscles	0 to -85	$1.431 \times 10^{-7}T^2 + 2.094 \times 10^{-4}T - 11.17 \times 10^{-4}$	[2]
	Thermal Expansion	Goat Arteries	0 to -90	$0.7383 \times 10^{-7}T^2 + 1.912 \times 10^{-4}T - 11.04 \times 10^{-4}$	[2]
	Thermal Expansion	Goat Arteries	-80 to -160	$2.672 \times 10^{-10}T^4 + 1.379 \times 10^{-7}T^3 + 2.668 \times 10^{-5}T^2 + 2.342 \times 10^{-3}T + 7.562 \times 10^{-2}$	[4]
	Thermal Expansion	Goat Arteries	0 to -160	$-0.5587 \times 10^{-10}T^4 - 0.2066 \times 10^{-7}T^3 - 0.1747 \times 10^{-5}T^2 + 0.1442 \times 10^{-3}T - 0.0209 \times 10^{-2}$	[4]
	Young's Modulus	Goat Arteries	-141.0 to -153.0	2419 ± 526	[5]